

DESIGN AND CONTROL OF POWERED TRANSTIBIAL PROSTHESES

by

HAO ZHENG

XIANGRONG SHEN, COMMITTEE CHAIR

KEITH A. WILLIAMS
NIMA MAHMOODI
BETH A. TODD
FEI HU

A DISSERTATION

Submitted in partial fulfillment of the requirements
for the degree of Doctor of Philosophy
in the Department of Mechanical Engineering
in the Graduate School of
The University of Alabama

TUSCALOOSA, ALABAMA

2017

Copyright Hao Zheng 2017
ALL RIGHTS RESERVED

ABSTRACT

The primary purpose of lower extremity prostheses is to restore the locomotive functions of amputees' lost sections and joints. The objective of this dissertation is to develop energetically active transtibial (TT, also known as below-knee) prostheses with powered ankle joints to generate sufficient power and torque with a compact form factor.

Firstly, pneumatic sleeve muscle actuators have been designed and tested to investigate the feasibility of application of such type of actuator in TT prosthesis. Experimental results obtained on the prototypes validated and proved that sleeve muscle is a good fit for robotic systems with asymmetric force/torque requirements.

Although the pneumatic sleeve muscle can provide sound force/torque capacities, it is challenging to build a transtibial prosthesis with this type of actuator that can match the size and weight of the human ankle. Hence, the subsequent efforts are directed towards utilizing a more compact actuation unit – pneumatic cylinder, which is well known for its capability in generating large force/power output with light weight and compact volumetric profile. Thus, a transtibial prosthesis has been designed using pneumatic cylinder. A finite-state impedance controller (FSIC) has been developed as a walking controller, and the parameters are tuned in walking experiments. The results from the experiments proved that the prosthesis is able to provide an improved gait compared with the traditional passive prosthesis.

Additionally, a model that characterizes the stiffness and equilibrium point as functions of the chamber air masses in the pneumatic cylinder has been developed and a predictive pressure control algorithm was used to improve pressure control performance while minimizing

valve actions. This enables the pneumatic actuator to be used as a variable series elastic actuator (VSEA). Experimental results showed that the proposed approach is able to provide the desired elastic characteristics of an artificial spring in stiffness control and demonstrated the advantages of this new approach for potential prosthetic applications.

Lastly, the dissertation presents VSEA-powered TT prosthesis with direct implementation of the finite-state impedance control (FSIC). The human subject walking experiments were also conducted, and the results demonstrated the effectiveness of the direct FSIC prosthesis control approach.

DEDICATION

This dissertation is dedicated to my family and friends who stood by me, helped me and guided me throughout the time taken to complete this masterpiece.

LIST OF ABBREVIATIONS AND SYMBOLS

TT	Transtibial
PAM	Pneumatic Artificial Muscle
SASM	Single-acting Sleeve Muscle
DASM	Double-acting Sleeve Muscle
ES	Early Stance
MS	Middle Stance
LS	Late Stance
SW	Swing
CP	Controlled Plantarflexion
CD	Controlled Dorsiflexion
PP	Powered Plantarflexion
SACH	Solid Ankle or Cushioned Heel
SPARKy	Spring Ankle with Regenerative Kinetics
VSEA	Variable Series Elastic Actuator
FSIC	Finite-state Impedance Controller

ACKNOWLEDGMENTS

First of all, I would like to express my sincerest and deepest gratitude and appreciation to my advisor, Dr. Xiangrong Shen, a great mentor, and scholar, for his continuous guidance and support throughout my entire Ph.D. journey. Without his guidance, support, and patience I would not have been able to reach this stage. I would also like to thank Dr. Keith Williams, Dr. Nima Mahmoodi, Dr. Beth Todd and Dr. Fei Hu for their valuable guidance and advice to complete my dissertation.

Next, I would like to thank all the fellows in Hub-robotics lab: Molei Wu, Tao Shen, Saroj Thapa, Rejwanul Haque, Rayhan Afsar, Cosmo Chou; and all the amputee subjects for their suggestions and coordination. They are always willing to help me and made a great contribution on every part of my research projects.

Lastly, I'd like to express my deepest gratitude to my family and friends who have always encouraged and supported me. In particular, I would like to thank my wonderful wife, Lina, for her never-ending support and encouragement.

CONTENTS

ABSTRACT	ii
DEDICATION	iv
LIST OF ABBREVIATIONS AND SYMBOLS	v
ACKNOWLEDGMENTS	vi
LIST OF TABLES.....	x
LIST OF FIGURES	xi
CHAPTER 1: INTRODUCTION	1
1.1 MOTIVATION	1
1.2 OBJECTIVES AND ORGANIZATION	2
CHAPTER 2: BACKGROUND AND LITERATURE REVIEW	3
2.1 NORMAL WALKING GAIT	3
2.2 STATE-OF-THE-ART TRANSTIBIAL PROSTHESES.....	6
REFERENCES.....	11
CHAPTER 3: CONCEPT, DESIGN AND APPLICATION OF SLEEVE MUSCLE ACTUATOR.....	13
3.1 INTRODUCTION.....	13
3.2 INSPIRATION OF THE SLEEVE MUSCLE CONCEPT	16
3.3 SINGLE-ACTING SLEEVE MUSCLE ACTUATOR	19
3.4 DOUBLE-ACTING SLEEVE MUSCLE ACTUATOR	22
3.5 APPLICATION OF DA SLEEVE MUSCLE IN BIO-ROBOTICS	30

3.6 CONCLUSIONS	32
REFERENCES	33
CHAPTER 4: DESIGN AND CONTROL OF PNEUMATICALLY ACTUATED TRANSTIBIAL PROSTHESIS	35
4.1 INTRODUCTION.....	35
4.2 PROSTHESIS DESIGN	37
4.2.1 DESIGN SPECIFICATIONS	37
4.2.2 MECHANICAL DESIGN	39
4.2.3 INSTRUMENTATION AND THE COMPLETE PROSTHESIS PACKAGE	43
4.3 PROSTHESIS CONTROL	45
4.3.1 ANKLE BIOMECHANICS IN WALKING	46
4.3.2 IMPEDANCE MODELING	48
4.3.3 CONTROLLER IMPLEMENTATION	50
4.4 PROSTHESIS TESTING.....	52
4.5 CONCLUSIONS	56
4.6 ACKNOWLEDGMENT	57
REFERENCES.....	58
CHAPTER 5: PNEUMATIC VARIABLE SERIES ELASTIC ACTUATOR	61
5.1 INTRODUCTION.....	62
5.2 PNEUMATIC ACTUATOR AS A VSEA	64
5.3 STIFFNESS CONTROL OF PNEUMATIC ACTUATOR.....	68
5.4 EXPERIMENTAL RESULTS	75
5.5 CONCLUSIONS	84
5.6 ACKNOWLEDGMENT	86

REFERENCES.....	87
CHAPTER 6: A PNEUMATIC VARIABLE SERIES ELASTIC ACTUATOR-POWERED TRANSTIBIAL PROSTHESIS	90
6.1 INTRODUCTION.....	90
6.2 PNEUMATIC VSEA-POWERED TRANSTIBIAL PROSTHESIS	93
6.2.1 PNEUMATIC VARIABLE SERIES ELASTIC ACTUATOR	93
6.2.2 PNEUMATIC VSEA-POWERED TRANSTIBIAL PROSTHESIS PROTOTYPE	97
6.3 DIRECTLY IMPLEMENTED FINITE-STATE IMPEDANCE CONTROLLER	100
6.3.1 IMPEDANCE CHARACTERIZATION OF THE ANKLE BEHAVIOR.....	101
6.3.2 DIRECT IMPLEMENTATION OF FSIC CONTROLLER WITH PNEUMATIC VSEA.....	104
6.4 EXPERIMENTAL TESTING RESULTS	107
6.5 CONCLUSIONS.....	111
REFERENCES.....	113
CHAPTER 7: CONCLUSION	115
REFERENCES.....	117
APPENDIX: IRB APPROVAL.....	118

LIST OF TABLES

Table 3-1: Comparison of block forces and free contractions.....	28
Table 4-1: The design parameters of the transtibial prosthesis prototype.....	41
Table 4-2: Parameters of the prosthesis controller.....	54
Table 5-1: Model and control parameters.....	77

LIST OF FIGURES

Figure 2-1: Human ankle biomechanics for level-ground walking from Au et al. (2009)	4
Figure 2-2: A typical ankle torque vs. angle behavior for a person walking at moderate speed (1.25 m/sec) from Au et al. (2009)	5
Figure 2-3: (a) SACH foot (Ohio Willow Wood); (b) Single-axis foot (Ohio Willow Wood); (c) Flex- Foot® Assure (Össur); (d) Össur Proprio Foot® (Össur).	7
Figure 2-4: BionX™ PowerFoot BiOM	9
Figure 2-5: Odyssey (SpringActive, Inc).....	10
Figure 2-6: Powered ankle prosthesis from Shultz et al. (2014).....	10
Figure 3-1: Structure (a) and actuation mechanism (b) of the pneumatic muscle.	14
Figure 3-2: Dividing the internal volume into two parts: V_1 and V_2	17
Figure 3-3: Contributions of V_1 and V_2 to the contraction force: F_1 is extension force due to the internal pressure, and F_2 is extension force by the membrane.	18
Figure 3-4: Schematic of the SA sleeve muscle actuator.	19
Figure 3-5: Comparison of force outputs under the same internal pressure.	20
Figure 3-6: The design of the SA sleeve muscle prototype. (a) The end connectors of the commercial pneumatic muscle are drilled through to accommodate the insert; (b) The insert features an internal air pathway to enable the access to the internal volume; (c) the assembled SA sleeve muscle actuator.	21
Figure 3-7: Measured and theoretically calculated force outputs of the SA sleeve muscle in comparison with the force output of the original unmodified pneumatic muscle under the gauge pressure of 414 kPa (60 psi).....	22
Figure 3-8: Concept of the DA sleeve muscle: (a) Separating V_1 and V_2 with a rigid shell; (b) The resulting DA sleeve muscle structure.	23
Figure 3-9: Force capacity of the DA sleeve muscle in comparison with that of the traditional pneumatic muscle.....	25

Figure 3-10: Prototype of the DA sleeve muscle: (a) Modified commercial pneumatic muscle; (b) Aluminum connector with stainless steel shell; (c) Solid aluminum insert mounted on the stationary end; (d) Assembled actuator prototype.....	26
Figure 3-11: Measured and theoretically calculated force outputs of the DA sleeve muscle in comparison with the force output of the original unmodified pneumatic muscle under the gauge pressure of 276 kPa (40 psi).....	27
Figure 3-12: Measured and theoretically calculated force outputs of the DA sleeve muscle in comparison with the force output of the original unmodified pneumatic muscle under the gauge pressure of 414 kPa (60 psi).....	28
Figure 3-13: Body weight-normalized torque trajectory of the ankle in fast walking.....	31
Figure 3-14: Conceptual design of a DA sleeve muscle-actuated robotic ankle.....	32
Figure 4-1: The torque trajectory of the ankle in slow walking (data from [2]).....	38
Figure 4-2: The actuation mechanism of the transtibial prosthesis.....	39
Figure 4-3: Comparison of the actuation torque capacity versus the ankle torque trajectory in walking.....	42
Figure 4-4: Photo of the prosthesis prototype when removed from the foot shell.....	44
Figure 4-5: Analysis of the ankle dynamic behavior in walking: (a) Segmentation of the original torque trajectory, (b) Simple impedance representation to understand the dynamic behavior within each phase.....	48
Figure 4-6: Finite-state machine for the implementation of the prosthesis controller.....	51
Figure 4-7: The test subject fitted with the transtibial prosthesis.....	52
Figure 4-8: Comparison of the trajectory of the prosthetic ankle joint versus the standard ankle trajectory of healthy subjects in level walking (data from [2]).....	55
Figure 4-9: Comparison of the torque trajectory of the prosthetic ankle joint versus the standard ankle torque trajectory of healthy subjects in level walking (data from [2]).....	55
Figure 4-10: Power output of the actuated ankle joint.....	56
Figure 5-1: Double-acting pneumatic cylinder with two independently controlled chambers....	65
Figure 5-2: Stiffness control of a pneumatic actuator: (a) Controller structure and (b) system diagram.....	70
Figure 5-3: The predictive pressure controller.....	71

Figure 5-4: Experimental setup.....	76
Figure 5-5: Piston position trajectory in the pneumatic VSEA experiment.	78
Figure 5-6: Desired versus measured actuator force in the pneumatic VSEA experiment.	79
Figure 5-7: Measured versus desired spring behavior in the pneumatic VSEA experiment.	79
Figure 5-8: Solenoid valve commands for chambers a and b in the pneumatic VSEA experiment.	80
Figure 5-9: Piston position trajectory in the experiment that involves the transition between two different sets of stiffness/equilibrium point.	81
Figure 5-10: Desired versus measured actuator force in the experiment that involves the transition between two different sets of stiffness/equilibrium point.....	81
Figure 5-11: Piston position trajectory in the closed-loop implemented stiffness control experiment.	83
Figure 5-12: Desired versus measured actuator force in the closed-loop implemented stiffness control experiment.	83
Figure 5-13: Measured versus desired spring behavior in the closed-loop implemented stiffness control experiment.	84
Figure 5-14: Proportional valve command (normalized to -1 to 1 range) in the closed-loop implemented stiffness control experiment.	84
Figure 6-1: Schematic of the pneumatic VSEA.....	94
Figure 6-2: Controller structure of the pneumatic VSEA	97
Figure 6-3: The pneumatic VSEA-powered transtibial prosthesis: (a) schematic of the actuation system; (b) a photo of the prototype.	98
Figure 6-4: Position trajectory (a) and torque trajectory (b) of the ankle in walking (plotted based on the data from [2]).	102
Figure 6-5: Position-torque curve generated by combining the position and torque trajectories in Fig. 6-4.....	102
Figure 6-6: Position-torque curve generated by the theoretical simulation of the directly implemented FSIC controller.....	106
Figure 6-7: Finite state machine of the directly implemented FSIC controller.	107
Figure 6-8: The test subject fitted with the pneumatic VSEA-actuated transtibial prosthesis. ..	108

Figure 6-9: Typical position and torque trajectories of the prosthetic ankle joint
in treadmill walking 109

Figure 6-10: The chamber pressure trajectories of the prosthetic ankle joint (above: Chamber A
pressure; below: Chamber B pressure). 110

Figure 6-11: The valve commands of the prosthetic ankle joint (-1 represents exhausting the
chamber, 0 represents closing the chamber, and 1 represents pressurizing the chamber)..... 111

CHAPTER 1: INTRODUCTION

1.1 MOTIVATION

From the research that has been done by Ziegler-Graham *et al.* [1], it showed that nearly 2 million persons are living with the loss of limbs in the United States and there are approximately 185,000 amputations occur in the United States each year. It is predicted that the number of people living with limb loss will be increased to 3.6 million by the year 2050 [2].

Currently, most amputees and orthopedically impaired people performed certain tasks using passive devices. Although currently available prosthetic devices have been well developed, the majority of those devices are passive which cannot provide positive net power at the joint and can only dissipate energy. For example, lower extremity amputees are suffering from an extraordinary loss in power and mobility after amputation due to the loss of significant amount of energy which is provided by knee and ankle joints during the stance period of walking [3]. According to the clinical studies in [4], in the absence of active power generated by knee and ankle, transfemoral amputees using passive prostheses expend up to 60% more metabolic energy compared to healthy subjects. Also, lower limb amputees exhibit an asymmetric gait pattern during stance of walking. For unilateral transtibial amputees, hip extension, knee flexion, and ankle dorsiflexion perform higher than normal on the unaffected side and perform lower than normal on the affected side, respectively [5, 6]. With those limitations of using passive devices,

powered prosthetics and orthotics seek to reduce or eliminate many of the problems amputees face after ambulation by providing positive power and normal gait.

1.2 OBJECTIVES AND ORGANIZATION

To eliminate limitations in passive prosthesis devices, this research is to develop a powered transtibial (TT) prosthesis which can provide positive energy for amputees during walking.

This dissertation consists of three major objectives. The first objective is to investigate the feasibility of pneumatic artificial muscle (PAM) modified to an advanced form of the actuator which is called sleeve muscle actuator in TT prosthesis applications. The second objective is to develop a pneumatically actuated TT prosthesis, which utilizes a pneumatic cylinder-type actuator to power the prosthetic ankle joint to support the user's locomotion. The third objective is to present a new approach by modeling pneumatic actuator as a variable series elastic actuator (VSEA) with controllable stiffness and equilibrium point which aims to improve the control performance and reduce the control action of the developed TT prosthesis.

This dissertation is organized into seven chapters. Chapter 1 presents the introduction and motivation of the work. Chapter 2 presents the background and literature review of state-of-the-art transtibial prosthetic devices. Chapter 3 presents the design and application of sleeve muscle actuator. Chapter 4 presents the design and control of a pneumatically actuated TT prosthesis. Chapter 5 presents the modeling and control of the novel VSEA; and finally, Chapter 6 presents the VSEA-powered TT prosthesis with direct implementation of the finite-state impedance control (FSIC).

CHAPTER 2:BACKGROUND AND LITERATURE REVIEW

Understanding normal walking biomechanics is very important in design and control of the below-knee prosthetic devices. In this chapter, gait cycle analysis of normal human ankle-foot is presented to understand features of normal walking biomechanics. Moreover, the background and literature review of the below-knee prostheses including current state-of-the-art prosthetic devices, as well as current research in the related area is presented.

2.1 NORMAL WALKING GAIT

Normal walking gait cycle and its biomechanical characteristics is the topic of this section, which includes basic concepts of human walking, as well as a detailed kinematic and kinetic analysis of human gait. A normal walking gait cycle is defined as a period of time from heel strike of one foot to next heel strike of the same foot [1]. Normally, there are two main subdivisions of a standard gait cycle, the stance phase (about 60% of a full gait cycle) and the swing phase (about 40% of a full gait cycle). The stance phase of gait can be divided by the point of initial contact of the foot onto the ground (heel strike), the point when the foot is flat on the ground (foot flat), the point when the maximum dorsiflexion occurs (max. dorsiflexion) and the point when the stance phase ends (toe off). The swing phase (SW) represents the portion of the gait cycle when the foot is off the ground during walking. Moreover, the stance phase can be divided into three sub-phases: controlled plantarflexion (CP) which starts at heel strike and ends

at foot flat; controlled dorsiflexion (CD) which starts at foot flat and continues until the ankle reaches maximum dorsiflexion; and powered plantarflexion (PP) which starts after CD and ends at the time of toe off [2]. These phases are presented in Fig. 2-1 and the corresponding ankle joint behaviors are also illustrated in the figure.

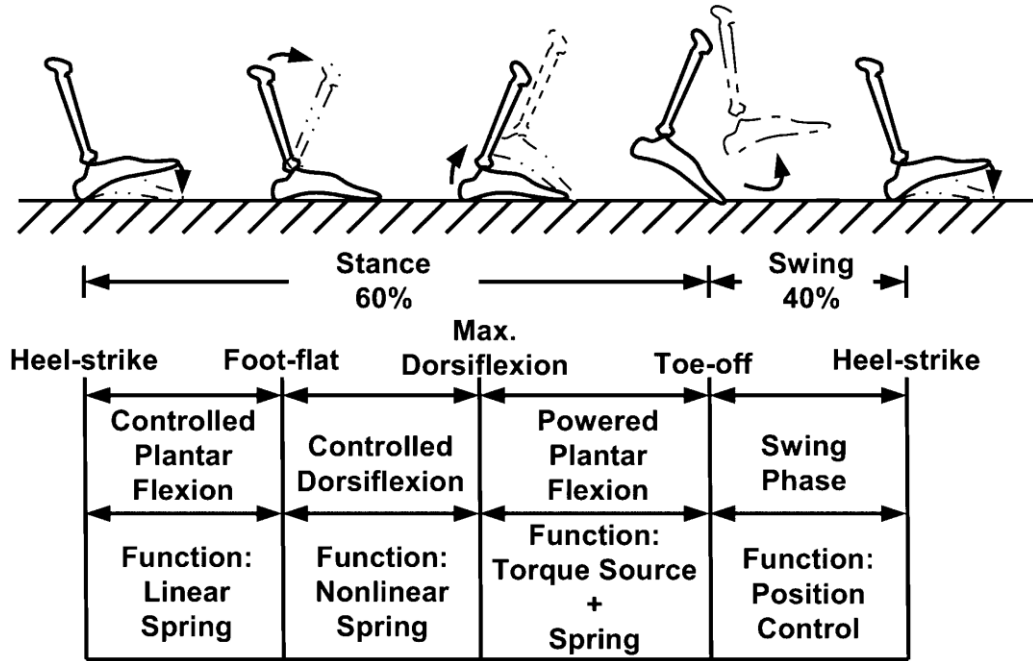


Figure 2-1: Human ankle biomechanics for level-ground walking from Au et al. (2009)

Figure 2-2 shows the average ankle torque with respect to the ankle angle for a normal person with intact limbs walking at a moderate speed (1.25 m/sec) [2]. As Fig. 2-2 indicated the ankle joint behavior during CP is consistent with a linear rotational spring response with joint torque proportional to joint position. In Fig. 2-2, segment (1) to (2) represents a linear spring behavior of the ankle. During the CD phase, ankle torque versus ankle position can be considered as a nonlinear spring where stiffness increases as ankle position increases. Segment (2) to (3) in Fig. 2-2 illustrates this nonlinear spring behavior of the ankle joint. Powered plantarflexion (PP) phase is also called push-off phase in which additional energy is generated

along with the spring energy stored during the CP and CD phase to achieve high plantarflexion. In this phase, the ankle can be considered as a torque source in parallel with CD spring. During SW phase, the ankle is a position source to indicate foot clearance as well as to reset the foot to a desired equilibrium position before the next heel strike [2].

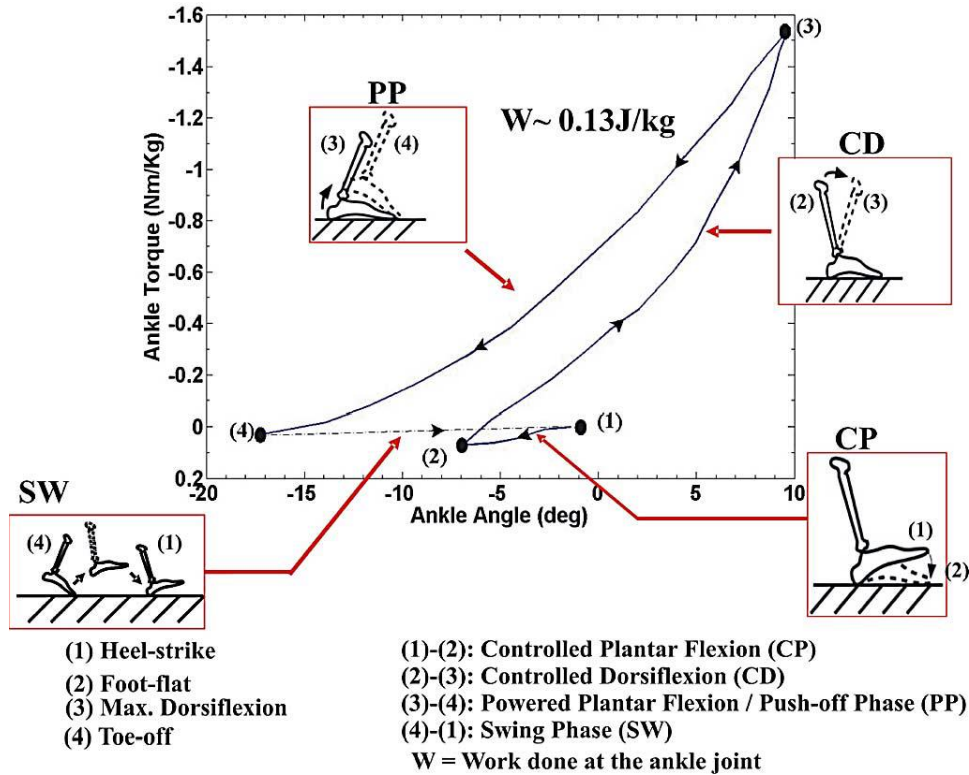


Figure 2-2: A typical ankle torque vs. angle behavior for a person walking at moderate speed (1.25 m/sec) from Au et al. (2009)

In summary, during walking, human ankle serves three major functions: (1) provides support and balance as a spring with variable stiffness; (2) provides additional net power for push-off; and (3) controls the foot to a desired equilibrium position in order to be ready for the next gait cycle. Most of the research on below-knee prosthesis focuses on improving amputees' level ground walking experience by achieving those functions mentioned above as much as possible compare to an intact ankle joint.

2.2 STATE-OF-THE-ART TRANSTIBIAL PROSTHESES

Lower-limb prosthetic devices range from simple mechanical joints to advanced computer controlled powered joints. Those devices can be categorized into energetically passive and powered groups. Each device has its own inherent strengths and weaknesses based on the user's activity and fitness level. Below-knee prosthetic devices will be discussed in this section, which includes the currently available prosthetic devices and the current research in this area.

A modern energetic passive device means that the device does not produce any active net power to assist the user during walking gait. Those prosthetic devices or prosthetic feet are serving as the anatomic foot and ankle for the amputees, thus providing cushioning and shock absorption at heel strike section, supporting the whole weight of the body during stance phase, etc. A typical example of the passive feet which have been widely used is the solid ankle or cushioned heel (SACH) foot as shown in Fig. 2-3 (a). The SACH foot is composed of a rigid longitudinal keel with a solid ankle covered with a wedge of polyurethane foam. When weight is applied to the heel, the foam will be compressed, thus simulating hyperextension of the foot during late stance. However, due to the rigidity of the SACH foot itself, dorsiflexion of the foot cannot be achieved. The next type of prosthetic foot design is the single axis foot, with which both plantar flexion and dorsiflexion of the foot can be accomplished, as shown in Fig. 2-3 (b). For active amputees who have the ability to move beyond basic ambulation skills, another type of prosthetic foot has been developed which can absorb the shock and store the energy during heel contact and middle stance, then release the stored energy during late stance to simulate “push-off” characteristics of the normal ankle. The Össur’s Flex-Foot shown in Fig. 2-3 (c) is a typical example of such kind of prosthetic feet. The most advanced passive below-knee prosthesis currently available is the Össur’s Proprio Foot® shown in Fig. 2-3 (d). It has an

electric motor to adjust the orientation of a low profile Flex-Foot during the swing phase of walking in order to clear the contact of the ground and adjust to irregular terrain to avoid stumbling. Although it is powered during the swing phase, the prosthesis behaves equivalently to a passive device as its ankle joint is locked during the stance phase.



Figure 2-3: (a) SACH foot (Ohio Willow Wood); (b) Single-axis foot (Ohio Willow Wood); (c) Flex-Foot® Assure (Össur); (d) Össur Proprio Foot® (Össur).

Below-knee prosthetics research has experienced significant technological advances in recent years. Developing a compact and powerful actuation system in powered prosthetics is a key challenge. Different actuation methods have been used, which include: pneumatic cylinder, pneumatic muscle, and electric motor, etc, while each of them has its own benefits and drawbacks.

In the early research efforts by Klute *et al.* [3], the first powered ankle-foot prosthesis was developed using McKibben pneumatic actuators which is capable of providing net positive power. Versluys *et al.* [4] also designed a powered prosthetic foot using pleated pneumatic artificial muscles. The muscles were arranged in a slider-crank configuration and the device can generate the peak torque of 200 N-m. Experimental tests were also conducted on an amputee and the subject felt the provided ankle torque helped to assist them forward. Wu *et al.* [5], presented a novel transfemoral prosthesis which includes a powered knee and ankle joint using pneumatic artificial muscles with spring return mechanism. Walking experiment results demonstrated that the prosthesis was able to provide a walking gait similar to that of a healthy person. Sup *et al.* [6] used pneumatic cylinders in slider-crank mechanisms to power both the knee and ankle. The design was capable of mimicking the torque curve of a 75 kg user, and joint compliance can be achieved by varying the pneumatic pressures within the cylinders.

In the existing works in powered transtibial prostheses, the major technical approach is electric actuation, combining electromagnetic actuator (i.e., DC motor) with electrochemical batteries. One commercially available powered transtibial prosthetic foot, the PowerFoot BiOM which is produced by BionX™ Medical Technologies, Inc (originally founded in 2007 as iWalk) [7], is the culmination of the work presented by Au and Herr *et al.* shown in Fig. 2-4 [2,8,9]. The PowerFoot BiOM has an electric motor in series with a unidirectional spring to provide a positive net power at the ankle joint to satisfy the design specifications dictated by normal human ankle walking biomechanics. By providing the ankle joint with power and torque, Au *et al.* demonstrated in their work that the average metabolic energy consumption has been reduced about 14% for normal walking at self-selected walking speeds in comparison with conventional

passive foot and ankle prosthetic devices [2]. Although the cost of the device is very high, the PowerFoot BiOM is still a significant progress in the prosthetic field [10].



Figure 2-4: BionX™ PowerFoot BiOM

In addition to the powered prosthetic foot developed by biomechatronics group at MIT mentioned above, another typical work also adopting this approach is the development of SPARKy (Spring Ankle with Regenerative Kinetics) ankle prosthesis by Hitt *et al.* [11]. The design utilizes a ball screw actuated by a set of electric motors to provide a positive net torque at the ankle joint. Two actuators are used due to the additional ankle joint torque required for running and jumping. It also has two degrees of freedom: plantar flexion and dorsiflexion and rotation of the ankle joint about the sagittal plane. The SPARKy prosthesis also has been developed as the commercial version by SpringActive, Inc. [12] which is now called Odyssey as shown in Fig. 2.5.



Figure 2-5: Odyssey (SpringActive, Inc)

Recent work done by the Center for Intelligent Mechatronics at Vanderbilt University [13,14] also developed a powered transtibial prosthesis that incorporates electric brushless motor with a parallel spring which can generate a peak ankle joint torque of approximately 110 Nm. The walking controller is a finite-state impedance-based controller which emulates a series of passive impedance functions at the joint. A prototype was shown in Fig. 2-6. Walking experiments were also conducted at multiple cadences to demonstrate the powered prosthesis can reproduce the essential biomechanical aspects similar to a healthy joint.

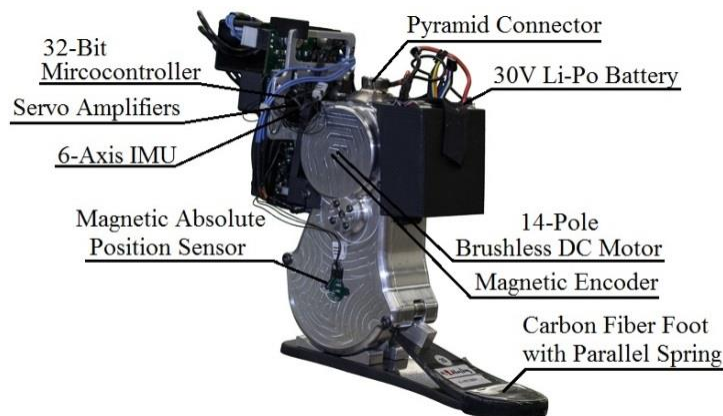


Figure 2-6: Powered ankle prosthesis from Shultz et al. (2014)

REFERENCES

- [1] Perry, J., & Davids, J. R. (1992). Gait analysis: normal and pathological function. *Journal of Pediatric Orthopaedics*, 12(6), 815.
- [2] Au, S. K., Weber, J., & Herr, H. (2009). Powered Ankle--Foot Prosthesis Improves Walking Metabolic Economy. *IEEE Transactions on Robotics*, 25(1), 51-66.
- [3] Klute, G. K., Czerniecki, J., & Hannaford, B. (1998). Development of powered prosthetic lower limb. In *Proceedings of the 1st National Meeting, Veterans Affairs Rehabilitation Research and Development Service*.
- [4] Versluys, R., Desomer, A., Peeraer, L., Van Gheluwe, B., & Lefever, D. (2007, January). Design of a Powered Below Knee Prosthesis. In *12th World Congress of the International Society for Prosthetics and Orthotics (ISPO) 2007, book of abstracts* (p. 455).
- [5] Wu, M., Driver, T., Wu, S. K., & Shen, X. (2014). Design and Preliminary Testing of a Pneumatic Muscle-Actuated Transfemoral Prosthesis. *Journal of Medical Devices*, 8(4), 044502.
- [6] Sup, F., Bohara, A., & Goldfarb, M. (2008). Design and control of a powered transfemoral prosthesis. *The International journal of robotics research*, 27(2), 263-273.
- [7] BionX™ Medical Technologies, Inc. (2015). Retrieved from <http://www.bionxmed.com/>
- [8] Au, S. K., Weber, J., & Herr, H. (2007, June). Biomechanical design of a powered ankle-foot prosthesis. In *Rehabilitation Robotics, 2007. ICORR 2007. IEEE 10th International Conference on* (pp. 298-303). IEEE.
- [9] Au, S. K., & Herr, H. M. (2008). Powered ankle-foot prosthesis. *IEEE Robotics & Automation Magazine*, 15(3).
- [10] Palmer, W. (2011) PowerFoot seeks to redefine human prosthetics. [Web log post]. Retrieved from <https://massacademy.wordpress.com/2011/02/24/powerfoot-seeks-to-redefine-human-prosthetics-2/>
- [11] Hitt, J. K., Bellman, R., Holgate, M., Sugar, T. G., & Hollander, K. W. (2007, January). The sparky (spring ankle with regenerative kinetics) project: Design and analysis of a robotic transtibial prosthesis with regenerative kinetics. In *ASME 2007 International Design Engineering Technical Conferences and Computers and Information in Engineering Conference* (pp. 1587-1596). American Society of Mechanical Engineers.

- [12] SpringActive, Inc. (2015). Retrieved from <http://www.springactive.com/>
- [13] Shultz, A. H., Mitchell, J. E., Truex, D., Lawson, B. E., Ledoux, E., & Goldfarb, M. (2014, August). A walking controller for a powered ankle prosthesis. In *Engineering in Medicine and Biology Society (EMBC), 2014 36th Annual International Conference of the IEEE* (pp. 6203-6206). IEEE.
- [14] Shultz, A. H., Mitchell, J. E., Truex, D., Lawson, B. E., & Goldfarb, M. (2013, May). Preliminary evaluation of a walking controller for a powered ankle prosthesis. In *Robotics and Automation (ICRA), 2013 IEEE International Conference on* (pp. 4838-4843). IEEE.

CHAPTER 3: CONCEPT, DESIGN AND APPLICATION OF SLEEVE MUSCLE ACTUATOR

3.1 INTRODUCTION

In the modern robotics research, biomimetics has become one of the major methods to bring continuous innovation to this area. By mimicking the structure and functioning mechanism of humans or animals, a biologically-inspired robotic system leverages the underlying biological principles, and thus enjoys similar advantages of its biological counterparts. Specifically for the actuation of biologically inspired robotic systems, investigators have expended significant efforts in developing the robotic counterpart of the biological muscle. Such efforts resulted in various types of muscle actuators, including pneumatic muscle actuators [1], piezoelectric actuators [2], shape memory alloy actuators [3], dielectric elastomer actuators [4], etc. Among these various choices, pneumatic muscle has drawn heavy attention from researchers as a highly competitive choice for bio-robotic systems, especially those serving human-assistance purposes (prostheses, orthoses, etc.). Also known as McKibben muscle and fluidic muscle, the pneumatic muscle simulates the functioning mechanism of biological skeletal muscles through the pressurizing of an air-tight tube surrounded by an inextensible mesh as shown in Fig. 3-1. With the interior volume pressurized, the tube expands in the radial direction and shortens in the axial direction, generating a contraction force to the external load. With this structure, the pneumatic muscle

possesses multiple unique advantages, including simple structure, high power density, and similar elastic characteristics to biological skeletal muscles.

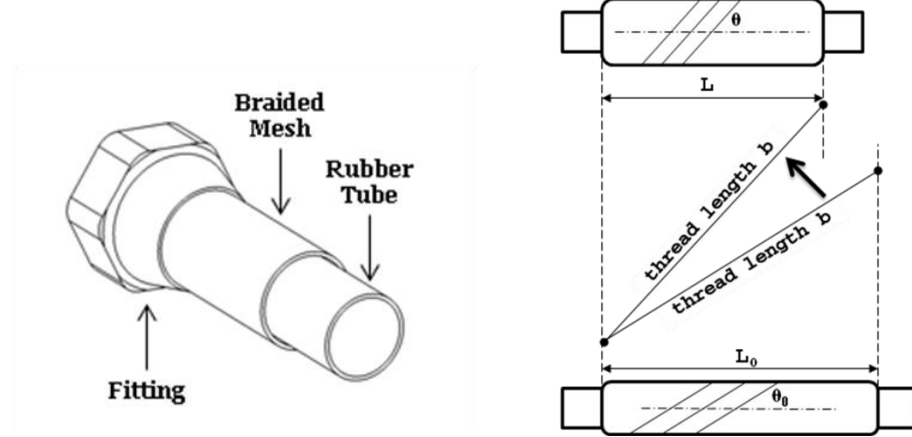


Figure 3-1: Structure (a) and actuation mechanism (b) of the pneumatic muscle.

Researchers have reported the power density values ranging from 1 kW/kg [5] to 10 kW/kg [6], significantly higher than the typical value for electric motors (~ 0.1 kW/kg as reported by Isermann and Raab [7]). The advantage in power density enables a large power output within a compact package, and thus makes the pneumatic muscle a highly competitive actuation approach for the robotic systems with strict weight and volumetric constraints. Moreover, the actuation force decreases with the contraction, which can be utilized to simulate the elastic behavior of biological skeletal muscles [8]. With these unique characteristics, pneumatic muscle has seen extensive use in robotic systems. For example, pneumatic muscle has been used to drive lower-limb prosthetic devices [9] and rehabilitation exoskeleton systems [10,11].

Despite the extensive robotic application of pneumatic muscle, the innovation of the actuator itself has been limited to its flexible membrane and the connection method. For example, the basic membrane structure as shown in Fig. 3-1(a) can be modified into an embedded design,

in which the load-bearing fibers are embedded into the flexible air-tight membrane to form a single-layer structure [12]. Also, Winters proposed a sleeved bladder muscle design, which consists of an air-tight bladder in a braid that is directly connected to an artificial tendon [13]. A more recent innovation is the pleated muscle concept by Daerden and Lefeber [14], in which the inflatable membrane is replaced with a flexible but non-extendible membrane folded along the longitude direction. Overall, these modifications did not change the basic structure or the functioning mechanism of the pneumatic muscle.

In this chapter, the authors propose a new class of pneumatic muscle actuator, namely sleeve muscle actuator, which represents a fundamental change in the structure of traditional pneumatic muscles. By incorporating a cylindrical insert in the center of the pneumatic muscle, the resulting sleeve muscle eliminates the central portion of the internal volume in the muscle. As a result of this structural change, the sleeve muscle enjoys a higher force output over its entire range of motion. Additionally, the significantly reduced internal volume also lowers the energy expenditure in operation. Based on this core concept, two types of sleeve muscle actuators are presented, including a single-acting type that enables the integration of the actuator with the load bearing structure, and a double-acting type that provides a unique capability of bi-directional actuation.

The chapter is organized as follows: Section 3.2 describes the inspiration of the general sleeve muscle concept; Section 3.3 presents the design and experimental results of the single acting sleeve muscle; Section 3.4 presents the design and experimental results of the double-acting sleeve muscle; Section 3.5 discusses the robotic applications of these two types of sleeve muscle actuators, and Section 3.6 presents the conclusions.

3.2 INSPIRATION OF THE SLEEVE MUSCLE CONCEPT

In the section, the working principle of pneumatic muscle is analyzed to form the theoretic basis and inspiration for incorporating the cylindrical insert to eliminate the central volume of pneumatic muscle. As described earlier, the pneumatic muscle actuator generates power output through the shortening of the flexible membrane under the internal pressure. In the meantime, the flexible membrane also expands radially, enlarging the internal volume of the actuator. To analyze the working mechanism of the pneumatic muscle, the principle of virtual work can be applied [15]. Neglecting the elastic straining energy in the membrane, the following equation can be obtained:

$$dW_{out} = dW_{in} \quad (3.1)$$

where W_{out} and W_{in} are the input work and output work, respectively. dW_{out} can be further expressed as

$$dW_{out} = -FdL \quad (3.2)$$

where F is the actuator contraction force and L is the length of the elastic part of the muscle. dW_{in} can be expressed as

$$dW_{in} = (P - P_{atm})dV \quad (3.3)$$

where P is the actuator internal pressure, P_{atm} is the atmosphere pressure, and V is the actuator internal volume. Combining the three equations above, the force output can be expressed as:

$$F = (-dV/dL) \cdot (P - P_{atm}) \quad (3.4)$$

As indicated by this equation, the contraction force F is proportional to the gauge pressure $(P - P_{atm})$, with the coefficient of proportionality as $(-dV/dL)$. Therefore, in order for the pneumatic muscle to generate a contraction force output, the internal volume V needs to

expand when the muscle length L shortens, resulting in a positive value of $(-dV/dL)$. To gain further insight into the actuation process, the internal volume V can be divided into two parts, including V_1 , a cylindrical volume at the center of the muscle, whose diameter is equal to that of the muscle's end connectors; and V_2 , a ring-shaped volume surrounding V_1 (Fig. 3-2).

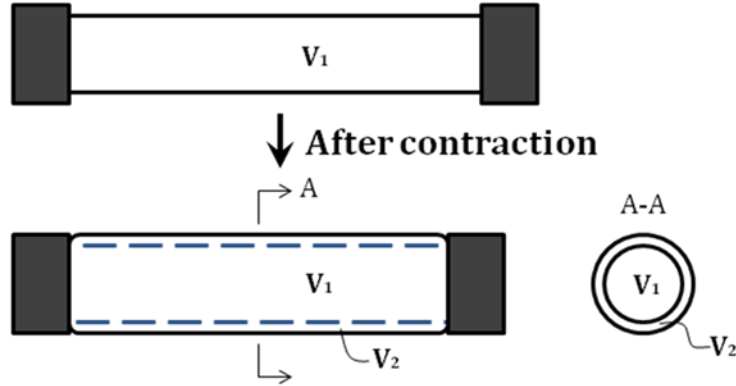


Figure 3-2: Dividing the internal volume into two parts: V_1 and V_2 .

Note that V_2 is negligible at the equilibrium state. Both V_1 and V_2 change with the length of the actuator, and thus the total contraction force can be expressed as the sum of F_1 and F_2 :

$$F = F_1 + F_2 \quad (3.5)$$

where F_1 and F_2 are the contributions of the changes of V_1 and V_2 , respectively:

$$F_1 = \left(-\frac{dV_1}{dL} \right) \cdot (P - P_{atm}) \quad (3.6)$$

$$F_2 = \left(-\frac{dV_2}{dL} \right) \cdot (P - P_{atm}) \quad (3.7)$$

To further analyze the contributions of these volume changes, V_1 can be expressed as the product of the fixed cross-sectional area $A_c = \frac{1}{4}D^2$ (D is the diameter of the muscle end connector) and the muscle length L , and thus decreases with the shortening of the muscle.

Consequently, the contribution of V_1 to the contraction force is always negative, as indicated by the following equation:

$$\frac{dV_1}{dL} = \frac{1}{4} D^2 > 0 \Rightarrow F_1 = \left(-\frac{dV_1}{dL} \right) \cdot (P - P_{atm}) = -A_C (P - P_{atm}) < 0 \quad (3.8)$$

On the other hand, V_2 expands with the shortening of the pneumatic muscle, and thus contributes positively to the generation of the output force:

$$\frac{dV_2}{dL} < 0 \Rightarrow F_2 = \left(-\frac{dV_2}{dL} \right) \cdot (P - P_{atm}) > 0 \quad (3.9)$$

Based on these two equations, it can be inferred that the total contraction force F is always less than F_2 , due to the fact that the negative F_1 reduces the total force output. This conclusion can be better explained with a simple force analysis as shown in Fig. 3-3.

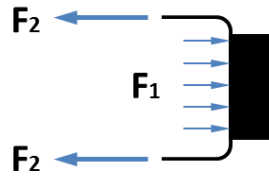


Figure 3-3: Contributions of V_1 and V_2 to the contraction force: F_1 is extension force due to the internal pressure, and F_2 is extension force by the membrane.

Among the two forces applied to the moving end of the pneumatic muscle, F_2 is the contraction force generated by the membrane, while F_1 is the extension force applied to the end connector due to the internal air pressure. When these forces are applied simultaneously, F_1 partially cancels out F_2 , resulting in a loss of the actuator force capacity. This observation inspired the basic concept of sleeve muscle actuator, which incorporates a cylindrical insert at the center of the muscle actuator with the purpose of eliminating F_1 .

3.3 SINGLE-ACTING SLEEVE MUSCLE ACTUATOR

Two specific forms of sleeve muscle actuator have been developed based on the basic concept described above. The first type is a single-acting (SA) sleeve muscle, in which a rigid cylindrical bar or tube is inserted into the center of the muscle actuator will be presented in this section as shown in Fig. 3-4.

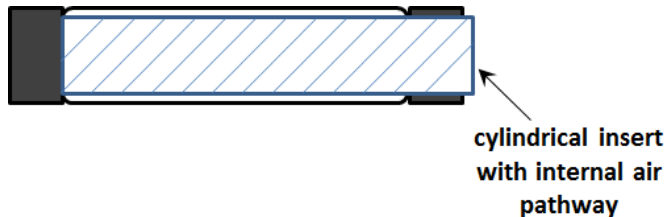


Figure 3-4: Schematic of the SA sleeve muscle actuator.

Note that the cylindrical insert incorporates a built-in air pathway to enable the access to the volume between the insert and the membrane. As such, the membrane is still able to generate the desired contraction force to the moving end, which now slides on the smooth outer surface of the insert. More importantly, with the central space occupied by the insert, the volume V_I is largely eliminated, which in turn eliminates the corresponding extension force F_I . Correspondingly, an increase in the actuator force capacity can be obtained:

$$\Delta F = -F_I = \frac{1}{4} \pi D_I^2 (P - P_{atm}) \quad (3.10)$$

where D_I is the outer diameter of the insert, which needs to be slightly less than the muscle end-connector diameter D to ensure the structural strength of the moving end. From Eq. (3.10), it can be deduced that, under a certain internal pressure, the magnitude of force increase is a constant, i.e., not affected by the contraction of the muscle. As such, this effect is especially important in

the large-contraction region, where the contraction force is much less than that at the equilibrium state. A comparison of the force curves is shown in Fig. 3-5.

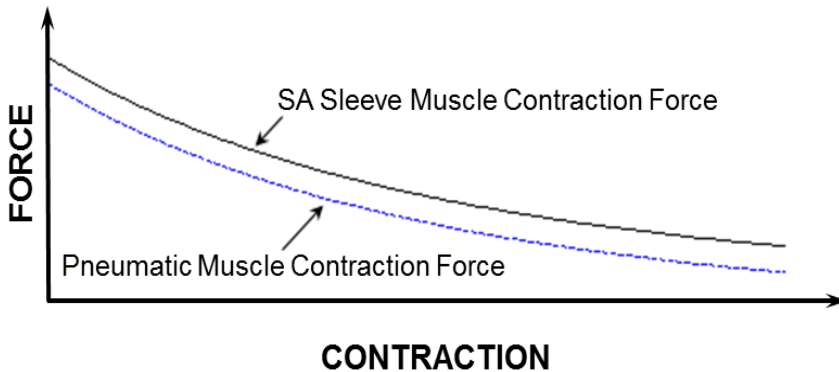


Figure 3-5: Comparison of force outputs under the same internal pressure.

In addition to the greater force capacity, the sleeve muscle also features a substantial reduction in energy consumption compared with the traditional pneumatic muscle. This can be primarily attributed to two factors: 1) The internal volume has been significantly reduced after incorporating the insert, and 2) With the greater force capacity, the sleeve muscle requires a lower air pressure to generate the desired force output, also contributing to the energy saving.

To evaluate the performance of the sleeve muscle actuator in comparison with traditional pneumatic muscles, a prototype of the SA sleeve muscle was fabricated and tested [16]. This prototype was developed based on a commercial pneumatic muscle (DMSP-40-180N-RM-CM, FESTO, Germany), as shown in Fig. 3-6. The end connectors of the commercial pneumatic muscle were drilled through to accommodate a cylindrical insert (Fig. 3-6 (b)). The insert is essentially a solid aluminum bar with an internal air pathway to enable the access to the internal volume of the sleeve muscle. The modified commercial pneumatic muscle is fixed to one end of the insert with proper sealing, while the other end slides on the surface of the insert for the power

output. Note that the outer diameter of the insert (35 mm) is slightly smaller than the inner diameter of the flexible membrane at the equilibrium state (40 mm), in order to maintain the strength of the hollow end connector. Also, an end cap structure is attached to the hollow end connector, which accommodates a U-cup to provide the sealing of the moving end. Finally, a U-shaped bracket is attached to the end cap for the connection to the external load while avoiding the interference with the insert structure (Fig. 3-6 (c)).



Figure 3-6: The design of the SA sleeve muscle prototype. (a) The end connectors of the commercial pneumatic muscle are drilled through to accommodate the insert; (b) The insert features an internal air pathway to enable the access to the internal volume; (c) the assembled SA sleeve muscle actuator.

The prototype was tested under a variety of conditions to characterize its performance in comparison with the original (unmodified) pneumatic muscle actuator. A typical experimental result is shown in Fig. 3-7, in which the force capacity of the sleeve muscle is compared with that of the original pneumatic muscle. As shown in the figures, the force output of the sleeve muscle is greater than that of the original pneumatic muscle over the entire range of contraction. Also, the predicted force output from the theoretical calculation poses a good match with the measured force output, demonstrating the validity of the theoretical analysis above. Experiments

have also been conducted to demonstrate the energy saving effects provided by the sleeve muscle. Depending on the percentage of muscle contraction, the energy consumption can be lowered by 20~37% compared with an identical pneumatic muscle without the insert [16].

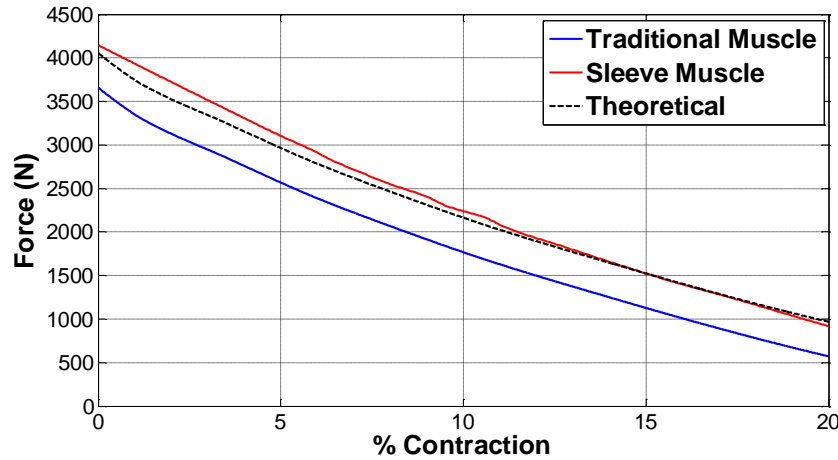


Figure 3-7: Measured and theoretically calculated force outputs of the SA sleeve muscle in comparison with the force output of the original unmodified pneumatic muscle under the gauge pressure of 414 kPa (60 psi).

3.4 DOUBLE-ACTING SLEEVE MUSCLE ACTUATOR

In addition to the single-acting sleeve muscle described in the previous section, a double-acting (DA) type of sleeve muscle has also been developed to further the potential of the approach of incorporating an insert into the muscle actuator. According to Eqns. (3.8) and (3.9), the contributions from V_1 and V_2 are totally opposite, so what if we separate them and let them contribute separately and independently to the actuation effort, as in Fig. 3-8 (a)? If this hypothetical structural change can be realized, the resultant muscle actuator can not only generate a greater contraction force but also generate an extension force for bi-directional actuation.

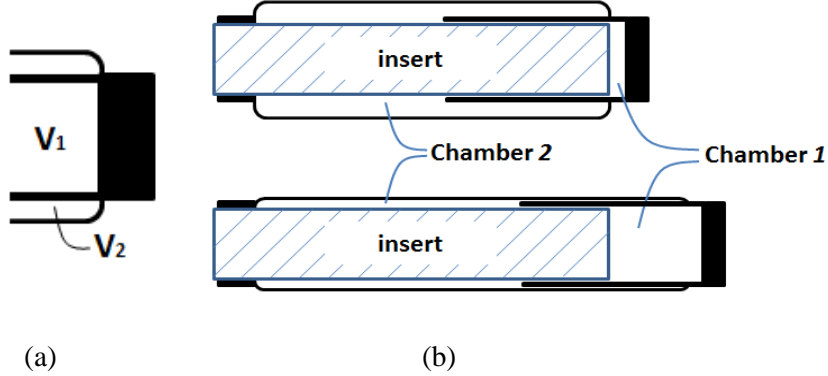


Figure 3-8: Concept of the DA sleeve muscle: (a) Separating V_1 and V_2 with a rigid shell;
(b) The resulting DA sleeve muscle structure.

The research inspired by the hypothetical question above leads to a new double-acting sleeve muscle actuator, as shown in Fig. 3-8 (b). Instead of simply eliminating V_1 , this new actuator introduces an additional pressurizable chamber (Chamber 1) over the moving end of the sleeve muscle. This additional chamber essentially isolates the portion of the original V_1 that is unaffected by the motion of the moving end, and thus retains the extension force associated with the volume V_1 . With this unique structure, the DA sleeve muscle features two separate chambers that can be individually pressurized or exhausted for contraction and extension, providing a truly bi-directional robotic actuator.

Based on the schematic in Fig. 3-8 (b), the force output can be expressed as a function of the pressures in the chambers. For the membrane pulling force, various theoretical or empirical models have been established with different levels of complexity and accuracy. To avoid losing generality in force calculation, assume the membrane force model takes the following form:

$$F_{PM} = F_{PM}(P, L) \quad (3.11)$$

in which P is the internal air pressure and L is the length of the actuator. For the DA sleeve muscle, the pressure applied to the membrane is the Chamber 2 pressure P_2 . Also, compared with

the pneumatic muscle, the DA sleeve muscle provides an increase in the force output as expressed by Eq. (3.10). As such, the contraction force of the DA sleeve muscle F_C can be expressed as:

$$F_C = F_{PM}(P_2, L) + \frac{1}{4} \pi D_I^2 (P_2 - P_{atm}) \quad (3.12)$$

For the extension force, the cross-sectional area is a constant $\frac{1}{4} \pi D_I^2$. As such, the extension force can be expressed as:

$$F_E = \frac{1}{4} \pi D_I^2 (P_1 - P_{atm}) \quad (3.13)$$

in which P_1 is the Chamber 1 pressure. Combining Eqns. (3.12) and (3.13), the force output of the DA sleeve muscle is:

$$F_{DASM} = F_{PM}(P_2, L) + \frac{1}{4} \pi D_I^2 (P_2 - P_1) \quad (3.14)$$

for which the contraction force is considered as positive. Based on this equation, a comparison of the force capacity of the DA sleeve muscle versus the traditional pneumatic muscle is shown in Fig. 3-9. From this figure, one can clearly see the increased contraction force capacity (positive) and the newly added extension force capacity (negative) provided by the DA sleeve muscle, indicating the significant performance enhancement of this new muscle actuator.

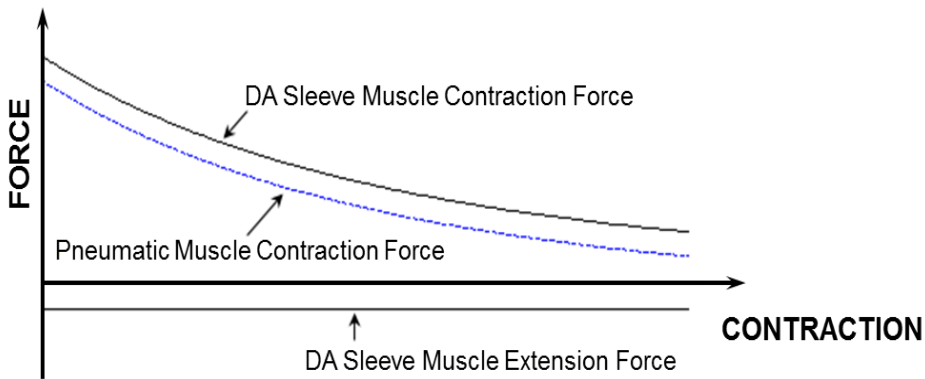


Figure 3-9: Force capacity of the DA sleeve muscle in comparison with that of the traditional pneumatic muscle.

Based on the schematic of the DA sleeve muscle, a prototype of the DA sleeve muscle has also been fabricated and tested [17]. The same commercial muscle from FESTO was selected as the basis for modification. Both ends of this commercial product were drilled through to accommodate the insert structure in the center, as shown in Fig. 3-10 (a). In order to attach a rigid shell to the moving end, a commercial pneumatic cylinder (Model 124-R, Bimba Manufacturing, University Park, IL, USA) was selected and modified. Specifically, on the rodless end of this single-acting cylinder is a cylindrical aluminum connector. After cutting the stainless steel body shell to the desired length (Fig. 3-10 (b)), the aluminum connector was fitted into the through hole in the muscle actuator to form the moving end. Teflon tape and adhesive were used to obtain the required sealing effect. On the stationary end, a solid aluminum insert is mounted to the through hole, and it provides the required air pathways to access the two chambers as shown in Fig. 3-10 (c). Also, two U-Cups, mounted in slots located close to the end of the insert, provide the sliding seal between the chambers during operation.

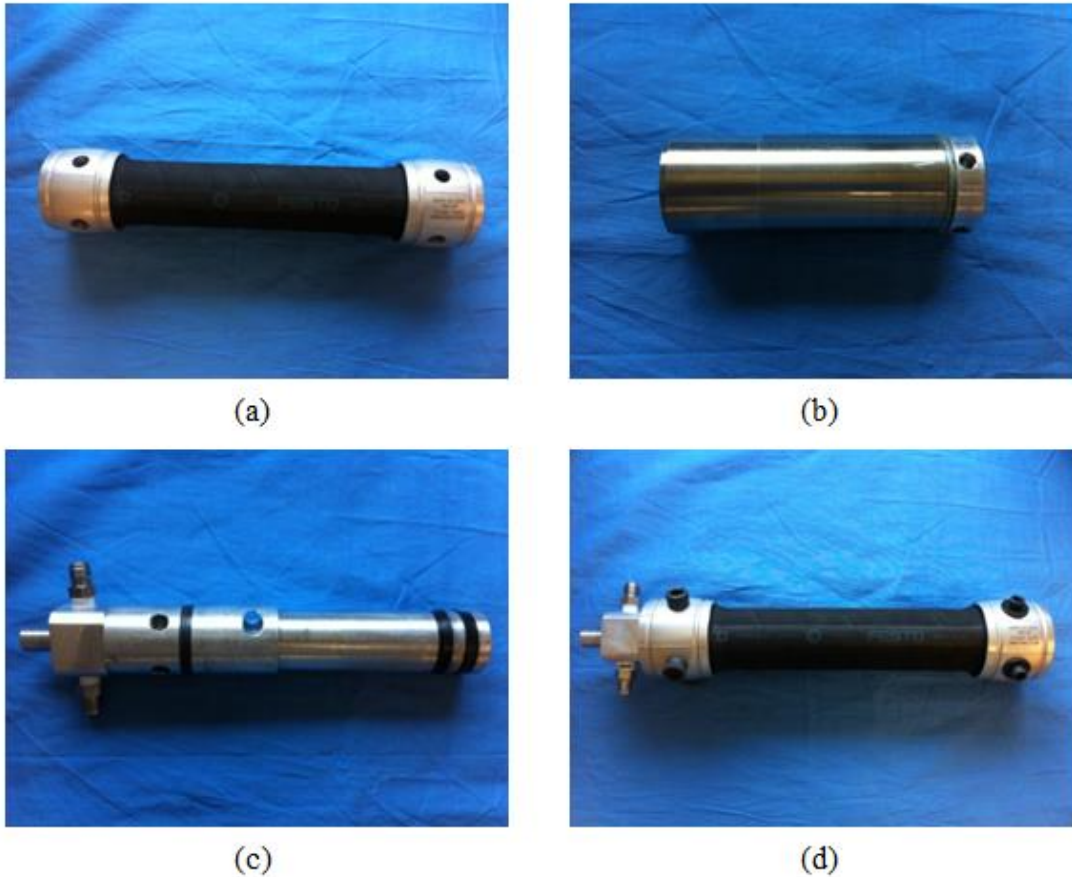


Figure 3-10: Prototype of the DA sleeve muscle: (a) Modified commercial pneumatic muscle; (b) Aluminum connector with stainless steel shell; (c) Solid aluminum insert mounted on the stationary end; (d) Assembled actuator prototype.

After the prototype was assembled (Fig. 3-10 (d)), experiments were conducted to characterize its force capacity under different internal pressures and contractions. The experimental apparatus is mounted horizontally on a vibration-isolated steel table, on which the fixed end is mounted on a stationary bracket. To alter the actuator length in the experiment, a winch was used to pull the free end of the actuator through a steel cable, with the actuator force measured through a load cell mounted between the actuator and the cable. Additionally, a linear potentiometer is attached to the moving end of the actuator to measure its displacement (and hence the contraction). To alter the internal pressure, a simple proportional control loop was

constructed, in which a proportional valve (MPYE-5-M5-010-B, FESTO, Esslingen, Germany) modulates the gas flow into or out of the muscle actuator, and a pressure transducer (SDET-22T-D25-G14-U-M12, FESTO, Esslingen, Germany) provides the pressure feedback. The control loop was implemented on a desktop computer that runs MATLAB Simulink Real-Time Workshop, which also recorded the measured force output of the muscle actuator. The primary focus of the experiments is to demonstrate the bi-directional actuation capability, and verify the force model Eq. (3.14). To serve this purpose, the force output was measured when the chamber pressures and actuator length took a wide range of values, and the measured data were compared with the theoretical values as calculated with Eq. (3.14). Two sets of typical data are shown in Fig. 3-11 and 3-12, with the corresponding block forces (at zero contraction) and free contractions (with zero force output) summarized in Table 3-1.

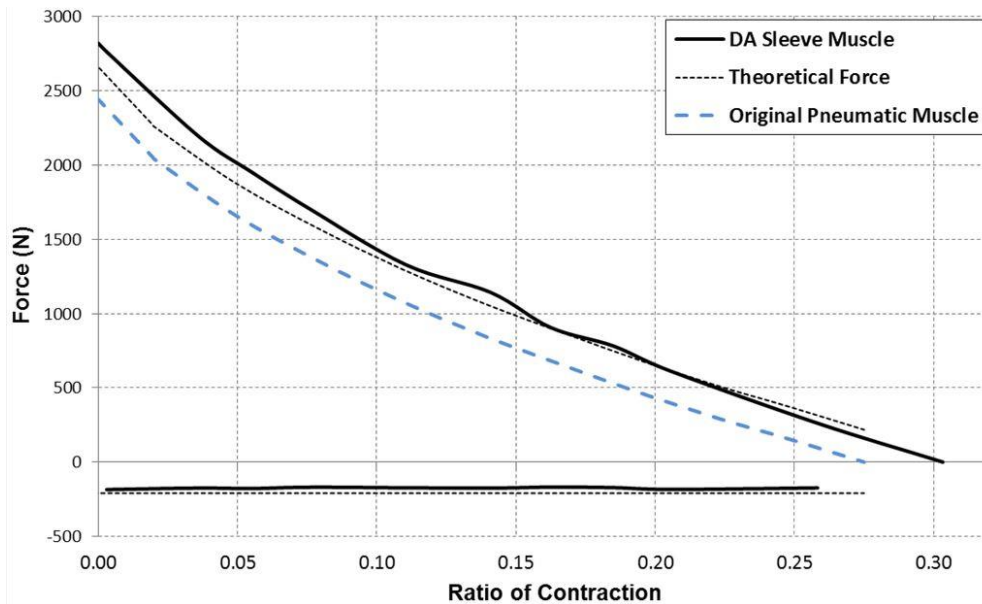


Figure 3-11: Measured and theoretically calculated force outputs of the DA sleeve muscle in comparison with the force output of the original unmodified pneumatic muscle under the gauge pressure of 276 kPa (40 psi).

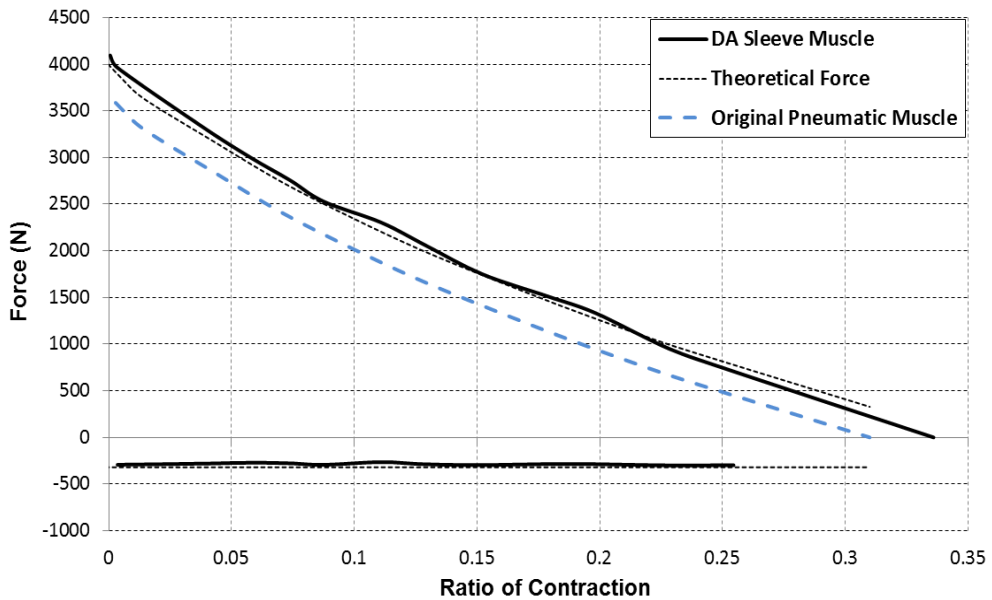


Figure 3-12: Measured and theoretically calculated force outputs of the DA sleeve muscle in comparison with the force output of the original unmodified pneumatic muscle under the gauge pressure of 414 kPa (60 psi).

Table 3-1: Comparison of block forces and free contractions.

	Pressure (psi)	Pressure (kPa)	Block force (N)	Free Contraction (%)
<i>Pneumatic Muscle</i>	40	276	2443	27.5
	60	414	3666	31.0
<i>DA Sleeve Muscle</i>	40	276	2820	30.3
	60	414	4096	33.6
<i>DA Sleeve Muscle Model</i>	40	276	2661	
	60	414	3994	
<i>% of Increase DASM vs PM</i>	40	276	15.4%	10.1%
	60	414	11.7%	8.4%
<i>% of Model Error</i>	40	276	5.6%	
	60	414	2.5%	

In the figures, the force-length curves of the pneumatic muscle (dashed lines in blue) were experimentally determined. Based on these curves, the theoretical force curves for contraction and extension (dashed lines in black) are calculated according to Eq. (3.14). As can be seen in these figures, the measured contraction force by DA sleeve muscle displays a consistent increase over the entire range of motion compared with that provided by the traditional pneumatic muscle. In addition, the DA sleeve muscle is able to provide an extension force that the traditional pneumatic muscle is not able to provide (the flat curves with negative values). As the extension force is provided by the telescoping insert with a constant cross-sectional area, the magnitude of the force is unaffected by the actuator length. Furthermore, the measured curves display a close match to the theoretic curves, demonstrating the validity of the pressure-force Eq. (3.14).

In addition to the force capacity, the energy density of the DA sleeve muscle has also been studied. The improved performance of the DA sleeve muscle is obtained by the introduction of the insert structure, which adds to the weight of the actuator. As such, to compare the DA sleeve muscle and the corresponding pneumatic muscle, the metric of specific work is used [18,19]. According to the measurement results, the original FESTO muscle weighs 0.69 kg, while the DA sleeve muscle prototype weighs 0.95 kg, with a 38% percentage increase in weight. On the other hand, the available energy of the DA sleeve muscle is increased to approximately 175 J, compared with the value of 149 J for the original FESTO muscle. As such, the DA sleeve muscle's specific work (184 J/kg) is only 15% lower than the original FESTO muscle's value (217 J/kg). Both of these values are an order of magnitude lower than the energy density of some light-weight pneumatic muscle models. For example, the pneumatic muscle developed by Woods *et al.* is able to provide a specific work of 4,400 J/kg [18]. When compared with other types of

actuators, the DA sleeve muscle's specific work is greater than those provided by solenoid actuators (~ 5 J/kg) and piezoelectric actuators (~ 1 J/kg), but less than those provided by shape memory alloy (SMA) actuators ($\sim 4,500$ J/kg) and pneumatic cylinders ($\sim 1,200$ J/kg) [18,19]. Note that the current DA sleeve muscle is only a prototype, which includes a nearly solid aluminum insert at the center, and thus has a significant potential for weight reduction. In the future, the weight of the DA sleeve muscle can be reduced by reducing the use of metal, e.g., redesigning the insert into a thin-wall structure, replacing the metal fitting with a carbon fiber structure, etc. Furthermore, peripheral components (such as the servo valve) can be incorporated into the DA sleeve muscle to form a highly integrated muscle actuator, with the details discussed in the subsequent section.

3.5 APPLICATION OF DA SLEEVE MUSCLE IN BIO-ROBOTICS

For the robotic application of this new actuator, it is important to identify the robotic systems that can make the best use of the unique asymmetric force capacity. Comparing the DA sleeve muscle with the traditional antagonistic pneumatic muscle actuation system, their displacement ranges are similar, but their force/torque capacities are vastly different. For the DA sleeve muscle, the contraction force capacity is far greater than the extension force capacity in the majority of the displacement range. As such, this actuator is most suitable for robotic applications with asymmetric force or torque requirements. In lower-limb prostheses, both knee and ankle display such asymmetric torque requirement. For the knee, the extension torque is much greater than the flexion torque; for the ankle, the plantar-flexion torque is much greater than the dorsiflexion torque. Such torque requirement is well studied and quantified. For example, Fig. 3-13 shows the torque trajectory of the ankle during level walking at a fast cadence,

with the data from Winter [20]. To meet such torque requirement, it is important to match the torque-demanding direction with the contraction of the muscle actuator to exploit its greater force capacity in this direction, as shown in the conceptual design schematic in Fig. 3-14. In this design, the DA sleeve muscle is placed behind the supporting tube and drives the ankle motion through an inverted crank-slider mechanism. As such, the match between the desired versus supplied torques can be obtained in both directions, making full use of the potential of the actuator and generating a highly efficient robotic design.

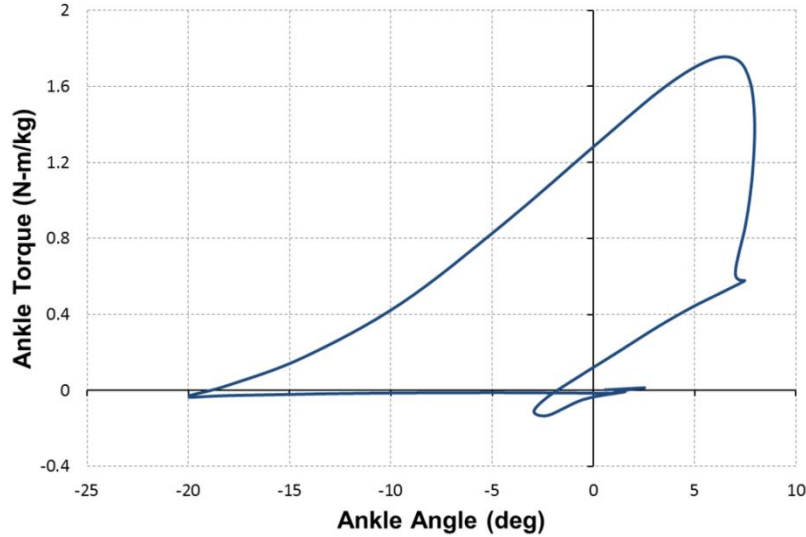


Figure 3-13: Body weight-normalized torque trajectory of the ankle in fast walking.

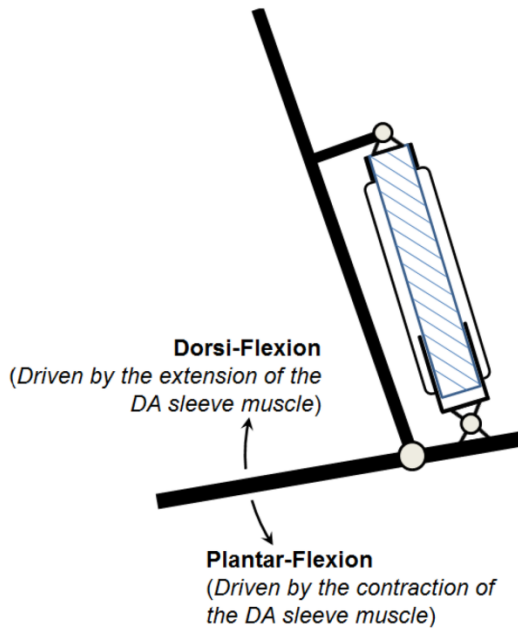


Figure 3-14: Conceptual design of a DA sleeve muscle-actuated robotic ankle.

3.6 CONCLUSIONS

In this chapter, a new class of muscle actuator, namely sleeve muscle actuator, which is based on the fundamental change in the structure of traditional pneumatic muscles, is presented. To introduce the rationale for this new actuator, an analysis was conducted, in which the internal volume of the traditional pneumatic muscle was divided into two parts and the contribution of each part was analyzed. The conclusion of this analysis led to the basic concept of incorporating a cylindrical insert to the center of the traditional pneumatic muscle, which forms the basis of the sleeve muscle actuator. Two types of sleeve muscle actuators were introduced, including a single-acting type with a fixed insert at the center, and a double-acting type with two chambers to provide bi-directional actuation capability. For each type of sleeve muscle, the basic structure was described in detail, and the force capacity was analyzed accordingly. Experimental results obtained on the prototypes were also summarized to validate the force capacity models.

REFERENCES

- [1] Schulte, H. F. (1961). The characteristics of the McKibben artificial muscle. *The application of external power in prosthetics and orthotics*, 874, 94-115.
- [2] Secord, T. W., Ueda, J., & Asada, H. H. (2008, May). Dynamic analysis of a high-bandwidth, large-strain, PZT cellular muscle actuator with layered strain amplification. In *Robotics and Automation, 2008. ICRA 2008. IEEE International Conference on* (pp. 761-766). IEEE.
- [3] Ikuta, K. (1990, May). Micro/miniature shape memory alloy actuator. *Proceedings of the IEEE International Conference on Intelligent Robots and Systems* (pp. 2156-2161). IEEE.
- [4] Baughman, R. H. (1996). Conducting polymer artificial muscles. *Synthetic Metals*, 78(3), 339-353.
- [5] Caldwell, D. G., Medrano-Cerda, G. A., & Goodwin, M. (1995). Control of pneumatic muscle actuators. *IEEE Control Systems*, 15(1), 40-48.
- [6] Hannaford, B., & Winters, J. (1990). Actuator properties and movement control: biological and technological models. In *Multiple Muscle Systems: Biomechanics and Movement Organization*, Chapter 7, 101-120. Springer New York.
- [7] Isermann, R., & Raab, U. (1993). Intelligent actuators—Ways to autonomous actuating systems. *Automatica*, 29(5), 1315-1331.
- [8] Klute, G. K., Czerniecki, J. M., & Hannaford, B. (2002). Artificial muscles: Actuators for biorobotic systems. *The International Journal of Robotics Research*, 21(4), 295-309.
- [9] Versluys, R., Desomer, A., Lenaerts, G., Van Damme, M., Beyl, P., Van der Perre, G., ... & Lefever, D. (2008, October). A pneumatically powered below-knee prosthesis: Design specifications and first experiments with an amputee. In *Biomedical Robotics and Biomechatronics, 2008. BioRob 2008. 2nd IEEE RAS & EMBS International Conference on* (pp. 372-377). IEEE.
- [10] Sawicki, G. S., & Ferris, D. P. (2009). A pneumatically powered knee-ankle-foot orthosis (KAFO) with myoelectric activation and inhibition. *Journal of Neuroengineering and Rehabilitation*, 6(1), 23.
- [11] Ferris, D. P., Czerniecki, J. M., & Hannaford, B. (2005). An ankle-foot orthosis powered by artificial pneumatic muscles. *Journal of applied biomechanics*, 21(2), 189-197.

- [12] Baldwin, H. A. (1969). Realizable models of muscle function. In *Biomechanics* (pp. 139-147). Springer US.
- [13] Winters, J. M. (1990). Braided artificial muscles: Mechanical properties and future uses in prosthetics/orthotics. In *Proceedings of the RESNA 13th annual conference* (pp. 173-174).
- [14] Daerden, F., & Lefeber, D. (2001). The concept and design of pleated pneumatic artificial muscles. *International Journal of Fluid Power*, 2(3), 41-50.
- [15] Chou, C. P., & Hannaford, B. (1996). Measurement and modeling of McKibben pneumatic artificial muscles. *IEEE Transactions on Robotics and Automation*, 12(1), 90-102.
- [16] Driver, T., & Shen, X. (2013). Sleeve muscle actuator: Concept and prototype demonstration. *Journal of Bionic Engineering*, 10(2), 222-230.
- [17] Zheng, H., & Shen, X. (2013, November). Double-acting sleeve muscle actuator for bio-robotic systems. In *Actuators* (Vol. 2, No. 4, pp. 129-144). Multidisciplinary Digital Publishing Institute.
- [18] Woods, B. K., Kothera, C. S., & Wereley, N. M. (2011). Wind tunnel testing of a helicopter rotor trailing edge flap actuated via pneumatic artificial muscles. *Journal of Intelligent Material Systems and Structures*, 22(13), 1513-1528.
- [19] Huber, J. E., Fleck, N. A., & Ashby, M. F. (1997, October). The selection of mechanical actuators based on performance indices. In *Proceedings of the Royal Society of London A: Mathematical, Physical and Engineering Sciences* (Vol. 453, No. 1965, pp. 2185-2205). The Royal Society.
- [20] Winter, D. A. (1991). *Biomechanics and motor control of human gait: normal, elderly and pathological*. 2nd edition, Waterloo, ON, University of Waterloo Press.

CHAPTER 4: DESIGN AND CONTROL OF PNEUMATICALLY ACTUATED TRANSTIBIAL PROSTHESIS

4.1 INTRODUCTION

For a lower extremity prosthesis, the primary purpose is to restore the locomotive functions of lost limb sections and joints. Traditionally, such functions have been restored by energetically passive devices, i.e., devices that only dissipate energy, or store and reuse energy within a gait cycle. The passive nature of such devices is fundamentally different from the energetic role of the corresponding biological joints, and thus poses a significant limitation to their functionalities and rehabilitation effects. For example, biomechanical studies on human locomotion highlight the important energetic role of the ankle joint. In level walking, the ankle produces substantially more work than that of the knee and hip [1]. Unlike the knee, the ankle's energetic behavior in level walking is clearly and significantly positive (i.e, integration over a cycle of power data is clearly and significantly positive) [2]. As such, for an amputee fitted with a passive transtibial prosthesis, he or she has to expend more power on the unaffected biological joints to compensate for the lack of power generation in the prosthetic ankle, resulting in an asymmetric gait and greater energy consumption [3,4].

To address this important issue, a considerable amount of research has been conducted on the development of energetically active transtibial prostheses with powered ankle joints. In such efforts, the primary challenge is to generate sufficient power and torque output within a compact

form factor. In the existing works, the major technical approach is electric actuation, combining electromagnetic actuator (i.e., DC motor) with electrochemical batteries. Typical works adopting this approach include the powered ankle-foot prostheses developed by the Biomechatronics group at MIT [5-7], the two degrees of freedom SPARKy ankle prosthesis [8,9], and the powered transfemoral prostheses developed by the Center for Intelligent Mechatronics at Vanderbilt University (which include powered ankle joints) [10-12]. In spite of the improved gait quality provided by these active devices, they tend to suffer from multiple inherent weaknesses of an electric actuation system, primarily the heavy weight of the actuator and the short battery life limit the duration of operation.

Unlike the aforementioned works, the research presented in this chapter takes a different technical route to address this challenging issue. Instead of electric actuation, the transtibial prosthesis design in this paper utilizes pneumatic actuation, which is well known for its capability of generating large force and power output with light weight and compact volumetric profile [13]. Leveraging this unique advantage, Sup *et al.* developed a powered transfemoral prosthesis, in which both knee and ankle joints are powered with pneumatic cylinders [14]. Note that, in this design, the ankle actuator shares the “shank” space with the knee actuator, and thus it cannot be isolated to form a standalone transtibial prosthesis. There have also been attempts of utilizing pneumatic muscle actuators in transtibial prosthesis design [15], and walking experiments have been conducted to demonstrate the feasibility of this new actuation approach [16]. However, a pneumatic muscle actuator expands radially during operation, which requires additional clearance from the supporting structure and enlarges the volumetric profile of the prosthesis.

Different from these earlier attempts, the work presented in this chapter aims at developing a highly compact transtibial prosthesis with a potential for future practical use in amputees' daily life. To achieve this goal, the design of the prosthesis is based on the pneumatic cylinder actuator. A cylinder-type actuator does not expand in operation, which enables it to be placed horizontally under the rotational axis of the ankle. This spatial arrangement minimizes the height of the prosthesis, enlarging the population that can potentially benefit from this device. There are three specific objectives in this work, which will be detailed in the following sections: Designing the pneumatically actuated transtibial prosthesis (section 4.2); Developing a prosthesis control algorithm for walking (section 4.3); (3) Conducting preliminary testing on a transtibial amputee (sections 4.4).

4.2 PROTHESIS DESIGN

4.2.1 DESIGN SPECIFICATIONS

Ideally, a transtibial prosthesis should restore the lost limb functions in supporting the body weight and providing torque/power output for locomotion. Meanwhile, the weight and volumetric profile of the prosthesis should be kept under those of the corresponding limb segments for daily-use comfort and aesthetic reason. As such, the design specifications are primarily determined according to principles in human anatomy and biomechanics of locomotion. Furthermore, for the development of this first prototype, off-the-shelf commercial products are preferred for the choices of major components, with the purpose of reducing the cost and risk in the prosthesis design, fabrication, and testing.

The weight and volumetric profile of the prosthesis are determined for a male subject of 75 kg, approximately 50th percentile in weight. The height of the prosthesis should be

comparable with or lower than that of a traditional high-profile transtibial prosthesis, which is approximately 180 mm from ground to the prosthetic adapter [17]. Taking the nominal height of a typical user at 1.75 m, the percentage of the missing limb mass under 180 mm from the ground surface (versus the entire body mass) is approximately 2.5% [18]. Multiplying the percentage to the nominal body weight, the mass of the missing limb segment is approximately 1.875 kg, which serves as the upper limit for the weight of the prosthesis.

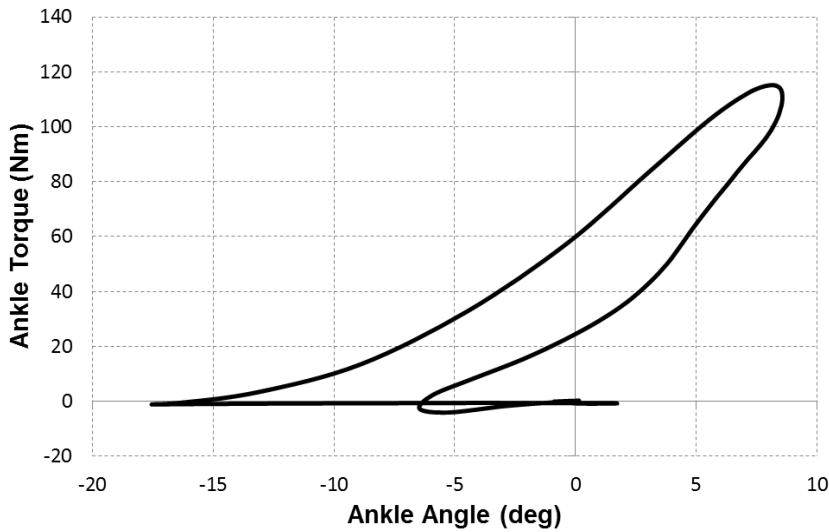


Figure 4-1: The torque trajectory of the ankle in slow walking (data from [2]).

The kinematic and kinetic specifications are determined according to the biomechanical data of ankle joint in walking. Note that the ankle motion is relatively slow in comparison with the knee, and thus the joint velocity is not considered as a major concern. Therefore, the design calculation is primarily focused on meeting the requirements in actuation torque and range of motion. According to the data by Winter [2], a joint angle-torque plot (for slow walking) is shown in Fig. 4-1. As indicated in this figure, the peak torque is approximately 115 Nm, which occurs at the joint angle of 8°. Note that the torque is a function of joint angle, and thus the

prosthetic ankle should ideally cover the entire torque trajectory of walking. This serves as the design goal for the torque capacity of the prosthetic ankle joint. Additionally, the range of motion is determined to be at least $-20^\circ \sim 10^\circ$, which covers the entire joint angle trajectory in walking.

4.2.2 MECHANICAL DESIGN

The mechanical design of the prosthesis is largely driven by the need for a compact package of the device. Specifically, reducing the prosthesis height is considered as a major goal to fit the amputees with amputation sites close to the ankle. Existing powered transtibial prostheses usually cannot be fitted to such patients due to their large heights compared with unpowered devices. A schematic of the actuation mechanism is shown in Fig. 4-2. Unlike the existing designs of pneumatically-actuated ankles, the actuator is arranged in the horizontal direction, driving the ankle motion through an inverted crank-slider mechanism. With this unique design, the actuator is completely under the rotation axis of the ankle joint, minimizing the height of the device.

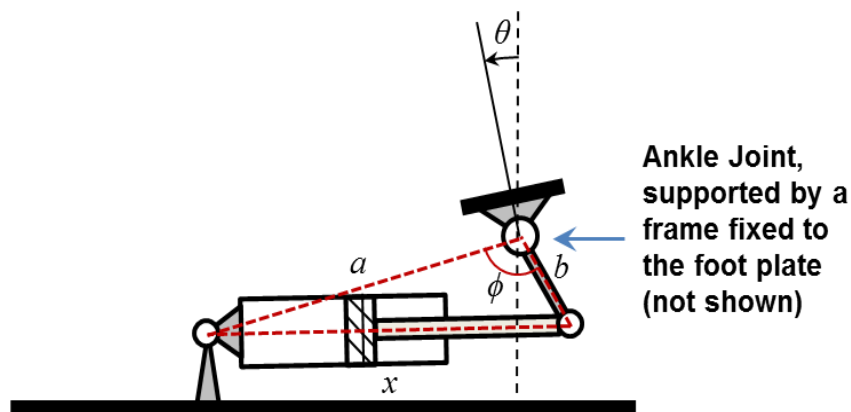


Figure 4-2: The actuation mechanism of the transtibial prosthesis.

Figure 4-2 also defines the design parameters are directly related to the kinematic and kinetic characteristics of the prosthesis, including the lengths a and b and the angle ϕ (when the ankle angle θ is zero). These parameters, combined with the bore size and stroke length of the actuators, determine the range of motion and the torque capacity of the prosthetic ankle joint. Specifically, the maximum actuation force provided by the pneumatic cylinders F_{MAX} is determined according to the maximum air pressure in the actuator (usually the supply gauge pressure P_s), in combination with the corresponding piston area A_p :

$$F_{MAX} = P_s \cdot A_p \quad (4.1)$$

where

$$A_p = \begin{cases} \pi D^2 & \text{for the rodless chamber} \\ \pi(D^2 - d^2) & \text{for the chamber with rod} \end{cases} \quad (4.2)$$

In the above equation, D is the piston diameter, and d is the rod diameter. Note that the piston areas in the two directions are slightly different due to the existence of the piston rod. To obtain the corresponding maximum torque, the method of virtual work can be applied, which results in the following equation:

$$\tau = F \cdot \frac{dx}{d\phi} \quad (4.3)$$

where τ is the torque corresponding to a certain actuation force F . According to the geometric relationships shown in Fig. 4-2, actuator length x can be expressed as a function of the angle ϕ according to the following equations:

$$x = \sqrt{a^2 + b^2 - 2ab\cos\phi} \quad (4.4)$$

Substitute Eq. (4.4) into (4.3), the following equation can be obtained

$$\tau = F \left(\frac{absin\phi}{\sqrt{a^2 + b^2 - 2abcos\phi}} \right) \quad (4.5)$$

Utilizing this equation, the torque capacity can be calculated according to the selected set of parameters. Note that, due to the prototype nature of the current device, off-the-shelf components are preferred. As such, the design parameters are determined by selecting a commercial pneumatic actuator and choosing the design parameters accordingly. In the current prototype, the actuator is a double-acting pneumatic cylinder (171.25-DP) in the Original Line from Bimba Manufacturing (University Park, IL, USA), with 38 mm (1.5 inches) bore size and 32 mm (1.25 inches) stroke. The other design parameters are listed in Table 4-1.

Table 4-1: The design parameters of the transtibial prosthesis prototype.

Parameter	Value	Unit
<i>a</i>	158	mm
<i>b</i>	46	mm
ϕ (when $\theta=0$)	98	°

The design described above is able to provide a range of motion of $-25^\circ \sim 15^\circ$, exceeding the kinematic requirement. The torque capacity (obtained under the maximum pressure of 2 MPa) is shown in Fig. 4-3, which also displays the required torque curve associated with slow walking. The actuation system is able to provide sufficient torque within the majority of the range of motion, while only the peak torque at $3\sim8^\circ$ is beyond the torque capacity curve. Note that it would be possible to use a pneumatic cylinder with a greater bore size to meet the peak torque requirement. However, a bigger cylinder would significantly increase the size of the prosthesis. As such, a relatively small cylinder is used to maintain the low volumetric profile of the prosthesis. It is worth mentioning that, as observed in the human subject experiments, the

lowered torque capacity did not seem to affect the user's gait quality, as demonstrated by the results obtained in walking experiments.

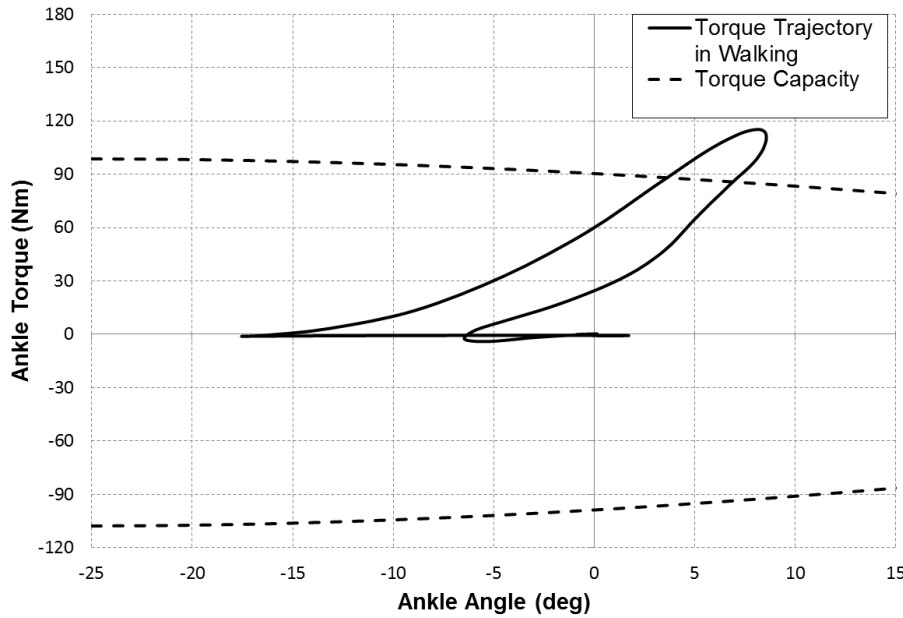


Figure 4-3: Comparison of the actuation torque capacity versus the ankle torque trajectory in walking.

Note that the design described above targets slow walking since it is the primary mode of motion for the majority of transtibial amputees, but the prosthesis can also be used for other locomotive modes. Within the same level walking mode, with the increase in speed, the maximum physiological torque increases slightly (from 115 Nm for slow walking to 122 Nm for natural walking and 130 Nm for fast walking), and high torque output (>100 Nm) spans a wider angular range (from $\sim 3.5^\circ$ for slow walking to $\sim 5.5^\circ$ for natural walking and $\sim 7.5^\circ$ for fast walking), according to the data from Winter [2]. As such, an amputee user fitted with the prosthesis will experience more difficulty when walking at higher speed. For stair ascent and descent, the maximum physiological torques are lower than that for slow walking (96 Nm for

stair ascent and 85 Nm for stair descent), according to the data from Riener *et al.* [19]. The prosthesis is expected to provide sufficient torque for these modes. For sloped walking, biomechanical data obtained by McIntosh *et al.* [20] indicate that there is an increase in peak torque for both upslope and downslope walking, with the only exception of 5° upslope walking (in which the peak torque decreases by ~50% compared with that for level walking). As such, an amputee with the prosthesis may also experience difficulty in sloped walking except in small-incline upslope walking. In summary, the prosthesis can provide sufficient torque capacity for slow walking and stair ascent/descent, but has difficulty in providing the high peak torques associated with faster walking and sloped walking.

After the design parameters are determined, the authors also conducted an analysis on the attainable speed of the prosthetic joint to verify that the prosthesis is able to provide the desired ankle speed in gait. According to the related biomechanical data [2], the maximum angular velocity of the ankle in slow walking is approximately 2.97 rad/s. On the other hand, for the pneumatic cylinder-type actuators, the maximum linear velocity can reach as high as 1000 mm/s with oil-free air, and may reach higher speed if lubricated air is used [21]. For a conservative estimation, take 1000 mm/s as the attainable linear velocity for the cylinders. According to the design parameters listed in Table 4-1, the corresponding attainable joint velocity is 21.9~28.9 rad/s (depending on the joint angle), far exceeding the maximum angular velocity in gait.

4.2.3 INSTRUMENTATION AND THE COMPLETE PROSTHESIS PACKAGE

Multiple sensors are incorporated into the prosthesis design to provide the required information for the control prosthesis. The most important sensor signal required by the controller (to be described in the subsequent section) is the joint angle, which is provided by a

string potentiometer mounted in parallel with the actuator (ZX-PA-1.5 analog position transducer, UniMeasure, Corvallis, OR, USA). This string potentiometer measures the displacement of the piston rod, which can be translated into the joint rotation with simple trigonometric calculation. Additionally, for the modulation of the actuation force, a load cell (ELPF-T3E-500L, Measurement Specialties, Hampton, VA, USA) is mounted in line with the actuator. With the force signal measured with this load cell, a simple PID force control loop can be used to obtain the desired actuation force/torque to support the user's locomotion. With these sensors included, the total weight of the prosthesis is 0.9 Kg, and the height of the prosthesis is 98 mm, both far below their respective upper limits. The appearance of the prosthesis is shown in Fig. 4-4.

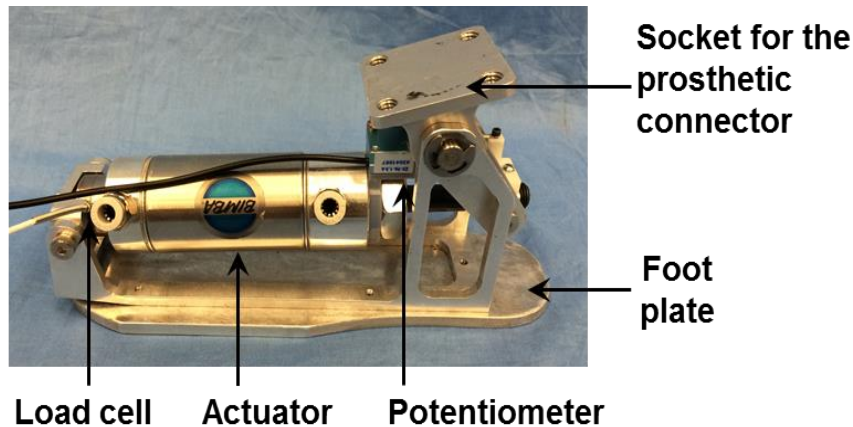


Figure 4-4: Photo of the prosthesis prototype when removed from the foot shell.

Currently, the control components of the prosthesis are implemented off-board, including the control valve (ZS-V-13000, Enfield Technologies, Shelton, CT, USA) and the control calculation. In the walking experiments, the valve was attached to the pylon mounted between the prosthesis and the user's prosthetic socket, and the controller was implemented on the National Instruments LabVIEW platform, running on a desktop computer. In the future, the

control valve, along with a microcontroller-based control system, will be integrated into the prosthesis itself. Furthermore, to form a completely self-contained prosthesis, a compact, portable pneumatic supply will also be incorporated. Two possible candidates are high-pressure carbon fiber compressed air tank and liquid propellant-based pneumatic supply [22]. A carbon fiber air tank stores compressed air under high pressure (up to 31 MPa, or 4500 Psi), and there are multiple commercial products on the market, primarily serving the purpose of powering paintball guns. The availability of commercial products makes it an ideal short-term solution. The alternative solution, liquid propellant-based supply, generates high-pressure gas through the catalytic reaction of liquid propellant. According to a study by Goldfarb *et al.* [22], a liquid-propellant-powered actuator offers an order of magnitude advantage over a comparable battery-powered DC motor actuated system in a system-level comparison of actuation performance. As such, liquid-propellant-based pneumatic actuation is a highly competitive approach that can potentially lead to a practical transtibial prosthesis with long duration of the operation. Compared with the traditional electromechanical actuation, the liquid-propellant-based pneumatic actuation does come with a few weaknesses, including: (1) the system configuration is more complex with more moving parts; (2) the noise level is higher; and (3) the system dynamics are highly nonlinear, which makes the motion control more challenging. However, in the authors' opinion, the gain in actuation performance outweighs these weaknesses, and pneumatic actuation can still be viable as a competitive actuation approach for future transtibial prostheses.

4.3 PROSTHESIS CONTROL

With the capability of supplying a significant amount of torque on the prosthetic ankle joint, this powered transtibial prosthesis requires a reliable and effective control approach to

enable the natural and coordinated interaction with the user. To enable such interaction, the general impedance control framework is adopted for the development of the prosthesis controller in this work. The general impedance control theory was proposed by Hogan in 1980s for the control of robotic manipulators in the interactive tasks [23]. This control approach is especially useful in the robotic applications that involve interaction with human, considering the important role of impedance modulation in the human motion control [24,25]. The application of impedance control in lower-extremity prosthesis control is proposed by Sup *et al.*, and its effectiveness has been demonstrated in the control of powered transfemoral prostheses with active knee and ankle joints [10].

For the application of impedance control in transtibial prostheses, there are two key steps in the process, including the proper segmentation of a walking cycle into a finite number of states (or phases), followed by the representation of the ankle biomechanical behavior with proper impedance parameters within each state. Note that this general method was used in the design of electric motor-actuated prostheses and guided the selection of spring elements [5,6]. Using this method for the controller design, the constraints associated with physical springs no longer apply, resulting in more flexibility in the selection of impedance parameters.

4.3.1 ANKLE BIOMECHANICS IN WALKING

The impedance control approach in this work aims to simulate the biomechanical behavior of the ankle in human walking, which has been the topic of a large amount of studies. As the basis of the analysis, the ankle angle-torque trajectory of slow walking is plotted in Fig. 4-5 (a), utilizing the data in [2]. With the large variation in the shape of the curve, it can be clearly seen that it is impossible to describe the entire cycle with a single impedance representation,

highlighting the importance of segmentation. The segmentation of the torque curve can be conducted with a few well-defined transition points (labeled as A~D in Fig. 4-5 (a)), with which the gait cycle is divided into four distinct stages. The following is a brief summary of these events and phases:

Event A: Heel Strike: the heel touches the ground, marking the start of the gait cycle.

Phase #1 (A→B): Early Stance (ES). In this state, the foot plantarflexes until it lays flat on the ground, and the ankle provides a small resistive torque that increases with the joint rotation.

Event B: Foot Flat: the foot starts to lie completely flat on the ground.

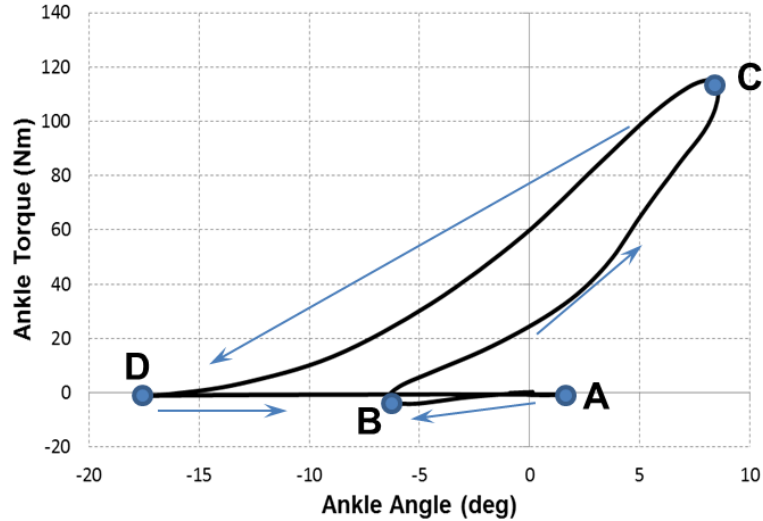
Phase #2 (B→C): Middle Stance (MS). In this state, the foot stays flat on the ground while the shank moves forward (dorsiflexion), and the ankle provides a rapidly increasing torque.

Event C: Maximum Dorsiflexion: the joint angle reaches the maximum value.

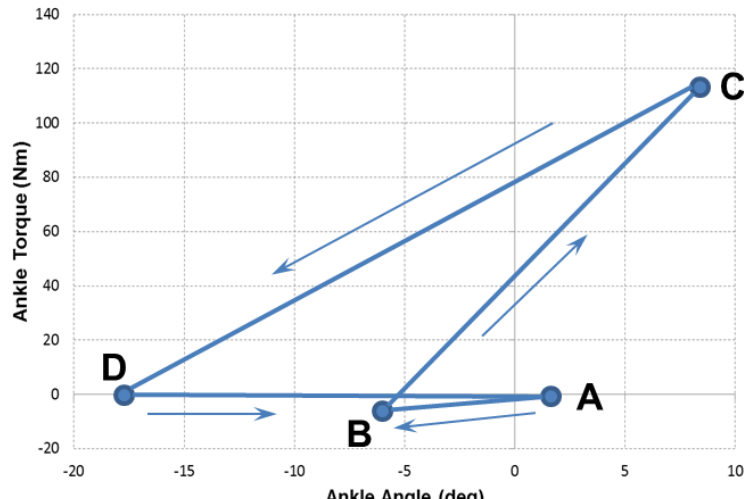
Phase #3 (C→D): Late Stance (LS). In this state, the foot pushes the ground and propels the body forward, with a torque that decreases with the plantarflexion of the ankle.

Event D: Toe Off: the toe leaves the ground.

Phase #4 (D→A): Swing (SW). In this state, the foot is completely in the air without contact to the ground, and the ankle experiences fast dorsiflexion with low torque, creating sufficient ground clearance and getting ready for the heel strike of the next cycle.



(a)



(b)

Figure 4-5: Analysis of the ankle dynamic behavior in walking: (a) Segmentation of the original torque trajectory, (b) Simple impedance representation to understand the dynamic behavior within each phase.

4.3.2 IMPEDANCE MODELING

In general, the impedance applied to a robotic joint can be modeled as the resistance associated with a set of virtual springs and dampers. For a virtual spring, the corresponding

torque is a function of the joint position; while for a virtual damper, the corresponding torque is a function of the joint velocity. The equation for the impedance torque is

$$\tau = \sum_{i=1}^n K_i (\theta - \theta_0)^{2i-1} + \sum_{j=1}^m B_j (\dot{\theta})^{2j-1} \quad (4.6)$$

where K_i 's and B_j 's are the stiffness and damping coefficients, respectively, and θ_0 is the equilibrium position of the virtual spring. Note that this equation includes the higher order terms for the general nonlinear spring and damper behaviors. Mathematically, it is possible to match a torque curve with infinite sets of parameters. However, to develop a practical prosthesis controller, its dynamic behavior should closely match the biomechanical behavior of the ankle with minimum complexity. To obtain a good understanding of such behavior, the original segmented torque curve (as shown in Fig. 4-5 (a)) is fitted with simple linear-spring torque curve within each state, as shown in Fig. 4-5 (b). The impedance behavior within each phase is summarized below:

Phase #1 (Early Stance): The ankle functions like a spring with moderate stiffness (~1 Nm/deg) to provide shock absorption and appropriate plantarflexion resistance before foot flat.

Phase #2 (Middle Stance): The ankle functions like a very stiff spring (~8 Nm/deg) to absorb energy to get ready for the following push-off. Better matching to the nonlinear behavior can be obtained by adding higher order terms in the spring torque equation.

Phase #3 (Late Stance): The ankle functions like a stiff spring, with the stiffness lower than that in Phase #2 (~5 Nm/deg). However, with an equilibrium position significantly less than that in the Phase #2 (~-16°), the ankle in this state generates higher torque output than in Phase #2, constituting the powered push-off in walking. As in Phase #2, better

matching to the nonlinear behavior can be obtained by adding higher order terms in the spring torque equation.

Phase #4 (Swing): The ankle functions like a spring with very low stiffness, returning the ankle to a slightly dorsiflexed position ($\sim 2^\circ$) to get ready for the next heel strike.

Based on the impedance behavior summarized above, the actual control algorithm implemented for the prosthesis control takes the following form:

$$\tau = K(\theta - \theta_0) + B\dot{\theta} \quad (4.7)$$

where, a linear stiffness term (K is the linear stiffness coefficient) plays the primary role in the prosthesis control, and a damping term (B is the linear damping coefficient) is added to dampen the motion and improve the stability of the motion. The corresponding parameter values in each state are obtained through repeated tuning in actual walking experiments which will be described in section 4.4.

4.3.3 CONTROLLER IMPLEMENTATION

Note that an important component of the finite-state machine is the switching conditions, which are usually associated with specific events in the walking gait (e.g., heel strike). A common approach to detect such events is through contact sensors, such as foot switch or force-sensing resistors under the foot. However, such sensors tend to unreliable and susceptible to failure. As such, the switching conditions in this work are constructed based solely on the ankle angle signal (θ) and its derivative ($\dot{\theta}$), as shown in Fig. 4-6. Specifically, the heel strike is detected according to the onset of plantarflexion ($\dot{\theta} < 0$). To avoid the false switching to Phase #3 (Late Stance), an additional condition ($\theta < \Theta_1$) is imposed, in which Θ_1 is a threshold value of approximately $2\text{--}3^\circ$. The foot flat is detected according to the onset of dorsiflexion ($\dot{\theta} > 0$). The

maximum dorsiflexion is detected when the ankle angle exceeds the second threshold value Θ_2 , with the specific value at approximately $7\text{--}8^\circ$. The toe off is detected when the ankle angle decreases below the third threshold value Θ_3 , with the specific value at approximately -16° . With these switching conditions, the controller can be implemented reliably on the prosthesis in the repeated walking experiments.

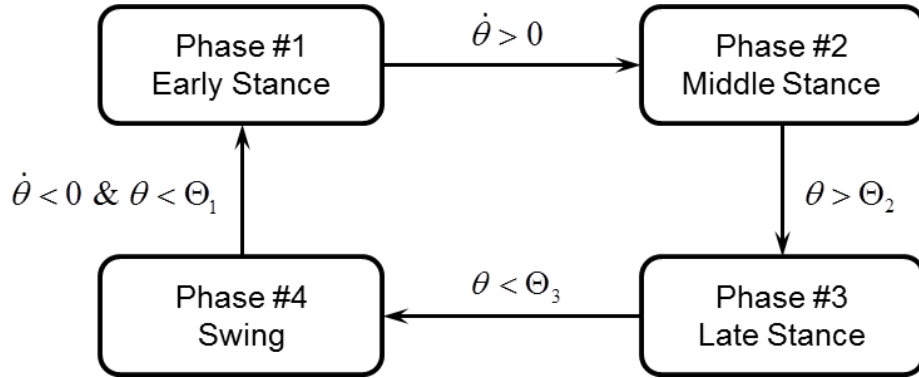


Figure 4-6: Finite-state machine for the implementation of the prosthesis controller.

The state machine (Fig. 4-6) combined with the impedance-based joint behavior representation (Eq. (4.7)) generates the desired actuation torque command for the powered ankle joint. To obtain this desired actuation torque, the torque command is converted to the desired actuation force with the following equation

$$F_d = \tau_d \left(\frac{\sqrt{a^2 + b^2 - 2ab\cos\phi}}{abs\sin\phi} \right) \quad (4.8)$$

The desired force as calculated by Eq. (4.8) is compared with the measured actuation force F to generate the error signal $e = F_d - F$. Based on this error signal, the standard PID control is applied to obtain the valve command for the real-time implementation of the controller. The

control gains were tuned in the experiments to generate a quick response without jeopardizing the stability in operation.

4.4 PROSTHESIS TESTING

After the fabrication of the prosthesis prototype and the development of the prosthesis controller, treadmill walking experiments have been conducted to evaluate the prosthesis' performance in restoring an amputee user's locomotion functions. The experimental protocol is approved by the Institutional Review Board of the University of Alabama. One unilateral transtibial amputee participated in the study. The male participant was 22 years old, 175 cm in height, and weighed 56.7 kg. An extension pylon was used to fit the prosthesis to the subject. The pylon also served as the base for mounting the control valve in the experiments, such that the delay due to the connection tube could be minimized. Figure 4-7 shows the subject's lower limb when fitted with the prosthesis.

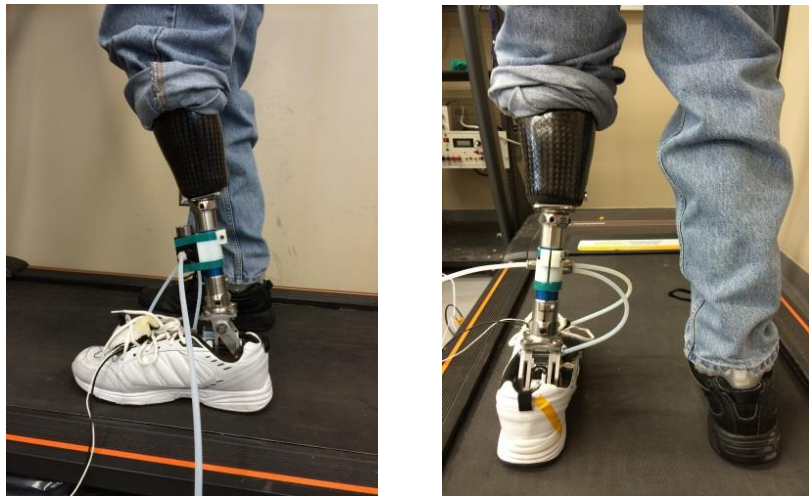


Figure 4-7: The test subject fitted with the transtibial prosthesis.

In the walking experiments, repeated tuning was conducted to obtain a satisfactory performance. In the tuning, the trajectory of the prosthetic joint was compared with the standard joint trajectory in the biomechanical literature (such as [2]) to form an objective evaluation of the gait quality. Additionally, visual observation and the feedback from the test subject also played important roles for the adjustment of control parameters. The control parameters obtained from the tuning are summarized in Table 4-2. In the experiments, impedance values obtained from the physiological analysis (section 4.3.2) were used as the initial control parameters, and these parameters were modified according to the measured joint angle/torque trajectories and the subject's feedback. It is worth mentioning that, for the stiffness value in MS phase, the physiological analysis indicated a much higher value of 8 Nm/deg, representing a very stiff spring. The control parameter, however, was reduced to its current value (4 Nm/deg) after repeated tuning. The reason for this discrepancy, in our opinion, could be the subject's experience with his daily-use prosthesis, i.e., the subject has gotten used to the less stiff passive prosthesis, and thus his gait was different from the standard gait of healthy individuals. Although the stiffness and damping values are the same for MS and LS phases, the equilibrium point for LS phase (-25°) is much lower than that for MS phase (-3°), generating a much higher torque for the push-off behavior in the LS phase.

The performance of the prosthesis and its controller are shown in Figs. 4-8–4-10. Fig. 4-8 displays a comparison between the angular trajectories of the prosthetic joint versus the biological joint, utilizing the standard biomechanical data in [2]. As shown in the figure, the prosthetic joint trajectory is smooth and close to the standard joint trajectory in the majority of the gait cycle. The prosthetic joint trajectory displays a more obvious transition between adjacent phases, presumably because of the use of the finite-state impedance controller. Fig. 4-9 displays

a comparison between the actuation torque of the prosthetic joint and the measured torque in the biological joint in level walking. Again, the actuation torque curve resembles the biological joint torque curve, but displays more obvious transitions due to the use of the finite-state controller. Last but not least, Fig. 4-10 shows the power output within a gait cycle. As shown in this figure, the actuated ankle joint is able to generate over 120 W peak power during the powered push-off, which is fundamentally different from the passive behavior of a traditional non-powered transtibial prosthesis. As such, a prosthesis user can leverage this active energetic behavior and enjoy a more natural and comfortable walking. This has been confirmed by the feedback of the test subject in the experiments.

Table 4-2: Parameters of the prosthesis controller.

State	K (Nm/deg)	B (Nm-s/deg)	θ_0 (deg)
ES	0.9	0.1	1
MS	4	0.1	-3
LS	4	0.1	-25
SW	0.9	0.01	1

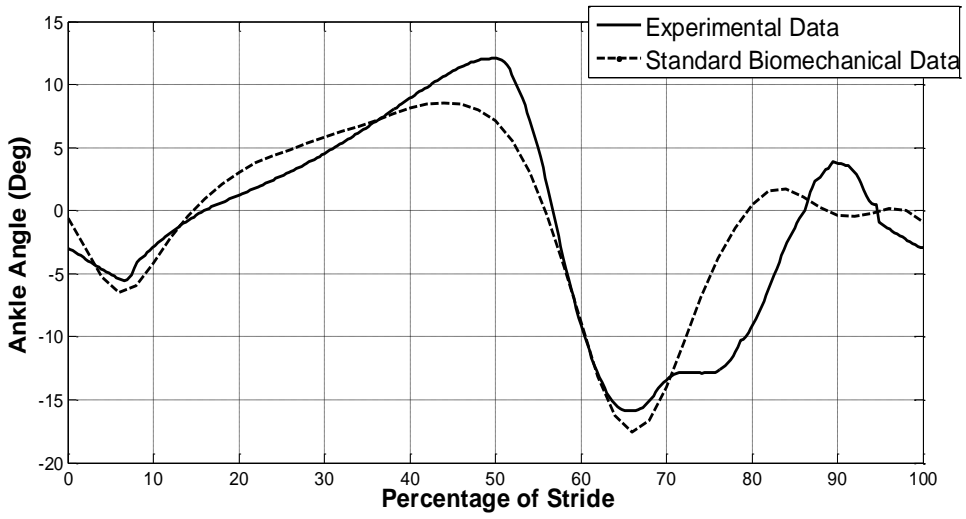


Figure 4-8: Comparison of the trajectory of the prosthetic ankle joint versus the standard ankle trajectory of healthy subjects in level walking (data from [2]).

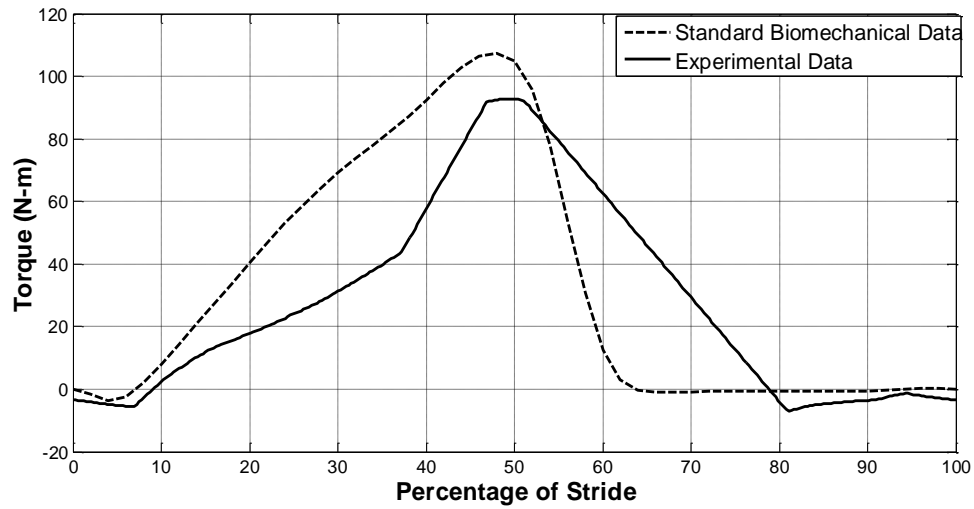


Figure 4-9: Comparison of the torque trajectory of the prosthetic ankle joint versus the standard ankle torque trajectory of healthy subjects in level walking (data from [2]).

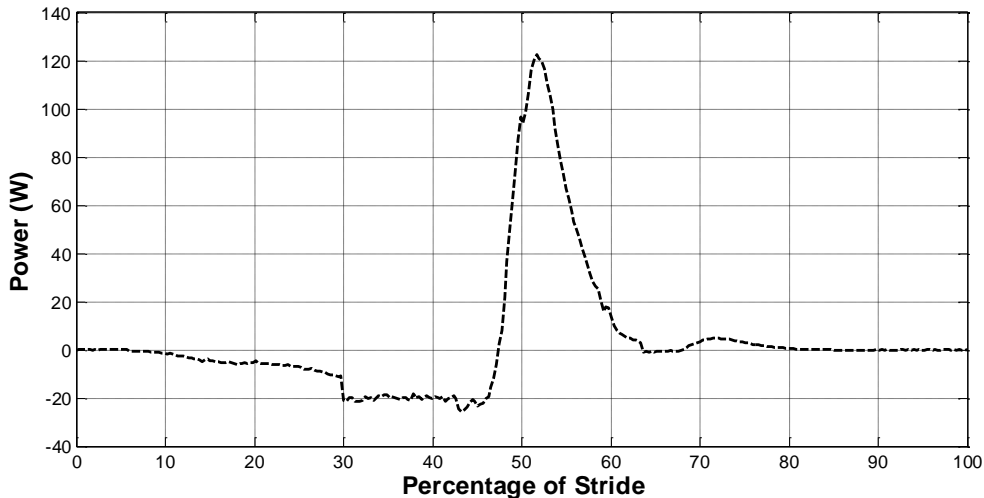


Figure 4-10: Power output of the actuated ankle joint.

4.5 CONCLUSIONS

In this chapter, a unique robotic transtibial prosthesis that utilizes a pneumatic cylinder-type actuator to drive the prosthetic ankle joint is presented. To reduce the prosthesis height, the pneumatic cylinder is arranged horizontally and drives the ankle joint through an inverted crank-slider mechanism. In the design process, the parameters were determined to provide the desired torque capacity while reducing the weight and volume of the system. The resulted prosthesis design is able to supply sufficient actuation torque for level walking within the majority of the range of motion. For the walking control of the prosthesis, a finite-state impedance controller has been developed based on the analysis of the biomechanical behavior of the biological ankle joint in walking. The angle-torque curve was segmented into a number of individual phases, and within each phase, the joint behavior is represented with a simple impedance behavior. For the implantation in the prosthesis control, the parameters were tuned in the treadmill walking experiments. After repeated tuning, the prosthesis was able to provide an improved gait

compared with the traditional passive prosthesis, according to the data collected in the experiments and the feedback provided by the test subject.

4.6 ACKNOWLEDGMENT

The authors gratefully acknowledge the support of the National Institutes of Health under Grant No. 5R01HD075493 and the National Science Foundation under Grant No. 1351520.

REFERENCES

- [1] Winter, D. A. (1983). Energy generation and absorption at the ankle and knee during fast, natural, and slow cadences. *Clinical orthopaedics and related research*, 175, 147-154.
- [2] Winter, D. A. (1991). *Biomechanics and motor control of human gait: normal, elderly and pathological*.
- [3] Hsu, M. J., Nielsen, D. H., Lin-Chan, S. J., & Shurr, D. (2006). The effects of prosthetic foot design on physiologic measurements, self-selected walking velocity, and physical activity in people with transtibial amputation. *Archives of physical medicine and rehabilitation*, 87(1), 123-129.
- [4] Torburn, L., Powers, C. M., Guitierrez, R., & Perry, J. (1995). Energy expenditure during ambulation in dysvascular and traumatic below-knee amputees: a comparison of five prosthetic feet. *Journal of rehabilitation research and development*, 32(2), 111.
- [5] Au, S. K., Weber, J., & Herr, H. (2007, June). Biomechanical design of a powered ankle-foot prosthesis. In *Rehabilitation Robotics, 2007. ICORR 2007. IEEE 10th International Conference on* (pp. 298-303). IEEE.
- [6] Au, S. K., Weber, J., & Herr, H. (2009). Powered Ankle--Foot Prosthesis Improves Walking Metabolic Economy. *IEEE Transactions on Robotics*, 25(1), 51-66.
- [7] Herr, H. M., & Grabowski, A. M. (2012, February). Bionic ankle-foot prosthesis normalizes walking gait for persons with leg amputation. In *Proc. R. Soc. B* (Vol. 279, No. 1728, pp. 457-464). The Royal Society.
- [8] Hitt, J. K., Bellman, R., Holgate, M., Sugar, T. G., & Hollander, K. W. (2007, January). The sparky (spring ankle with regenerative kinetics) project: Design and analysis of a robotic transtibial prosthesis with regenerative kinetics. In *ASME 2007 International Design Engineering Technical Conferences and Computers and Information in Engineering Conference* (pp. 1587-1596). American Society of Mechanical Engineers.
- [9] Hitt, J. K., Sugar, T. G., Holgate, M., & Bellman, R. (2010). An active foot-ankle prosthesis with biomechanical energy regeneration. *Journal of medical devices*, 4(1), 011003.
- [10] Sup, F., Varol, H. A., Mitchell, J., Withrow, T. J., & Goldfarb, M. (2009). Preliminary evaluations of a self-contained anthropomorphic transfemoral prosthesis. *IEEE/ASME Transactions on Mechatronics*, 14(6), 667-676.

- [11] Sup, F., Varol, H. A., & Goldfarb, M. (2011). Upslope walking with a powered knee and ankle prosthesis: initial results with an amputee subject. *IEEE Transactions on Neural Systems and Rehabilitation Engineering*, 19(1), 71-78.
- [12] Lawson, B. E., Varol, H. A., Huff, A., Erdemir, E., & Goldfarb, M. (2013). Control of stair ascent and descent with a powered transfemoral prosthesis. *IEEE Transactions on Neural Systems and Rehabilitation Engineering*, 21(3), 466-473.
- [13] Kuribayashi, K. (1992). Criteria for the evaluation of new actuators as energy converters. *Advanced Robotics*, 7(4), 289-307.
- [14] Sup, F., Bohara, A., & Goldfarb, M. (2008). Design and control of a powered transfemoral prosthesis. *The International journal of robotics research*, 27(2), 263-273.
- [15] Versluys, R., Desomer, A., Lenaerts, G., Van Damme, M., Beyl, P., Van der Perre, G., ... & Lefebvre, D. (2008, October). A pneumatically powered below-knee prosthesis: Design specifications and first experiments with an amputee. In *Biomedical Robotics and Biomechatronics, 2008. BioRob 2008. 2nd IEEE RAS & EMBS International Conference on* (pp. 372-377). IEEE.
- [16] Versluys, R., Van Ham, R., Vanderniepen, I., & Lefebvre, D. (2009, June). Successful walking with a biologically-inspired below-knee prosthesis. In *Rehabilitation Robotics, 2009. ICORR 2009. IEEE International Conference on* (pp. 652-657). IEEE.
- [17] Seymour, R. (2002). *Prosthetics and orthotics: lower limb and spinal*. Lippincott Williams & Wilkins.
- [18] Winter, D. A. (2009). *Biomechanics and motor control of human movement*. John Wiley & Sons.
- [19] Riener, R., Rabuffetti, M., & Frigo, C. (2002). Stair ascent and descent at different inclinations. *Gait & Posture*, 15(1), 32-44.
- [20] McIntosh, A. S., Beatty, K. T., Dwan, L. N., & Vickers, D. R. (2006). Gait dynamics on an inclined walkway. *Journal of Biomechanics*, 39(13), 2491-2502.
- [21] Beater P. *Pneumatic Drives: System Design, Modelling and Control*, Springer-Verlag Berlin Heidelberg, New York, USA, 2007.
- [22] Goldfarb, M., Barth, E. J., Gogola, M. A., & Wehrmeyer, J. A. (2003). Design and energetic characterization of a liquid-propellant-powered actuator for self-powered robots. *IEEE/ASME transactions on mechatronics*, 8(2), 254-262.

- [23] Hogan, N. (1985). Impedance control: an approach to manipulation: Part 1-theory, Part 2-implementation, and Part 3-applications. *ASME Journal of Dynamic Systems, Measurement, and Control*, vol.107, pp. 1-24.
- [24] Hogan, N. (1984). Adaptive control of mechanical impedance by coactivation of antagonist muscles. *IEEE Transactions on Automatic Control*, 29(8), 681-690.
- [25] Hogan, N. (1985). The mechanics of multi-joint posture and movement control. *Biological Cybernetics*, 52(5), 315-331.

CHAPTER 5: PNEUMATIC VARIABLE SERIES ELASTIC ACTUATOR

Inspired by human motor control theory, stiffness control is highly effective in manipulation and human-interactive tasks. The implementation of stiffness control in robotic systems, however, has largely been limited to close-loop control, and suffers from multiple related issues such as limited frequency range, potential stability issue, and lack of contribution to energy efficiency. Variable-stiffness actuator represents a better solution, but the current designs are complex, heavy, and bulky. The approach presented in this chapter seeks to address these issues by using pneumatic actuator as a variable series elasticity actuator, leveraging the compressibility of the working fluid. In this chapter, a pneumatic actuator is modeled as an elastic element with controllable stiffness and equilibrium point, both of which are functions of air masses in the two chambers. As such, for the implementation of stiffness control in a robotic system, the desired stiffness/equilibrium point can be converted to the desired chamber air masses, and a predictive pressure control approach is developed to control the timing of valve switching to obtain the desired air mass while minimizing control action. Experimental results showed that the new approach in this paper requires less expensive hardware (on-off valve instead of proportional valve), causes less control action in implementation, and provides good control performance by leveraging the inherent dynamics of the actuator.

5.1 INTRODUCTION

Stiffness control, proposed by Salisbury in 1980's, is a highly effective control approach for robotic manipulators in their interaction with humans or the environment [1]. Unlike position control and force/torque control, stiffness control essentially regulates the behavior of the robotic manipulator to follow the desired behavior of an artificial spring. Similar to a physically existing mechanical spring, an artificial spring generates an output force when there is a deflection from the equilibrium position. Later this approach was generalized by Hogan to formulate the concept of impedance control, in which an artificial damper was added [2].

A major reason for stiffness/impedance control's popularity in modern robotics is its close match to the biological motor control theory. From a dynamics perspective, a biological muscle functions as a source of controllable force and impedance. The widely-accepted equilibrium position hypothesis presented by Feldman and Lewis [3] supports this observation via physiological evidence. According to the theory, with an agonist-antagonist musculoskeletal structure, a pair of muscles provides both independent position and stiffness control. The stiffness of the joint is determined via the sum of muscle activations, while the output torque and subsequent output position are determined by the difference in muscles activations. Prior research presented by Hogan [4-6] has shown that such a capability is critical in providing stability in the humans' interaction with the environment. Research has also shown that variable stiffness is a major contributing factor for the high energy efficiency in mammalian locomotion [7,8]. Inspired by such findings, stiffness/impedance control has been used in a wide variety of robotic applications. For example, impedance control has been used in conjunction with a finite-state machine to obtain a highly effective walking controller for a lower-limb prosthesis [9].

For the implementation of stiffness control, current approaches have largely been limited to the traditional close-loop control. Specifically, the desired force is calculated according to the deviation from the equilibrium point in combination with the desired stiffness, and close-loop force control is used to regulate the actuator output to obtain the desired actuation force. Such strategy is conceptually simple, and the implementation does not rely on the specific type of actuator. On the other hand, this strategy also suffers from the common problems associated with close-loop control, especially the limited frequency range and potential stability issue due to the time delay in the control loop. Furthermore, the close-loop strategy does not contribute to the energy efficiency of the robotic system, since close-loop control is energetically non-conservative in general.

Motivated by these issues, researchers have also attempted to develop actuators with physically existing stiffness. Series Elastic Actuator (SEA) is a typical example [10-12]. Connecting elastic elements in series with the electric motor-transmission assembly, a SEA incorporates the desired elasticity. However, the package is bulky and complex due to the added components. Furthermore, the elasticity of the SEA is usually fixed, without the capability of adjusting the stiffness in use. Under similar strategies, actuators with variable stiffness have also been developed, most of which based on nonlinear springs in combination with two independently controlled motors. Among them, some use the agonist-antagonist configuration, inspired by the human musculoskeletal structure (e.g., Refs. [13-17]); others use a configuration with each motor dedicated to a certain function (generating force/torque output or regulating output stiffness) (e.g., Refs. [18] and [19]). Obviously, these actuator designs also suffer from similar problems as the SEA, e.g., added complexity and excessive weight/size.

Unlike these existing approaches, the variable-stiffness actuator presented in this chapter does not rely on dedicated elastic components. Instead, a double-acting pneumatic actuator, with two pressure-controlled chambers, can function as a variable-stiffness actuator with much less complexity compared with the aforementioned motor-spring designs. Note that there have been works on the simultaneous stiffness and position/force control for pneumatic muscle-type and cylinder-type actuators [20-23]. However, these works do not explicitly address the regulation of the equilibrium point, affecting their efficacy in use. In the subsequent section, the modeling of the pneumatic actuator as a variable series elastic actuator (VSEA) is presented, followed by the control and experimental demonstration of the proposed approach.

5.2 PNEUMATIC ACTUATOR AS A VSEA

With the compressible working fluid, a pneumatic actuator features a physically existing elasticity, which enables its use as a series elastic actuator (SEA), similar in concept to the aforementioned SEA actuator. Furthermore, for a double-acting cylinder-type actuator, two actuator chambers can be independently controlled with respect to its air pressure as shown in Fig. 5-1. As a result, this actuator can be treated as a two-input-two-output dynamic system, which provides the basis for its use as a VSEA. In this section, elastic behavior of a pneumatic actuator is modeled to formulate the two-input-two-output mapping for the implementation of stiffness control.

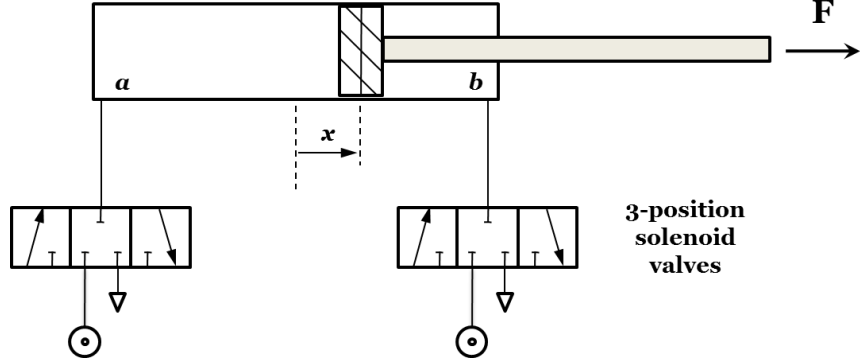


Figure 5-1: Double-acting pneumatic cylinder with two independently controlled chambers.

To derive the equation for actuator stiffness, we can start from the equation of actuator force:

$$F = P_a A_a - P_b A_b - P_{atm} A_r \quad (5.1)$$

where P_a is the Chamber a (rodless chamber) pressure, A_a is the piston area facing Chamber a , P_b is the Chamber b pressure, A_b is the piston area facing Chamber b , P_{atm} is the atmospheric pressure, and A_r is the rod cross-sectional area. The actuator stiffness is defined as the partial derivative of the actuator force with respect to displacement:

$$K = -\frac{\partial F}{\partial x} = -A_a \frac{\partial P_a}{\partial x} + A_b \frac{\partial P_b}{\partial x} \quad (5.2)$$

where K is the actuator stiffness, and x is the displacement with respect to the middle point of the stroke as the reference. Assuming air is an ideal gas, chamber pressure can be expressed as:

$$P_a = \frac{m_a RT}{V_a} = \frac{m_a RT}{A_a (\frac{L}{2} + x) + V_{da}} \quad (5.3)$$

$$P_b = \frac{m_b RT}{V_b} = \frac{m_b RT}{A_b (\frac{L}{2} - x) + V_{db}} \quad (5.4)$$

where R is the universal gas constant, T is the air temperature, V_a and V_b are the total volumes in Chamber a and Chamber b , respectively, m_a and m_b are the air masses in Chamber a and Chamber b , respectively, L is the cylinder stroke, and V_{da} and V_{db} are the dead volumes in Chamber a and Chamber b , respectively. The dead volumes are the volumes unaffected by the motion of the piston, e.g., volume in the air pathway in the actuator, internal volume of the connection tube, etc. They are included to improve the accuracy of the dynamic model. To facilitate the subsequent derivation, a new variable, namely dead length, can be introduced as the ratio of the dead volume versus the corresponding piston area:

$$L_{da} = \frac{V_{da}}{A_a} \quad (5.5)$$

$$L_{db} = \frac{V_{db}}{A_b} \quad (5.6)$$

Substituting Eqs. (5.5) and (5.6) into (5.3) and (5.4) yields:

$$P_a = \frac{m_a RT}{A_a (\frac{L}{2} + L_{da} + x)} \quad (5.7)$$

$$P_a = \frac{m_a RT}{A_a (\frac{L}{2} + L_{da} + x)} \quad (5.8)$$

Differentiating Eqs. (5.7) and (5.8) with respect to x yields:

$$\frac{\partial P_a}{\partial x} = -\frac{m_a RT}{A_a (\frac{L}{2} + L_{da} + x)^2} \quad (5.9)$$

$$\frac{\partial P_b}{\partial x} = \frac{m_b RT}{A_b (\frac{L}{2} + L_{db} - x)^2} \quad (5.10)$$

Substituting Eqs. (5.9) and (5.10) into (5.2),

$$K = \frac{m_a RT}{\left(\frac{L}{2} + L_{da} + x\right)^2} + \frac{m_b RT}{\left(\frac{L}{2} + L_{db} - x\right)^2} \quad (5.11)$$

As can be clearly seen from this equation, the actuator stiffness K is a function of the chamber air masses m_a and m_b as well as the piston displacement x . When the chambers are closed, the air masses remain as constants, and thus the stiffness is nearly a constant when the displacement is small. Note that the stiffness still varies with the displacement, which requires special attention when the displacement is significant. Similar to the derivation above, the equilibrium position x_e can also be expressed as a function of m_a and m_b . At equilibrium, there is no force output:

$$F_e = P_{ae}A_a - P_{be}A_b - P_{atm}A_r = 0 \quad (5.12)$$

where P_{ae} and P_{be} are the chamber pressures when the piston is at the equilibrium point. Again, these chamber pressures can be expressed as functions of chamber air masses by assuming the air to be an ideal gas:

$$P_{ae} = \frac{m_a RT}{A_a \left(\frac{L}{2} + L_{da} + x_e\right)} \quad (5.13)$$

$$P_{be} = \frac{m_b RT}{A_b \left(\frac{L}{2} + L_{db} - x_e\right)} \quad (5.14)$$

Substituting Eqs. (5.13) and (5.14) into (5.12) yields:

$$\frac{m_a RT}{\frac{L}{2} + L_{da} + x_e} - \frac{m_b RT}{\frac{L}{2} + L_{db} - x_e} - P_{atm}A_r = 0 \quad (5.15)$$

This equation can serve as an implicit definition of the equilibrium point x_e as a function of m_a and m_b . As such, Eqns. (5.11) and (5.15) constitute a dynamic model from the chamber air masses as the input to the stiffness/equilibrium point as the output. Conversely, for the implementation of stiffness control, the desired chamber air masses can be calculated from the

desired stiffness/equilibrium point. This can be conducted by solving the following matrix equation, which is derived by manipulating and combining (5.11) and (5.15):

$$[\mathbf{A}] \begin{Bmatrix} m_a \\ m_b \end{Bmatrix} = \{\mathbf{B}\} \quad (5.16)$$

where

$$[\mathbf{A}] = \begin{bmatrix} \frac{RT}{(\frac{L}{2} + L_{da} + x)^2} & \frac{RT}{(\frac{L}{2} + L_{db} - x)^2} \\ \frac{RT}{\frac{L}{2} + L_{da} + x_e} & -\frac{RT}{\frac{L}{2} + L_{db} - x_e} \end{bmatrix} \quad (5.17)$$

$$\{\mathbf{B}\} = \begin{Bmatrix} K \\ P_{atm} A_r \end{Bmatrix} \quad (5.18)$$

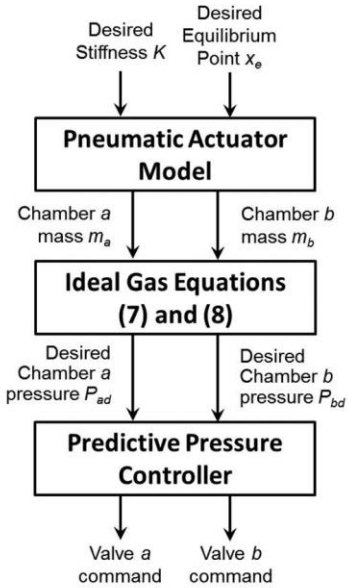
The result can be expressed as

$$\begin{Bmatrix} m_a \\ m_b \end{Bmatrix} = [\mathbf{A}]^{-1} \{\mathbf{B}\} \quad (5.19)$$

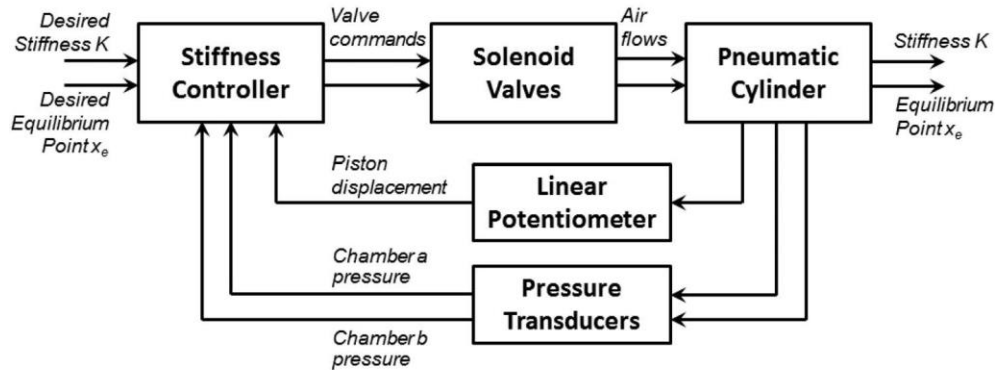
5.3 STIFFNESS CONTROL OF PNEUMATIC ACTUATOR

The model derived in the previous section forms the foundation for the stiffness control using the pneumatic actuator as a VSEA. Desired chamber air masses, as calculated through Eq. (5.19), serve as the set point for the lower-level controller. Air masses, however, cannot be directly measured, and thus need to be converted to the chamber pressures according to Eqns. (5.7) and (5.8), based on the current position. Subsequently, the desired chamber pressures can be obtained through simple pressure control. The whole process is depicted in Fig. 5-2 (a), and the entire dynamic system is depicted in Fig. 5-2 (b).

A major advantage of the approach presented in this work is its potential in minimizing control actions in the stiffness control process. When a set of stiffness/equilibrium point is implemented, the corresponding chamber masses remain constant, assuming small deviation from the equilibrium point (i.e., $x \approx x_e$). As such, a simple 3-position, closed-center valve can be used for each chamber, and only one cycle of valve action (open to supply or exhaust, and then return to the closed position at the center) is needed to increase or decrease chamber air mass to the desired value, which is unaffected by the subsequent piston motion. This approach offers multiple advantages over the traditional close-loop implementation of stiffness control, including significantly reduced control action, noise level, and energy consumption.



(a)



(b)

Figure 5-2: Stiffness control of a pneumatic actuator: (a) Controller structure and (b) system diagram.

To realize the aforementioned one-cycle valve action, however, poses a challenge to the controller design. On-off valves usually have a significant time delay between signal input and the corresponding spool movement. Such time delay, if not properly addressed, will cause severe overshoot and large control error. To address this problem, a pressure prediction approach is developed to control the timing of valve closing action. When a new set of stiffness/equilibrium

point commands arrive, the desired air mass in a chamber is compared to the current air mass to determine the initial control action (connecting to the supply to increase the air mass, or connecting to the exhaust to decrease). In the meantime, a pressure prediction algorithm is used to predict the future air pressure in a switching cycle (i.e., the time for the valve to switch to the closed position after the valve control signal is received). If the predicted pressure reaches the desired pressure, the valve will be switched to the center closed position to complete the cycle. The flow chart for this process is shown in Fig. 5-3, and the details of the pressure prediction algorithm are described below.

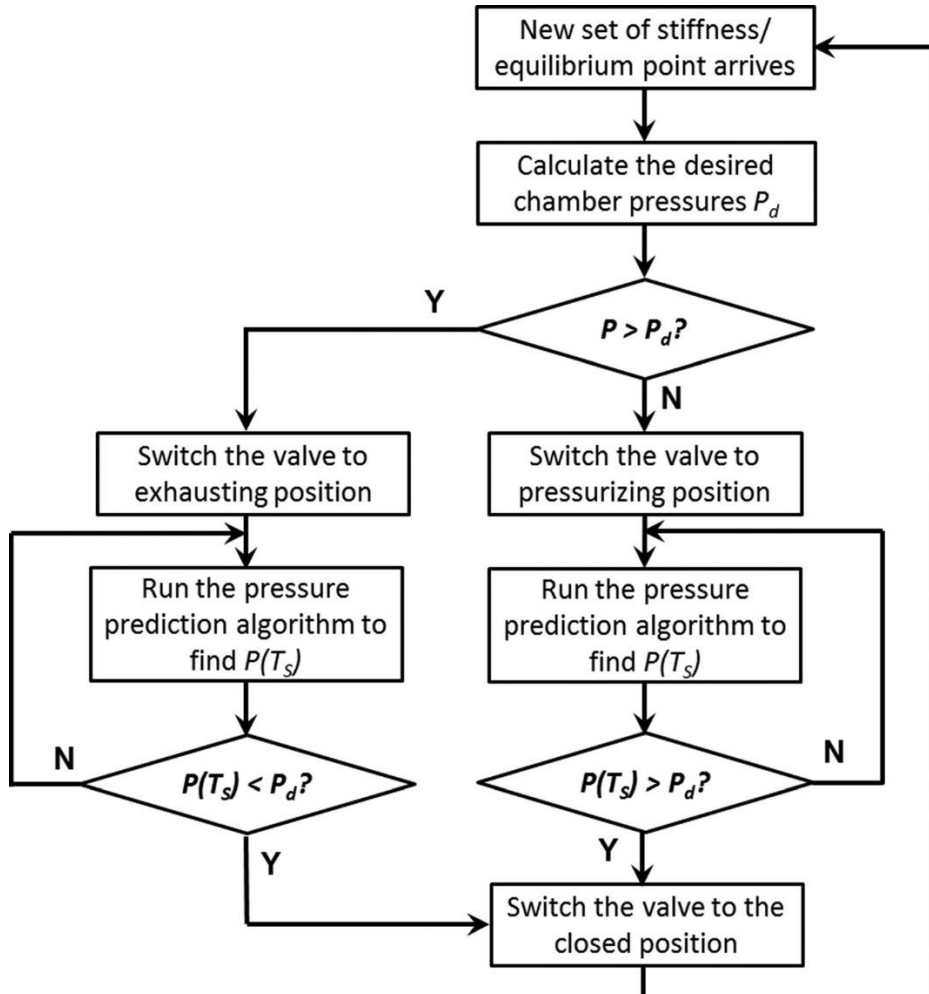


Figure 5-3: The predictive pressure controller.

For each actuator chamber, the pressure dynamics can be expressed by

$$\dot{P} = \frac{RT}{V} \dot{m} - \frac{P}{V} \dot{V} \quad (5.20)$$

where V is the chamber volume, and \dot{m} is the mass flow rate. Pressure change usually occurs much faster than piston motion. As such, the velocity of piston movement can be assumed to be a constant, and the average chamber volume over the valve switch period and the rate of change of the chamber volume can be calculated accordingly. To calculate the mass flow rate, the flow through the valve can be modeled as the flow of an ideal gas through a converging nozzle, which yields the following equation:

$$\dot{m}(P_u, P_d) = \pm A_v \Psi(P_u, P_d) \quad (5.21)$$

and

$$\Psi(P_u, P_d) = \begin{cases} \sqrt{\frac{\gamma}{RT}} \left(\frac{2}{\gamma+1} \right)^{(\gamma+1)/(\gamma-1)} C_f P_u & \text{if } \frac{P_d}{P_u} \leq C_r \text{ (choked)} \\ \sqrt{\frac{2\gamma}{RT(\gamma-1)}} \sqrt{1 - \left(\frac{P_d}{P_u} \right)^{(\gamma-1)/\gamma}} \left(\frac{P_d}{P_u} \right)^{1/\gamma} C_f P_u & \text{otherwise (un choked)} \end{cases} \quad (5.22)$$

where A_v is the valve opening area, P_u and P_d are the upstream and downstream pressures, respectively, γ is the ratio of specific heats, C_f is the discharge coefficient of the valve (which accounts for irreversible flow conditions), and C_r is the pressure ratio that divides the flow regimes into unchoked (sub-sonic) and choked (sonic) flow through the orifice. To simplify the analysis, the valve opening area can be treated as a constant over the switching period. According to Eqns. (5.21) and (5.22), the mass flow rate can be expressed as a function of the

chamber pressure. The specific form of the equation depends on the flow direction (charging/exhausting) and the flow regime (choked/unchoked), with four possible scenarios:

I) Charging in the choked regime ($\frac{P}{P_s} \leq C_r$, P_s is the supply pressure), which generates a

constant flow rate:

$$\dot{m}_1 = A_v \sqrt{\frac{\gamma}{RT}} \left(\frac{2}{\gamma+1} \right)^{(\gamma+1)/(\gamma-1)} C_f P_s = C_1 P_s \quad (5.23)$$

where the constant C_1 is introduced to simplify the expression.

II) Charging in the unchoked regime ($\frac{P}{P_s} > C_r$), which yields the following function:

$$\dot{m}_2 = A_v \sqrt{\frac{2\gamma}{RT(\gamma-1)}} \sqrt{1 - \left(\frac{P}{P_s} \right)^{(\gamma-1)/\gamma}} \left(\frac{P}{P_s} \right)^{1/\gamma} C_f P_s \quad (5.24)$$

III) Exhausting in the choked regime ($\frac{P_{atm}}{P} \leq C_r$), which yields a proportional function:

$$\dot{m}_3 = -A_v \sqrt{\frac{\gamma}{RT}} \left(\frac{2}{\gamma+1} \right)^{(\gamma+1)/(\gamma-1)} C_f P = -C_1 P \quad (5.25)$$

IV) Exhausting in the unchoked regime ($\frac{P_{atm}}{P} > C_r$), which also yields the following

function:

$$\dot{m}_4 = -A_v \sqrt{\frac{2\gamma}{RT(\gamma-1)}} \sqrt{1 - \left(\frac{P_{atm}}{P} \right)^{(\gamma-1)/\gamma}} \left(\frac{P_{atm}}{P} \right)^{1/\gamma} C_f P \quad (5.26)$$

Subsequently, the mass flow rate equations (5.23)-(5.26) can be substituted into the pressure dynamics equation (5.20). The resulting equations and the corresponding solutions are summarized below:

I) Charging in the choked regime:

$$\dot{P} + \left(\frac{\dot{V}}{V} \right) P = \frac{RT}{V} C_1 P_s \quad (5.27)$$

with the solution as

$$P(t) = P_0 \exp\left(-\frac{\dot{V}}{V}t\right) + \frac{RT}{\dot{V}} C_1 P_s \left[1 - \exp\left(-\frac{\dot{V}}{V}t\right) \right] \quad (5.28)$$

where P_0 is the initial chamber pressure. From the equation above, the pressure at the end of the switching period can be calculated as $P(T_s)$ (T_s is the length of the switching period).

II) Charging in the unchoked regime:

$$\dot{P} = \frac{RT}{V} \dot{m}_2 - \frac{\dot{V}}{V} P \quad (5.29)$$

with \dot{m}_2 defined by Eq. (5.24). Due to the complex form, it is difficult to obtain an analytical solution of this differential equation. As such, a numerical integration can be performed over the switching period to obtain $P(T_s)$. To reduce the computation load in the real-time implementation, a look-up table can be established for the \dot{m}_2 function to accelerate the operation.

III) Exhausting in the choked regime:

$$\dot{P} = - \left(\frac{RTC_1 + \dot{V}}{V} \right) P \quad (5.30)$$

with the solution as

$$P(t) = P_0 \exp\left[- \left(\frac{RTC_1 + \dot{V}}{V} \right) t\right] \quad (5.31)$$

IV) Exhausting in the unchoked regime:

$$\dot{P} = \frac{RT}{V} \dot{m}_4 - \frac{\dot{V}}{V} P \quad (5.32)$$

with \dot{m}_4 defined by Eq. (5.26). Similar to Scenario (II), it is difficult to obtain an analytical solution. As such, a numerical integration, performed with a look-up table on the \dot{m}_4 function, can be used to calculate $P(T_s)$.

After the predicted pressure is calculated, a simple comparison can be performed to determine if the control valve should be switched off at the current time step. Specifically, the desired pressure P_d is calculated according to the desired chamber mass m_d by using Eq. (5.7) (for Chamber *a*) or Eq. (5.8) (for Chamber *b*).

Subsequently, if the predicted pressure $P(T_s)$ exceeds P_d (for pressurizing) or falls below P_d (for exhausting), the valve should be switched to the central closed position. Otherwise, the valve should stay at the current position for the current time step, and the calculation described above should be repeated until the switching condition is met. Once the valve is switched to the central closed position, no further calculation is needed until the stiffness/equilibrium point change to the next set of value.

5.4 EXPERIMENTAL RESULTS

Experiments were conducted and presented to demonstrate the performance of the proposed approach in this section. The experimental setup includes a double-acting pneumatic cylinder (0750D02-04A, Numatics Incorporated, Novi, Michigan, USA) mounted on a vibration-isolated table. The piston in the pneumatic cylinder is connected to a moving block mounted on a linear slide, which defines the piston motion and allows a human operator to manually move the piston. Each of the two chambers of the cylinder is connected to a 3-position, closed-centered

solenoid valve (VQ1300K-5B1, SMC Corporation, Tokyo, Japan) for independent pressure control. Sensors in the experimental setup include a pair of pressure transducers (SDET-22T-D25-G14-U-M12, FESTO, Esslingen, Germany) for the measurement of chamber air pressures and a linear potentiometer (LP-100F, Midori Precisions Co., Tokyo, Japan) for the measurement of the piston position. A photo of the experimental setup is shown in Fig. 5-4, and the model and control parameters are listed in Table 5-1.

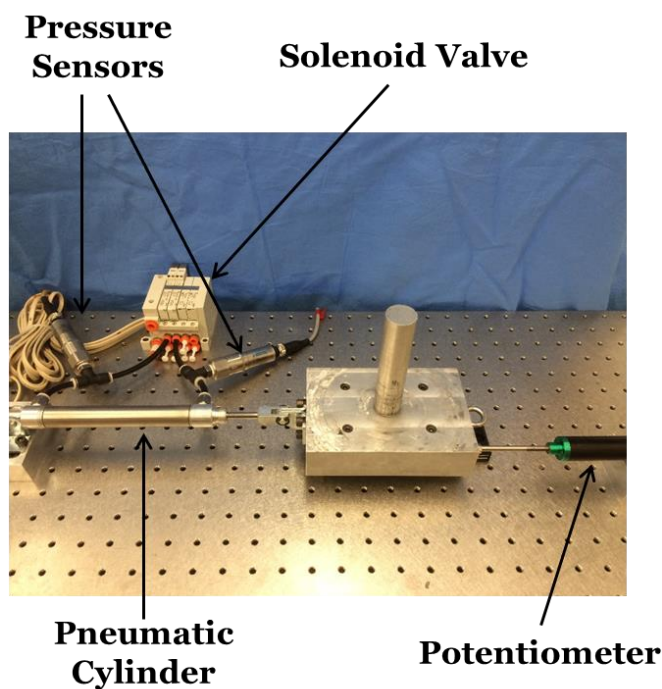


Figure 5-4: Experimental setup.

Table 5-1: Model and control parameters.

Parameter	Description	Value	Unit
P_s	Supply pressure	653	kPa
A_a	Piston area side a	285	mm ²
A_b	Piston area side b	253	mm ²
A_r	Rod area	32	mm ²
L	Cylinder stroke	102	mm
C_f	Discharge coefficient	0.8	
C_r	Pressure ratio	0.5	
γ	Ratio of specific heats	1.4	
R	Universal gas constant	0.287	kJ/kg·K
T	Gas temperature	293	K
L_{da}	Dead length side a	6.6	mm
L_{db}	Dead length side b	6.6	mm

The primary purpose of the experiments is to demonstrate the advantage of using the pneumatic actuator as a VSEA. With this approach, the pneumatic VSEA enables the implementation of stiffness control without the high-frequency control action required for closed-loop control. In the experiments, the pneumatic VSEA, starting from an at-rest state (both chambers at atmospheric pressure), implemented the stiffness control as described in the previous section to obtain a desired set of stiffness/equilibrium point. The piston of the actuator was subject to a reciprocating motion imposed by a human operator. The output force of the actuator recorded in this process is then compared to the desired reaction force calculated from the artificial spring behavior

$$F_d = -K(x - x_e) \quad (5.33)$$

Such comparison serves the purpose of demonstrating the accuracy of stiffness control of the pneumatic VSEA. A set of typical results is shown in Figs. 5-5 to 5-8, including the plots of

piston motion (Fig. 5-5), comparison of desired versus measured actuator forces (Fig. 5-6, in which the forces are inverted to better match the motion plot), position-force relationship (Fig. 5-7), and valve commands (Fig. 5-8, in which 1 represents pressurizing, 0 represents being closed, and -1 represents exhausting). In this experiment, an artificial spring with the stiffness of 15 N/mm and equilibrium point at 5 mm was implemented starting at $t = 2$ s. It can be clearly observed that the measured output force closely matches the desired output force in Fig. 5-6, indicating that the pneumatic VSEA is able to provide the desired elastic behavior of the artificial spring. Such elastic behavior is more clearly shown in the position-force plot (Fig. 5-7). In this figure, the desired spring behavior is represented by a straight line, indicating a linear spring with a fixed equilibrium point. The measured actuator behavior, as represented by the force trajectory, closely matches the desired spring behavior. Small hysteresis loops are present, but the deviation is very small, demonstrating the validity of the elasticity model derived in Sec. 5.2. In the valve command plots (Fig. 5-8), only one short cycle of valve switching is displayed for each valve, indicating minimum control action and minimal involvement of closed-loop control.

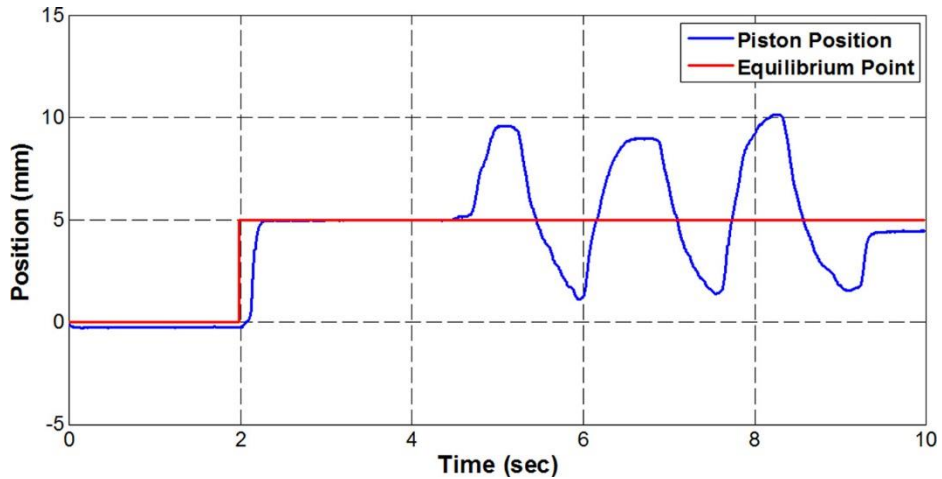


Figure 5-5: Piston position trajectory in the pneumatic VSEA experiment.

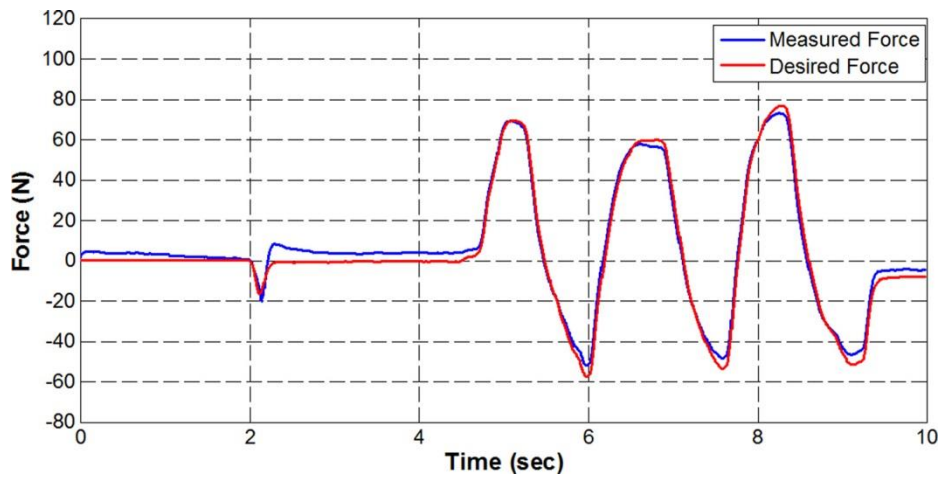


Figure 5-6: Desired versus measured actuator force in the pneumatic VSEA experiment.

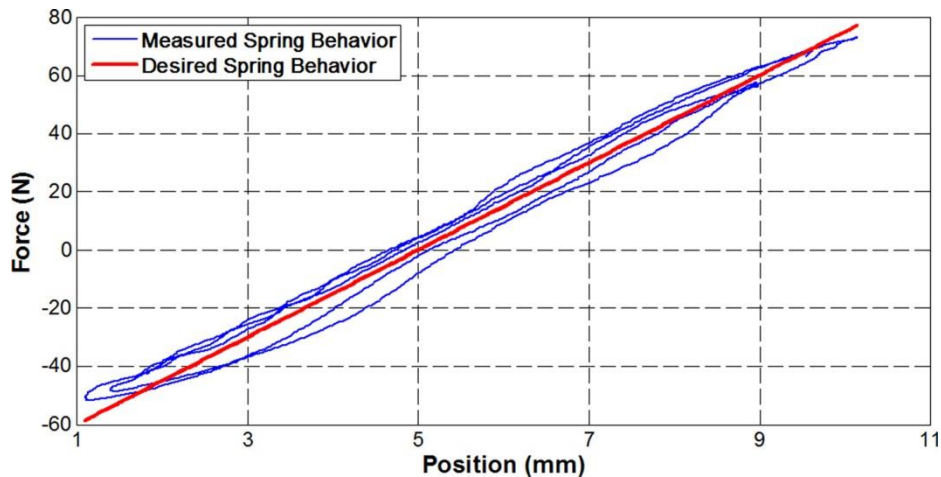


Figure 5-7: Measured versus desired spring behavior in the pneumatic VSEA experiment.

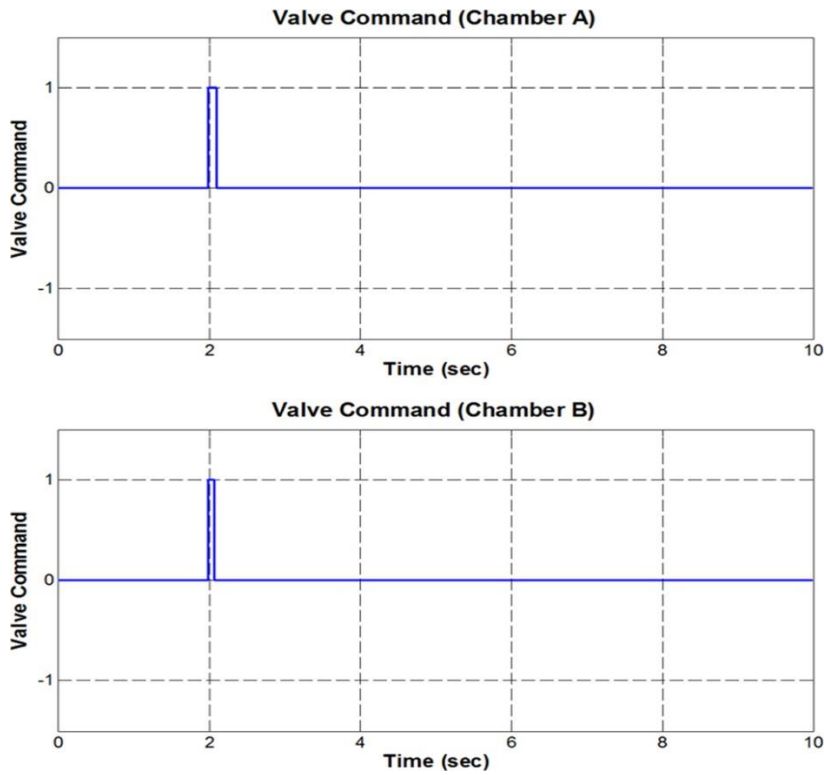


Figure 5-8: Solenoid valve commands for chambers a and b in the pneumatic VSEA experiment.

Furthermore, a set of experiments that involves the transition between two different sets of stiffness/equilibrium point has also been conducted, with the purpose of demonstrating the controller's capability in modulating the dynamic characteristics of the pneumatic VSEA in real-time. Typical results of such experiments are shown in Fig. 5-9 and 5-10. In this experiment, an artificial spring with the stiffness of 5 N/mm and equilibrium point at 5 mm was implemented starting at $t = 2$ s. Eight seconds later ($t = 10$ s), the springs parameters switched to 7 N/mm and 18 mm for the stiffness and equilibrium point, respectively. The piston motion, as compared with the equilibrium point, is shown in Fig. 5-9, with the corresponding forces shown in Fig. 5-10. As can be seen in Fig. 5-10, except for the short transitional period following $t = 10$ s, the measured

output force closely matches the desired output force, demonstrating that the pneumatic VSEA is able to modulate the artificial spring behavior in real-time.

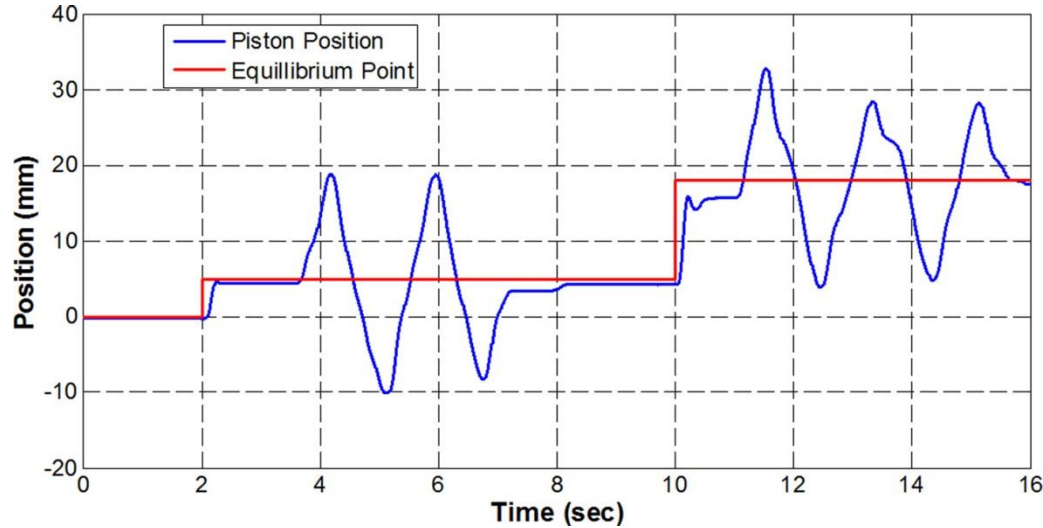


Figure 5-9: Piston position trajectory in the experiment that involves the transition between two different sets of stiffness/equilibrium point.

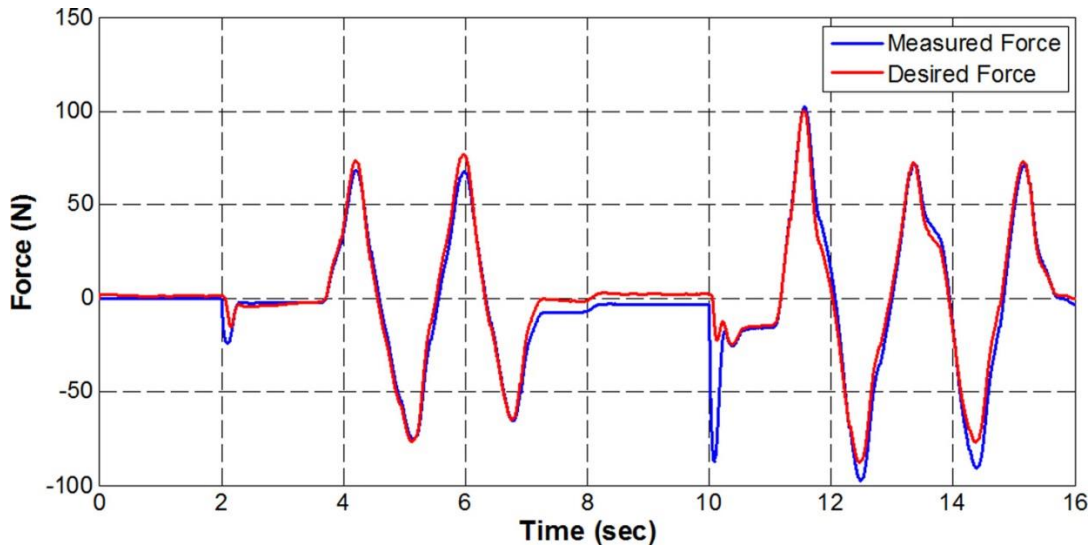


Figure 5-10: Desired versus measured actuator force in the experiment that involves the transition between two different sets of stiffness/equilibrium point.

To provide a quantitative comparison of the proposed approach versus the traditional close-loop implementation of stiffness control, another set of experiments were conducted, in which the pneumatic actuator was used as a traditional force-control actuator for the close-loop implementation of stiffness control. The same artificial spring was implemented in this set of experiments. To improve the force control performance, the solenoid valves were replaced with a high-bandwidth proportional valve (MPYE-5-M5-010-B, FESTO, Esslingen, Germany). The force control was conducted by using a simple PID controller, with the desired force calculated from the desired artificial spring behavior according to Eq. (5.33). The results are shown in Figs. 5-11 to 5-14, including the plots of piston motion (Fig. 5-11), comparison of desired versus measured actuator forces (Fig. 5-12, in which the forces are inverted to better match the motion plot), position-force relationship (Fig. 5-13), and valve command (Fig. 5-14, in which the valve command IS normalized to the range of -1 to 1). Since the motion was generated by the human operator, there is a slight difference in piston motion among different sets of experimental results. Through close-loop control, the force-controlled pneumatic actuator is able to provide the desired elastic behavior (Fig. 5-12), although the performance is slightly inferior to that provided by the pneumatic VSEA (Fig. 5-6). The position-force plot (Fig. 5-13) leads to a similar conclusion, with a slightly bigger deviation from the desired spring behavior when compared with the position-force plot for the pneumatic VSEA (Fig. 5-7). Although the closed-loop implemented stiffness control provides a similar performance as the VSEA, such performance is obtained through the non-stopping action of the proportional valve (Fig. 5-14), which is typical for closed-loop control. Through a comparison between the valve actions (Fig. 5-8 versus Fig. 5-14), it clearly shows that the proposed pneumatic VSEA provides a superior way of

implementing stiffness control and avoiding the multiple issues with close-loop control such as continuous high-frequency control action.

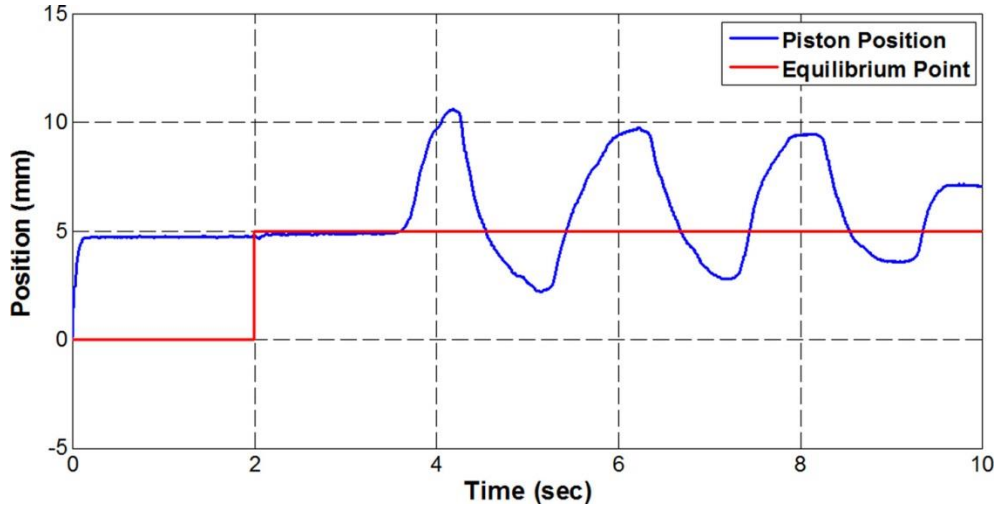


Figure 5-11: Piston position trajectory in the closed-loop implemented stiffness control experiment.

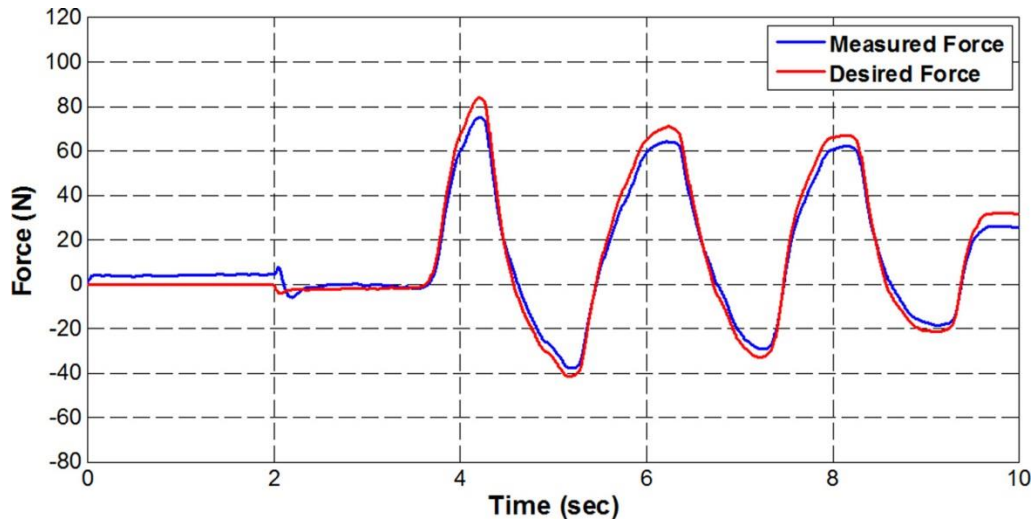


Figure 5-12: Desired versus measured actuator force in the closed-loop implemented stiffness control experiment.

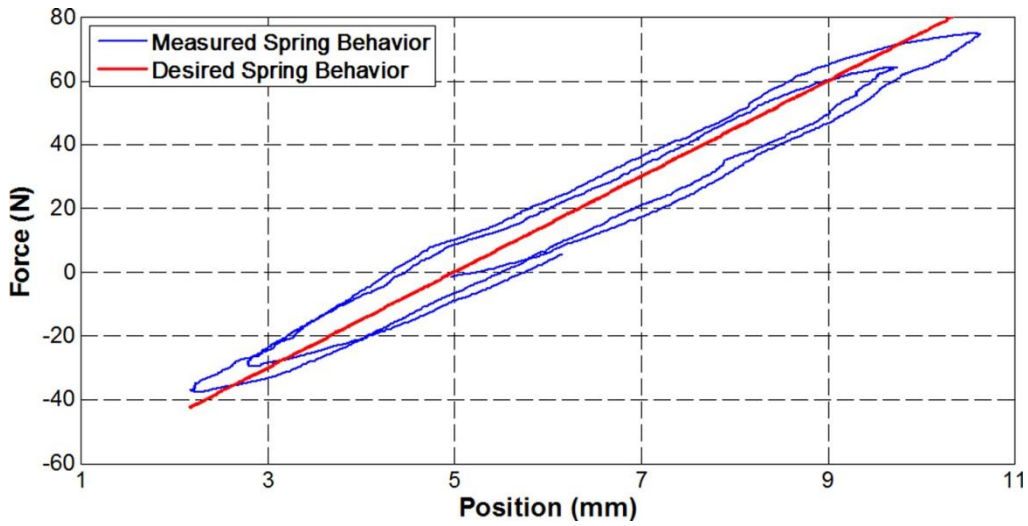


Figure 5-13: Measured versus desired spring behavior in the closed-loop implemented stiffness control experiment.

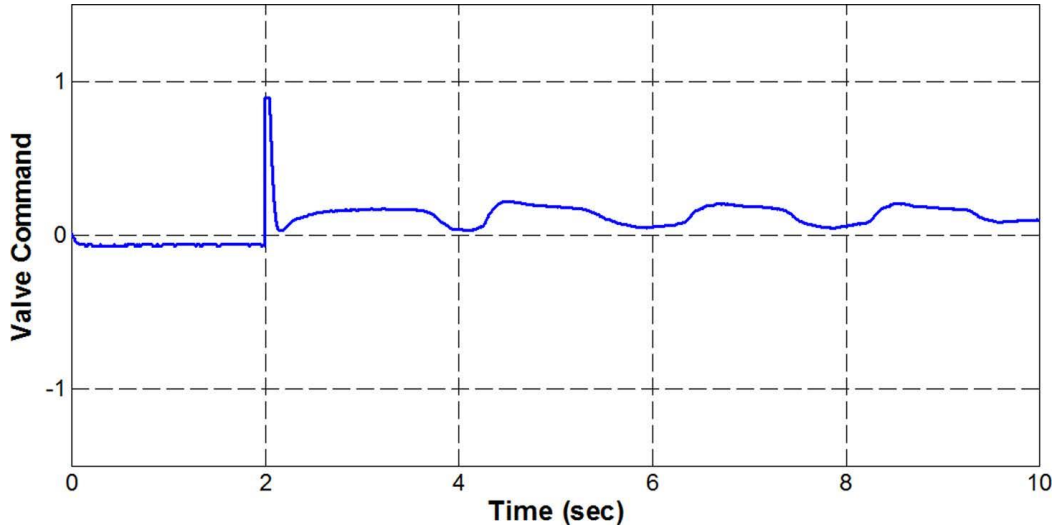


Figure 5-14: Proportional valve command (normalized to -1 to 1 range) in the closed-loop implemented stiffness control experiment.

5.5 CONCLUSIONS

In this chapter, a new approach to implement stiffness control for robotic system has been presented. With its compressible working fluid, a pneumatic actuator features a physically existing elasticity that can be modulated with its air masses. Leveraging this unique feature, a

model that characterizes the stiffness and equilibrium point as functions of the chamber air masses in the actuator has been developed. Subsequently, a stiffness control approach was developed, in which a predictive pressure control algorithm is used to improve pressure control performance while minimizing valve action. This enables the pneumatic actuator to be used as a variable series elastic actuator (VSEA). Experimental results showed that the proposed approach is able to provide the desired elastic characteristics of an artificial spring in stiffness control. Compared with the traditional close-loop control-based implementation, the pneumatic VSEA is an open-loop system, and thus is free of the multiple issues that affect the closed-loop systems (time delay, limited bandwidth, etc.). On the other hand, due to the nonlinearity of the air pressure dynamics, the stiffness of the pneumatic VSEA varies with the piston displacement, which requires special attention while the displacement is significant.

The pneumatic VSEA in this paper has a potential of replacing the existing force-controlled robotic actuators in interactive tasks such as manipulation and human assistance. A typical example is the actuation of lower-limb prostheses, which involve constant interaction with the human users. For the control of such prosthetic devices, the finite-state impedance control approach is especially effective in enabling human–robot interaction and restoring normal walking gait [9]. This approach requires the implementation of artificial impedance (primarily an artificial spring, complemented with a small artificial damper), with the parameters switching between different sets of values during phase transitions. Using the pneumatic VSEA to replace the existing force-controlled actuator, the implementation of the finite-state impedance approach is expected to be greatly simplified while generating better control performance. Leveraging the research in this area [24-26], the authors' group investigated such possibility and

further compared the performances of the pneumatic VSEA versus the traditional force-controlled actuator in the next chapter.

5.6 ACKNOWLEDGMENT

This work was supported by the National Institutes of Health under Grant No. R01HD075493 and the National Science Foundation under Grant No. CBET-1351520.

REFERENCES

- [1] Salisbury, J. K. (1980, December). Active stiffness control of a manipulator in Cartesian coordinates. In *Decision and Control including the Symposium on Adaptive Processes, 1980 19th IEEE Conference on* (Vol. 19, pp. 95-100). IEEE.
- [2] Hogan, N. (1985). Impedance control: An approach to manipulation. *Journal of dynamic systems, measurement, and control*, 107, 17.
- [3] Feldman, A. G., & Levin, M. F. (1995). The origin and use of positional frames of reference in motor control. *Behavioral and brain sciences*, 18(04), 723-744.
- [4] Hogan, N. (1980). Tuning muscle stiffness can simplify control of natural movement. In *Advances in Bioengineering, ASME Winter Annual Meeting* (pp. 279-282).
- [5] Hogan, N. (1984). Adaptive control of mechanical impedance by coactivation of antagonist muscles. *IEEE Transactions on Automatic Control*, 29(8), 681-690.
- [6] Hogan, N. (1985). The mechanics of multi-joint posture and movement control. *Biological Cybernetics*, 52(5), 315-331.
- [7] Cavagna, G. A., Heglund, N. C., & Taylor, C. R. (1977). Mechanical work in terrestrial locomotion: two basic mechanisms for minimizing energy expenditure. *American Journal of Physiology-Regulatory, Integrative and Comparative Physiology*, 233(5), R243-R261.
- [8] Taylor, C. R., & Heglund, N. C. (1982). Energetics and mechanics of terrestrial locomotion. *Annual Review of Physiology*, 44(1), 97-107.
- [9] Sup, F., Bohara, A., & Goldfarb, M. (2008). Design and control of a powered transfemoral prosthesis. *The International journal of robotics research*, 27(2), 263-273.
- [10] Pratt, G. A., & Williamson, M. M. (1995, August). Series elastic actuators. In *Intelligent Robots and Systems 95.'Human Robot Interaction and Cooperative Robots', Proceedings. 1995 IEEE/RSJ International Conference on* (Vol. 1, pp. 399-406). IEEE.
- [11] Robinson, D. W., Pratt, J. E., Paluska, D. J., & Pratt, G. A. (1999). Series elastic actuator development for a biomimetic walking robot. In *Advanced Intelligent Mechatronics, 1999. Proceedings. 1999 IEEE/ASME International Conference on* (pp. 561-568). IEEE.
- [12] Pratt, J., Krupp, B., & Morse, C. (2002). Series elastic actuators for high fidelity force control. *Industrial Robot: An International Journal*, 29(3), 234-241.

- [13] Laurin-Kovitz, K. F., Colgate, J. E., & Carnes, S. D. (1991, April). Design of components for programmable passive impedance. In *Robotics and Automation, 1991. Proceedings., 1991 IEEE International Conference on* (pp. 1476-1481). IEEE.
- [14] Koganezawa, K., & Yamazaki, M. (1999). Mechanical stiffness control of tendon-driven joints. In *Intelligent Robots and Systems, 1999. IROS'99. Proceedings. 1999 IEEE/RSJ International Conference on* (Vol. 2, pp. 818-825). IEEE.
- [15] Koganezawa, K., & Ban, S. (2002). Stiffness control of antagonistically driven redundant DOF manipulator. In *Intelligent Robots and Systems, 2002. IEEE/RSJ International Conference on* (Vol. 3, pp. 2280-2285). IEEE.
- [16] English, C. E., & Russell, D. (1999). Mechanics and stiffness limitations of a variable stiffness actuator for use in prosthetic limbs. *Mechanism and Machine Theory*, 34(1), 7-25.
- [17] English, C., & Russell, D. (1999). Implementation of variable joint stiffness through antagonistic actuation using rolamite springs. *Mechanism and Machine Theory*, 34(1), 27-40.
- [18] Hurst, J. W., Chestnutt, J. E., & Rizzi, A. A. (2004, April). An actuator with physically variable stiffness for highly dynamic legged locomotion. In *Robotics and Automation, 2004. Proceedings. ICRA'04. 2004 IEEE International Conference on* (Vol. 5, pp. 4662-4667). IEEE.
- [19] Tonietti, G., Schiavi, R., & Bicchi, A. (2005, April). Design and control of a variable stiffness actuator for safe and fast physical human/robot interaction. In *Robotics and Automation, 2005. ICRA 2005. Proceedings of the 2005 IEEE International Conference on* (pp. 526-531). IEEE.
- [20] Bicchi, A., Rizzini, S. L., & Tonietti, G. (2001). Compliant design for intrinsic safety: General issues and preliminary design. In *Intelligent Robots and Systems, 2001. Proceedings. 2001 IEEE/RSJ International Conference on* (Vol. 4, pp. 1864-1869). IEEE.
- [21] Tonietti, G., & Bicchi, A. (2002). Adaptive simultaneous position and stiffness control for a soft robot arm. In *Intelligent Robots and Systems, 2002. IEEE/RSJ International Conference on* (Vol. 2, pp. 1992-1997). IEEE.
- [22] Shen, X., & Goldfarb, M. (2007). Simultaneous force and stiffness control of a pneumatic actuator. *Journal of Dynamic Systems, Measurement, and Control*, 129(4), 425-434.

- [23] Taheri, B., Case, D., & Richer, E. (2014). Force and stiffness backstepping-sliding mode controller for pneumatic cylinders. *IEEE/ASME Transactions on Mechatronics*, 19(6), 1799-1809.
- [24] Zheng, H., & Shen, X. (2015). Design and control of a pneumatically actuated transtibial prosthesis. *Journal of Bionic Engineering*, 12(2), 217-226.
- [25] Zheng, H., & Shen, X. (2015). A Pneumatically Actuated Transtibial Prosthesis. *Journal of Medical Devices*, 9(3), 030919.
- [26] Wu, M., Zheng, H., & Shen, X. (2015). A Pneumatically Actuated Knee Prosthesis. *Journal of Medical Devices*, 9(3), 030911.

CHAPTER 6: A PNEUMATIC VARIABLE SERIES ELASTIC ACTUATOR-POWERED TRANSTIBIAL PROSTHESIS

6.1 INTRODUCTION

In human locomotion, the ankle plays an important role in supplying the power and work to support the forward motion. Biomechanical studies show that the ankle produces substantially more work than the knee and hip in level walking [1], and its cumulative energetic behavior over a gait cycle is clearly positive [2]. For the transtibial (below-knee) amputees, loss of the ankle functions results in a significant deficiency in the energetics of the full-body biomechanics. However, existing transtibial prostheses are primarily passive devices, which only dissipate energy, or store and reuse energy within a gait cycle. Such behavior is fundamentally different from that of the biological ankle, constituting a major limitation to the functionality and rehabilitation performance of such devices. A transtibial amputee fitted with a passive prosthesis has to use his/her biological joints to compensate for the lack of mechanical power generation in the prosthetic ankle, and thus suffers from multiple related issues, e.g., asymmetric gait and higher metabolic energy consumption [3,4].

Motivated by this challenge, researchers have developed multiple transtibial prostheses with powered ankle action. The majority of these prosthetic devices are powered by electromagnetic actuators (DC motors) through high gear ratio transmission, with the energy supplied by electrochemical batteries. Furthermore, elastic elements (mechanical springs in

various shapes) are also added in parallel or series with the actuator-transmission unit to reduce the shock loading, add flexibility, and mimic the human musculoskeletal structure. A typical example is the multiple prototypes developed by the MIT Biomechatronics group [5-7], later commercialized as the BioM/emPOWER prosthesis by BionX Medical Technologies [8]. In these devices, a DC motor is coupled with a ball screw assembly to convert the high-speed rotation to slower linear translation, which in turn drives the rotation of the prosthetic ankle through an inverted crank-slider mechanism. Connected in series with the motor-ball screw assembly is a mechanical spring, forming a series elasticity actuator (SEA) system [9]. Other electrically actuated devices are largely in the same “motor + transmission + spring” configuration. The SPARKy ankle prosthesis has a unique 2-degree-of-freedom (2-DOF) ankle joint actuated by two DC motors through ball screw assemblies, and two springs are also incorporated to provide flexibility in both DOFs [10,11]. Researchers in the Center for Intelligent Mechatronics at Vanderbilt University also developed powered ankle prostheses, initially as part of the 2-DOF knee-and-ankle transfemoral prostheses [12], and later as standalone transtibial prostheses [13]. The Vanderbilt designs also include leaf springs to store energy and reduce the required motor torque for powered push-off.

It can be clearly seen from these prior works that various types of mechanical springs play important roles in the powered transtibial prostheses. The fundamental reason for incorporating mechanical springs into powered prostheses is that the prosthetic actuators lack the desired elasticity, and thus have to be complemented with such elastic elements. Consider the prosthetic actuators’ biological counterparts, skeletal muscles. From a dynamic perspective, a skeletal muscle can be modeled as a source of controllable force and impedance, which is supported by the widely accepted equilibrium position hypothesis [14]. In a simplified biological

joint actuation model, two skeletal muscles drive the joint motion in the opposite directions, and the joint stiffness is determined by the sum of the muscle contractions, while the joint torque is determined by the difference in muscle contractions. As such, the stiffness and torque in a biological joint can be controlled simultaneously through the corresponding neural signals for muscle contraction. Such capability serves many important functions, e.g. providing stability in the humans' interaction with the environment [15-17]. Inspired by such scientific findings, impedance/stiffness control has been used extensively in the robots and robotic devices that interact with humans. Specifically for the lower-limb prostheses, impedance control is combined with a finite-state machine to form the finite-state impedance control (FSIC), which has been demonstrated to provide a highly interactive and natural control experience for the amputee users [18].

Note that an FSIC controller cycles through a number of phases (states) in a gait cycle to achieve the desired gait functions. Due to the significantly different impedance characteristics between phases, the mechanical springs in the prosthesis are unlikely to provide the desired impedance in all phases. As such, implementation of the FSIC in a powered prosthesis still relies on feedback-based closed-loop force/torque control, and thus suffers from the related issues such as limited bandwidth and potential instability. The pneumatic VSEA presented in the previous chapter is able to maintain its impedance characteristics when the actuator chambers are completely closed. Such advantage makes the pneumatic VSEA highly suitable for the implementation of the FSIC, as the control action (and the resulted energy consumption) can be reduced to a minimum (i.e., only required during phase transitions).

In this paper, a unique pneumatic VSEA-actuated transtibial prosthesis is presented, including the design of the prosthesis prototype, and the unique prosthesis control approach

based on the variable series elasticity in the VSEA. Two major benefits are expected in comparison with existing powered transtibial prostheses: 1) The inherent elasticity in the pneumatic VSEA eliminates the need for additional mechanical springs, and thus significantly simplifies the design of the prosthesis and reduce the device cost; 2) The simultaneous eq. pt. and stiffness control of the pneumatic VSEA eliminates the need for implementing feedback-based closed-loop force/torque control, and thus significantly reduces the complexity and cost of the prosthesis control system. Overall, the pneumatic VSEA-actuated transtibial prosthesis has a potential of developing into a high-performance, low-cost prosthetic device to benefit the large transtibial amputee population to improve their quality of life.

This chapter is organized as follows: Section 2 presents the design of the pneumatic VSEA-based transtibial prosthesis; Section 3 presents the variable series elasticity-based implementation of the FSIC control of the prosthesis; Section 4 presents the results of the human subject testing of the proposed approach; and Section 5 contains the conclusions.

6.2 PNEUMATIC VSEA-POWERED TRANSTIBIAL PROSTHESIS

In this section, the basic concept of pneumatic VSEA will be described, followed by the design of the transtibial prosthesis prototype powered with a pneumatic VSEA.

6.2.1 PNEUMATIC VARIABLE SERIES ELASTIC ACTUATOR

In a traditional series elastic actuator (SEA), elastic elements, usually helical springs, are connected in series with the motor-transmission assembly to add elasticity to the otherwise rigid actuator [9]. Despite the recent progress made on the development of compact SEA assembly, most SEA packages are still bulky and complex. Pneumatic VSEA, on the other hand, does not

rely on the added elastic elements to obtain the desired elasticity. Instead, it is essentially a double-acting pneumatic cylinder with independently controlled chamber pressures, with the elasticity generated from the compressibility of the working fluid (compressed air). The system configuration, as shown in Fig. 6-1, is very simple. More importantly, the stiffness of the actuator can be controlled independently from the actuation force, which constitutes a major advantage over the traditional SEA. Modeling of a pneumatic VSEA is briefly introduced below, with the details presented in [19].

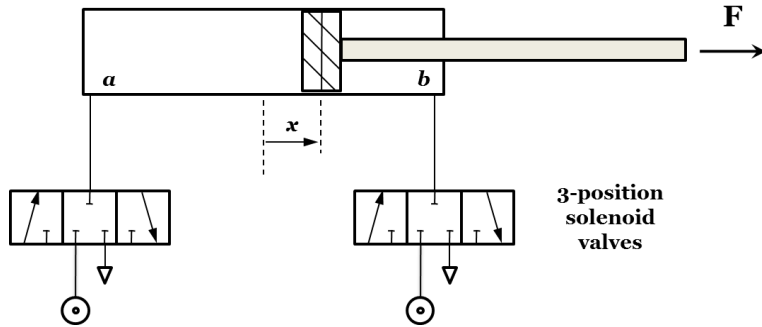


Figure 6-1: Schematic of the pneumatic VSEA

For the implementation of the FSIC, a pneumatic VSEA can be modeled as a virtual spring with controllable stiffness and equilibrium point. For the implementation of the FSIC, a pneumatic VSEA can be modeled as a virtual spring with controllable stiffness and equilibrium point.

$$F = P_a A_a - P_b A_b - P_{atm} A_r \quad (6.1)$$

where P_a is the Chamber a (rodless chamber) pressure, A_a is the piston area facing Chamber a , P_b is the Chamber b pressure, A_b is the piston area facing Chamber b , P_{atm} is the atmospheric pressure, and A_r is the rod cross-sectional area. Note that chamber pressures change with the

piston position, and thus the actuator displays an inherent stiffness as shown by the equation below:

$$K = -\frac{\partial F}{\partial x} = -A_a \frac{\partial P_a}{\partial x} + A_b \frac{\partial P_b}{\partial x} \quad (6.2)$$

where K is the linear stiffness of the actuator, and x is the displacement of the piston. Assuming air is an ideal gas, pressure is a function of the air mass in the chamber:

$$P_a = \frac{m_a RT}{V_a} = \frac{m_a RT}{A_a (\frac{L}{2} + x) + V_{da}} \quad (6.3)$$

$$P_b = \frac{m_b RT}{V_b} = \frac{m_b RT}{A_b (\frac{L}{2} - x) + V_{db}} \quad (6.4)$$

where R is the universal gas constant, T is the air temperature, V_a and V_b are the total chamber volumes, m_a and m_b are the chamber air masses, L is the actuator stroke, and V_{da} and V_{db} are the chamber dead volumes. The dead volumes are the volumes unaffected by the piston motion, and typical examples include the volumes in the air pathways, internal volumes of the connection tubes, etc. To simplify the equation, each of the dead volumes is expressed as the product of the piston area multiplied with a new length variable, namely dead length (L_{da} and L_{db}):

$$V_{da} = A_a L_{da} \quad (6.5)$$

$$V_{db} = A_b L_{db} \quad (6.6)$$

Substituting Eqs. (6.5) and (6.6) into (6.3) and (6.4) yields:

$$P_a = \frac{m_a RT}{A_a (\frac{L}{2} + L_{da} + x)} \quad (6.7)$$

$$P_b = \frac{m_b RT}{A_b (\frac{L}{2} + L_{db} - x)} \quad (6.8)$$

The equations above can be differentiated and then substituted into the stiffness equation (6.2), resulting in the following equations:

$$K = \frac{m_a RT}{\left(\frac{L}{2} + L_{da} + x\right)^2} + \frac{m_b RT}{\left(\frac{L}{2} + L_{db} - x\right)^2} \quad (6.9)$$

Similar to the equation above, the eq. pt. of the pneumatic VSEA can also be expressed as a function of the chamber air masses. No actuation force is generated when the piston position is at the eq. pt.:

$$F_e = P_{ae} A_a - P_{be} A_b - P_{atm} A_r = 0 \quad (6.10)$$

where P_{ae} and P_{be} are the chamber air pressures at the eq. pt., which can be further expressed as chamber air masses:

$$P_{ae} = \frac{m_a RT}{A_a \left(\frac{L}{2} + L_{da} + x_e\right)} \quad (6.11)$$

$$P_{be} = \frac{m_b RT}{A_b \left(\frac{L}{2} + L_{db} - x_e\right)} \quad (6.12)$$

After substituting (6.11) and (6.12) into (6.9), the following equation can be obtained, which serves as an implicit description of the eq. pt. x_e as a function of chamber air masses:

$$\frac{m_a RT}{\frac{L}{2} + L_{da} + x_e} - \frac{m_b RT}{\frac{L}{2} + L_{db} - x_e} - P_{atm} A_r = 0 \quad (6.13)$$

Equations (6.9) and (6.13) can then serve as the two-input-two-output model of the pneumatic VSEA, which can be further consolidated into a single matrix equation:

$$[\mathbf{A}] \begin{Bmatrix} m_a \\ m_b \end{Bmatrix} = \{\mathbf{B}\} \quad (6.14)$$

where

$$[\mathbf{A}] = \begin{bmatrix} \frac{RT}{\left(\frac{L}{2} + L_{da} + x\right)^2} & \frac{RT}{\left(\frac{L}{2} + L_{db} - x\right)^2} \\ \frac{RT}{\frac{L}{2} + L_{da} + x_e} & -\frac{RT}{\frac{L}{2} + L_{db} - x_e} \end{bmatrix} \quad (6.15)$$

$$\{\mathbf{B}\} = \begin{Bmatrix} K \\ P_{atm} A_r \end{Bmatrix} \quad (6.16)$$

As such, to implement the desired eq. pt. and stiffness, the desired chamber air pressures can be calculated from the following equation:

$$\begin{Bmatrix} m_a \\ m_b \end{Bmatrix} = [\mathbf{A}]^{-1} \{\mathbf{B}\} \quad (6.17)$$

which can be further converted the desired air pressures through Eqns. (6.7) and (6.8). Subsequently, simple pressure control can be conducted, which generates the commands for the solenoid valve actions. Fig. 6-2 shows the controller schematic of the pneumatic VSEA, with the desired eq. pt. and stiffness as the input, and the solenoid valve commands as the output.

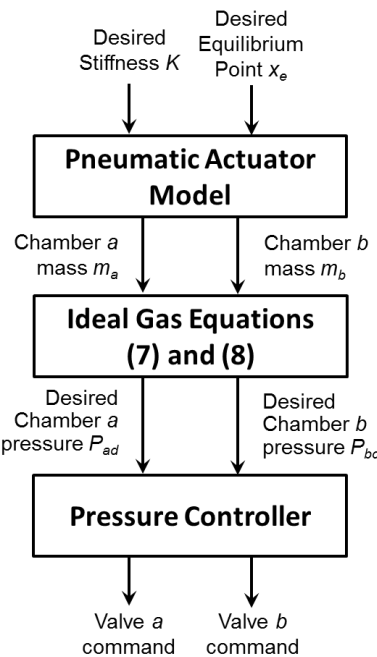


Figure 6-2: Controller structure of the pneumatic VSEA

6.2.2 PNEUMATIC VSEA-POWERED TRANSTIBIAL PROSTHESIS PROTOTYPE

To demonstrate the concept of the pneumatic VSEA-powered transtibial prosthesis, a preliminary prototype has been developed and fabricated, as shown in Fig. 6-3. This prototype

was developed based on the author's prior work on pneumatic transtibial prosthesis [20], with an identical actuation mechanism. The major difference from the prior work is that the pneumatic actuator has been reconfigured as a VSEA, enabling the direct implementation of the FSIC prosthesis controller (to be described in Sec. 3).

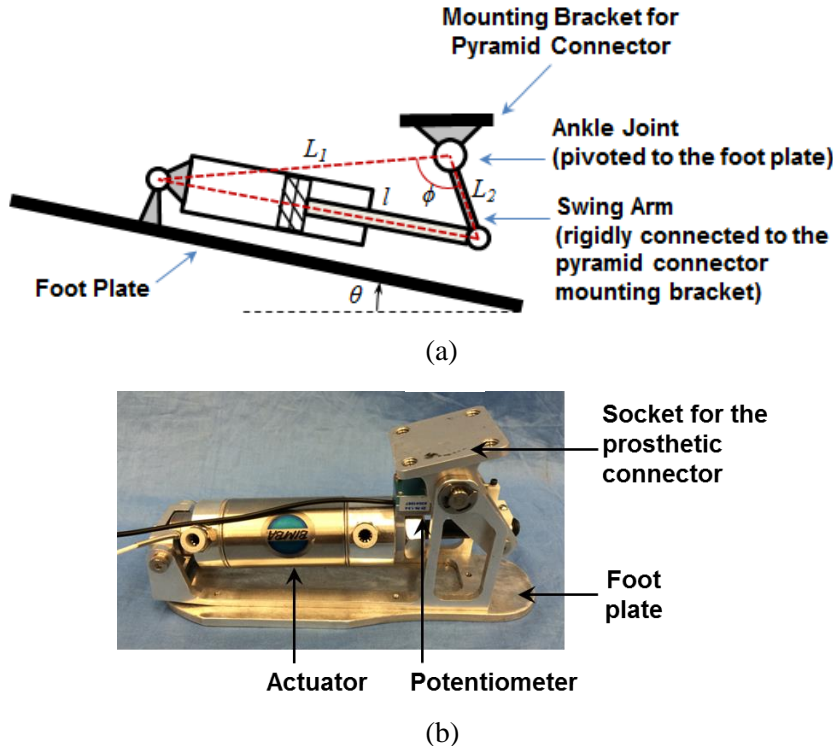


Figure 6-3: The pneumatic VSEA-powered transtibial prosthesis: (a) schematic of the actuation system; (b) a photo of the prototype.

To minimize the height of the prosthesis, the pneumatic actuator is mounted in the horizontal direction, with the rodless end pivoted to the foot plate, and the piston rod connected to a short swing arm through a pin joint. The swing arm is rigidly connected to the mounting bracket for the prosthetic pyramid connector to form a single rigid piece, which can rotate with respect to the ankle joint. As such, the pneumatic actuator's linear motion is converted to the

rotation of the ankle through an inverted crank-slider mechanism, which minimizes the mechanical complexity of the system. Correspondingly, the linear stiffness of the pneumatic VSEA can be converted to the rotational stiffness of the actuation system. Based on the actuation mechanism shown in Fig. 6-3(a), the joint actuation torque τ can be calculated from the actuator force F :

$$\tau = F \cdot L_m \quad (6.17)$$

where L_m is the effective moment arm, which can be expressed as

$$L_m = \frac{dl}{d\phi} \quad (6.18)$$

According to the geometry shown in Fig. 6-3(a), l can be expressed as a function of ϕ :

$$l = \sqrt{L_1^2 + L_2^2 - 2L_1L_2 \cos\phi} \quad (6.19)$$

Substituting (6.19) into (6.18) yields

$$L_m = \frac{L_1L_2 \sin\phi}{\sqrt{L_1^2 + L_2^2 - 2L_1L_2 \cos\phi}} \quad (6.20)$$

Correspondingly, the linear stiffness of the pneumatic VSEA K can be converted to the rotational stiffness of the rotary actuation system K_r with the following equation:

$$K_r = K \cdot L_m^2 \quad (6.21)$$

Due to the prototype nature, off-the-shelf commercial products were used for all major components of this transtibial prosthesis. The pneumatic actuator is a double-acting pneumatic cylinder with 38 mm (1.5 inches) bore size and 32 mm (1.25 inches) stroke (171.25-DP, Bimba Manufacturing, University Park, IL, USA), and a modular multi-unit solenoid valve (VQ1300K-5B1, SMC Corporation, Tokyo, Japan) is chosen for the chamber air pressure regulation. To provide pressure feedback, two small-profile pressure sensors (85C, Measurement Specialties,

Fremont, CA) are embedded into the actuator. Additionally, a string potentiometer (ZX-PA-1.5, UniMeasure, Corvallis, OR, USA) is mounted in parallel with the actuator, which measures the displacement of the piston rod. The displacement signal is then translated into joint rotation through trigonometric calculation. Currently, the prosthesis controller is implemented off-board on a desktop computer running the National Instruments LabView software, and compressed air is supplied from an external air tank at a constant supply pressure. In the future, the control system will be transferred to a microcontroller-based system and integrated into the prosthesis itself. Furthermore, by using a compact pneumatic supply such as the liquid propellant-based system [21], the proposed pneumatic VSEA-powered transtibial prosthesis can potentially be developed into a practical low-cost prosthetic device for the amputees' daily use.

6.3 DIRECTLY IMPLEMENTED FINITE-STATE IMPEDANCE CONTROLLER

For the control of a powered transtibial prosthesis, the ultimate goal is to restore the amputee user's lost ankle-foot functions. To achieve this goal, the prosthesis is expected to function like its biological counterpart and interact with the user and the environment in a natural way. So far the most effective control approach toward this goal is the aforementioned finite-state impedance control (FSIC), which simulates the dynamic behavior of a torsional spring combined with a rotary damper in the prosthetic joint:

$$\tau = K_r(\theta - \theta_0) + P\dot{\theta} \quad (6.22)$$

where θ is the joint position, θ_0 is the eq. pt. of the spring, P is the damping coefficient of the artificial rotary damper, and $\dot{\theta}$ is the joint angular velocity. Note that a powered prosthetic joint already has physically existing damping (i.e., friction), so the contribution of the artificial damping term is minor compared with the artificial spring term. As such, it is possible to neglect

the damping term, and use the pneumatic VSEA to implement the desired impedance directly. In the subsequent analysis in this section, the desired impedance characteristics in different gait phases will be modeled based on existing biomechanical data, and the corresponding control scheme of the pneumatic VSEA-actuated prosthesis will be formulated and simulated.

6.3.1 IMPEDANCE CHARACTERIZATION OF THE ANKLE BEHAVIOR

As the basis of the FSIC prosthesis controller, the biomechanical behavior of the ankle is studied and modeled through impedance characterization. Typical trajectories of joint position and torque of the ankle in slow walking are shown in Fig. 6-4, plotted based on the experimental data from Winter [2]. Note that the torque output of a virtual torsional spring is a function of its deflection, which in turn is determined by the position of the joint. As such, the joint position and torque trajectories are combined to form a position-torque curve, which provides an easy-to-understand representation of the desired spring behaviors in different gait phases (Fig. 6-5).

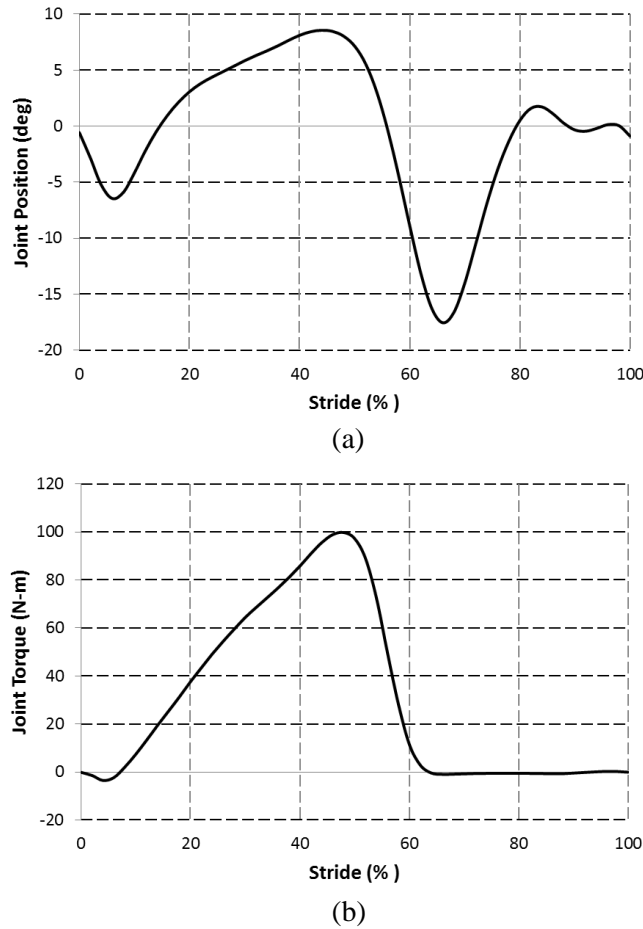


Figure 6-4: Position trajectory (a) and torque trajectory (b) of the ankle in walking (plotted based on the data from [2]).

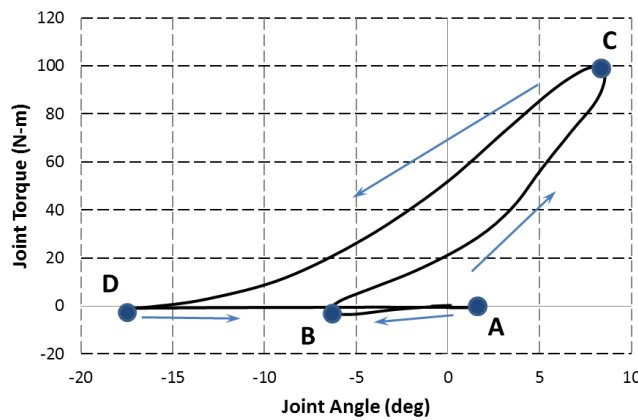


Figure 6-5: Position-torque curve generated by combining the position and torque trajectories in Fig. 6-4.

Figure 6-5 also shows the four important gait events that segment a gait cycle into four distinct phases. Event A is heel strike, which marks the start of the gait cycle; Event B is foot flat, when the foot starts to lie completely flat on the ground; Event C is maximum dorsiflexion, when the joint position reaches the maximum value; Event D is toe off, when the toe leaves the ground. Correspondingly, the four phases in the gait cycle are defined as follows:

#1: **Early Stance** (A→B): The foot plantarflexes until it lays flat on the ground, and the ankle provides a small resistive torque that increases with joint position, which can be modeled with a spring with moderate stiffness (~0.7 N-m/deg) to provide shock absorption and appropriate resistance in the ankle plantarflexion.

#2: **Middle Stance** (B→C): The foot stays flat on the ground while the shank rotates forward, while the ankle provides a rapidly increasing torque, which can be modeled with a very stiff spring (~6.5 N-m/deg) to absorb energy to prepare for the subsequent push-off.

#3: **Late Stance** (C→D): The foot pushes the ground to propel the body forward, while the ankle torque decreases in the process. The ankle behavior can be modeled with a spring slightly less stiff than that in Middle Stance (~3.8 N-m/deg). Despite the lower stiffness, the torque in this phase is considerably higher than that in Middle Stance (at the same joint position), constituting the powered push-off. Such effect can be modeled with a shift of the equilibrium point of the artificial torsional spring, from approximately -7° in Middle Stance to approximately -17° in this phase.

#4: **Swing** (D→A): The foot is completely in the air, with the toe quickly moving up with the ankle dorsiflexion to create ground clearance and prepare for the next heel strike. The ankle behavior can be modeled with a very soft spring that pushes the ankle to a slightly dorsiflexed position.

6.3.2 DIRECT IMPLEMENTATION OF FSIC CONTROLLER WITH PNEUMATIC VSEA

Based on the results of the ankle behavior impedance characterization, the directly implemented FSIC controller is formulated and simulated. Unlike the traditional feedback control-based FSIC implementation, the direct implementation exploits the physically existing and controllable stiffness in the pneumatic VSEA, and thus significantly simplifies the required hardware and minimizes the control action in the operation. Note that the dynamics of air flow (for pressurizing and exhausting the actuator chambers) is in general much faster than the physical movement of the prosthetic joint. As such, an important assumption adopted in the analysis is that the desired chamber pressure can be reached accurately and instantaneously. Such assumption may generate a small amount of error in the actual controller implementation, but the significant simplification of the modeling and simulation process outweighs this weakness.

Two important limitations were taken into consideration in the controller formulation. 1) Due to the use of the off-the-shelf solenoid valve, the maximum gauge pressure for the valve operation is limited to 1034 kPa (150 psi), equivalent to the absolute pressure of 1136 kPa (164.7 psi). As such, the supply pressure is also chosen at the same value, which dictates the maximum pressure each actuator chamber can reach in pressurization. The chamber pressure in operation, nonetheless, may exceed the supply pressure when being compressed (e.g., in the Middle Stance). This is in fact a desirable effect, as the actuator chamber essentially functions as an energy storage device that stores and reuses energy to reduce the overall consumption. 2) The stiffness of a closed pneumatic VSEA (with constant chamber masses m_a and m_b) still varies with the piston position x , as shown in Eq. (6.9). Such variation is especially significant when the piston moves close to either end of the actuator. As a result, the position–torque relationship is not linear, but rather a curve with changing gradient as represented in the position–torque plot. In the

simulation, such relationship is exactly calculated via the position-related chamber pressure change, which generates a closer match to the actual physical system than linearization-based approximation.

Under the limitations described above, the controller is formulated by determining the initial desired chamber pressures for each phase, as well as the construction of the finite state machine for phase transition. The pressure setpoints are summarized as follows.

#1: **Early Stance** (A→B): The initial stiffness is set at 0.8 N-m/deg with the eq. pt. of 1.72°, which are converted to the chamber pressures of 214 kPa and 185 kPa for Chambers *a* and *b*, respectively.

#2: **Middle Stance** (B→C): The initial stiffness is set at 4.3 N-m/deg with the eq. pt. of -5°, which can be converted to the chamber pressures of 1136 kPa and 1096 kPa for Chambers *a* and *b*, respectively. The selected stiffness value is lower than that shown in the biomechanical data, as the chamber pressures are limited by the valve maximum operating pressure as described above. However, with the considerable displacement in this phase, the stiffness increases significantly when the piston approaches the ends of the cylinder, resulting in a closer match to the biomechanical data.

#3: **Late Stance** (C→D): At the end of the Middle Stance phase, the air in Chamber *b* is compressed, and thus increases to 2657 kPa, significantly higher than the supply pressure. As such, the valve for this chamber should stay closed to maintain the pressure. Chamber *a* pressure, expected to be 731 kPa at the end of MS, needs to be lowered to ~264 kPa to increase the actuation torque for a powered push-off.

#4: **Swing** (D→A): In this phase, the joint swings back to a slightly dorsiflexed position under a very soft spring. To avoid creating excessive resistance to joint motion due to air

compression-generated pressure increase, Chamber *b* should be exhausted over the entire phase, which Chamber *a* should be pressurized slightly (~196 kPa) at the beginning to initiate a smooth swing motion.

The values discussed above are obtained through simulation using the biomechanical joint motion data from Winter [2]. Figure 6-6 shows the position–torque curve generated by the control approach described above. Comparing the position–torque curves in Figs. 6-5 and 6-6, it can be observed that the curves are very similar in shape, and the locations of the gait events (A through D) and the peak torques also match each other well. This observation clearly indicates that the directly implemented FSIC controller is able to generate a dynamic behavior similar to the biomechanical behavior of the biological ankle in walking.

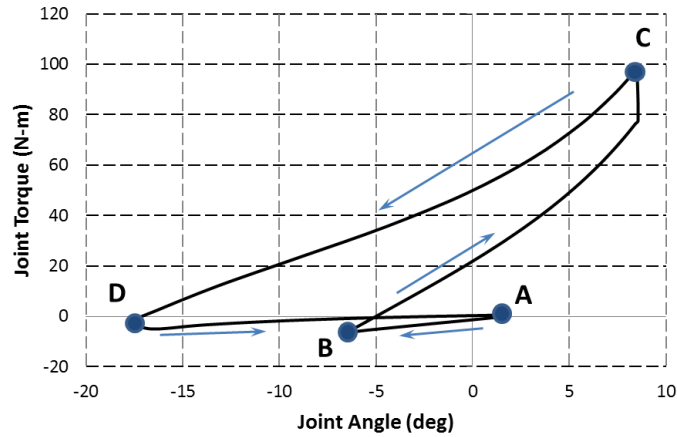


Figure 6-6: Position-torque curve generated by the theoretical simulation of the directly implemented FSIC controller.

For the real-time implementation of this control approach, a finite-state machine is also constructed (Fig. 6-7). In addition to the four phases defined above, it also includes the triggering conditions for phase transitions to facilitate the real-time implementation in the pneumatic

VSEA-actuated transtibial prosthesis. Specifically, for the transition from Swing to Early Stance, the event of Heel Strike is detected according to the onset of plantarflexion ($\dot{\theta} < 0$); for the transition from Early Stance to Middle Stance, the event of Foot Flat is detected according to the onset of dorsiflexion ($\dot{\theta} > 0$); for the transition from Middle Stance to Late Stance, the event of Maximum Dorsiflexion is detected when the joint angle exceeds a threshold value Θ_1 , with the specific value at approximately $7\text{--}8^\circ$; for the transition from Late Stance to Swing, the event of Toe Off is detected when the joint angle exceeds a second threshold Θ_2 , with the specific value at approximately -16° . With these conditions, the phase transitions can be triggered reliably for the functioning of the FSIC controller.

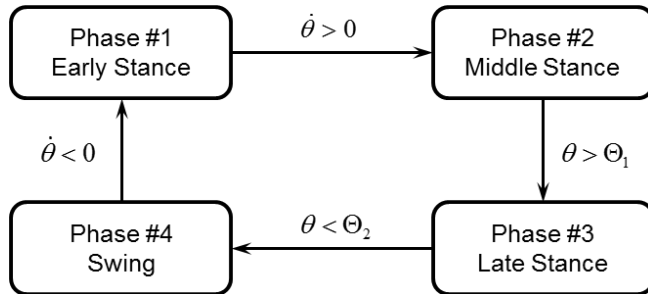


Figure 6-7: Finite state machine of the directly implemented FSIC controller.

6.4 EXPERIMENTAL TESTING RESULTS

The pneumatic VSEA-actuated transtibial prosthesis and its directly implemented FSIC controller have been experimentally tested to evaluate the performance in restoring the user's locomotive functions. To reduce the risk in testing, a healthy subject was used in the study. The male subject was 29 years old, 180 cm in height, and weighed 68 kg. A pair of able-bodied adapters were fabricated based on a pair of inline skates (Zetrablade, Rollerblade, Trenton, NJ, USA), with the wheel assemblies removed and replaced with a steel plate to mount the standard

female pyramid connectors. To maintain lateral balance in testing, a commercial prosthetic foot (LP Vari-Flex, Ossur, Reykjavik, Iceland) was fitted underneath the left adapter when the powered transtibial prosthesis fitted underneath the other adapter.



Figure 6-8: The test subject fitted with the pneumatic VSEA-actuated transtibial prosthesis.

Walking experiments were conducted on a commercial treadmill (T91, Horizon Fitness, Cottage Grove, WI, USA) augmented with custom hand rails and overhead harness for safety protection. Repeated tuning was conducted to optimize the control performance, which was assessed through the objective evaluation (comparison with standard biomechanical data) and subjective evaluation (feedback from the test subject). A typical set of experimental results is shown in Fig. 6-9, including the joint position and torque trajectories. Comparing these results with the biomechanical data as shown in Fig. 6-4, it can be clearly seen that the joint position trajectory is smooth and close to the standard biomechanical trajectory throughout the entire gait cycle. The joint torque curve resembles the biological joint torque curve, and displays more obvious transition due to the use of the FSIC controller. The peak torque recorded during the

powered push-off is approximately 55 Nm, primarily limited by the maximum operating pressure of the control valve. As such, the torque capacity has a potential for significant increase when a high-pressure control valve becomes available in the future.

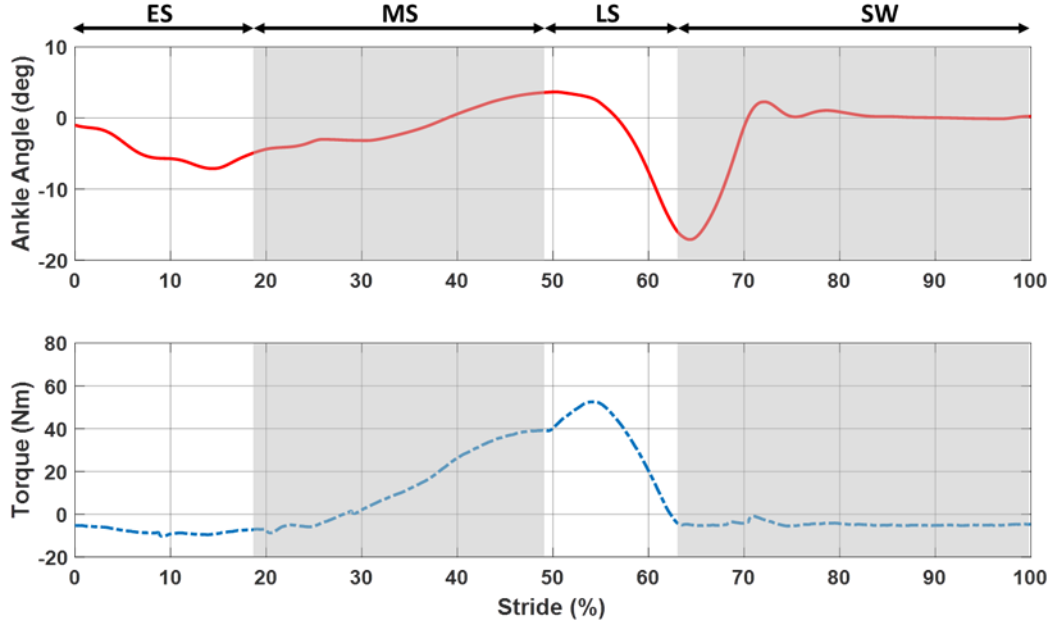


Figure 6-9: Typical position and torque trajectories of the prosthetic ankle joint in treadmill walking.

To provide more insight on the functioning of the directly implemented FSIC controller, the chamber pressure trajectories, and valve commands are shown in Figs. 6-10 and 6-11, respectively. In the Early Stance (ES), both chambers are closed so the actuator provides mild resistance to the ankle plantar-flexion before reaching foot-flat. In the Middle Stance (MS), both chambers are charged at the beginning. Due to the significant pressure increases, both valves are opened for an extended period of time in the MS, constituting the primary cause for the discrepancy between the modeling results shown in Section 3. In the Late Stance (LS), Chamber B stays closed to maintain its pressure (higher than the supply pressure), while Chamber A is

exhausted at the beginning to increase the joint torque for a powered push-off. In the Swing (SW), Chamber B is exhausted at the beginning to lower its pressure, such that an initial torque can be generated for the dorsiflexion of the joint. As can be clearly seen in Fig. 6-11, only very few valve actions are needed for the entire gait cycle, as the prosthesis controller makes the full use of the unique inherent dynamic characteristics of the pneumatic VSEA. Compared with the authors' prior work [20], in which a force control loop was implemented for the FSIC controller, the direct implementation of the FSIC controller requires significantly reduced control effort, while in the meantime provides a smoother interaction and more comfortable experience for the prosthesis user.

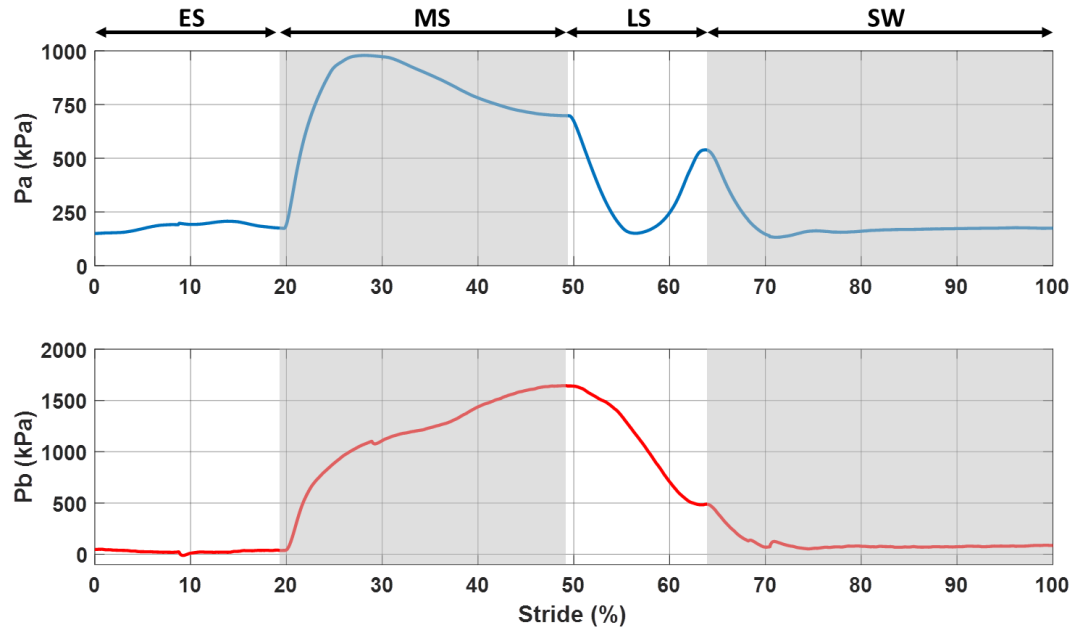


Figure 6-10: The chamber pressure trajectories of the prosthetic ankle joint (above: Chamber A pressure; below: Chamber B pressure).

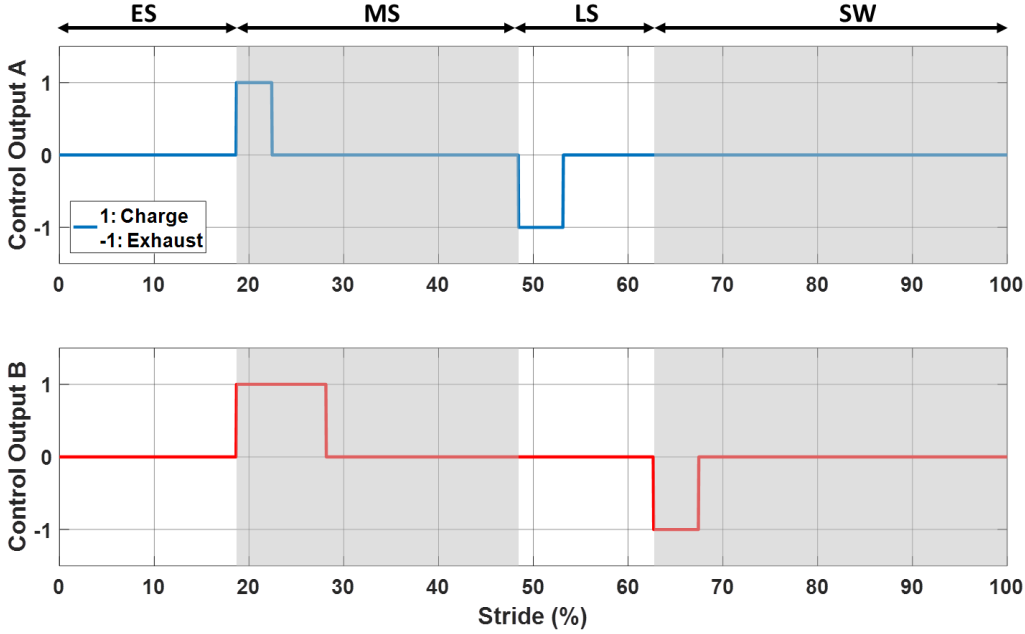


Figure 6-11: The valve commands of the prosthetic ankle joint (-1 represents exhausting the chamber, 0 represents closing the chamber, and 1 represents pressurizing the chamber).

6.5 CONCLUSIONS

In this chapter, the design, modeling, and control of a novel transtibial prosthesis was presented, which is powered by a unique pneumatic VSEA actuator. The pneumatic VSEA provides a physically existing elasticity, leveraging the compressibility of the working fluid in a pneumatic actuator, and thus eliminates the need for additional elastic elements. The modeling of the pneumatic VSEA was presented, and the design details of the pneumatic VSEA-powered prosthesis were also provided. With the pneumatic VSEA's ability of simultaneously controlling the actuator stiffness and equilibrium point, a novel control approach was developed, which enables the direct implementation of the FSIC controller. This direct FSIC approach eliminated the need for closed-loop force control, and thus significantly reduces the complexity and cost of the prosthesis control system. Furthermore, the controller action is minimized, contributing to a

smooth and comfortable experience for the prosthesis user. Experiments conducted on a human subject demonstrated the validity of modeling analysis as well as the effectiveness of the direct FSIC prosthesis control approach through a natural gait observed and recorded in the treadmill walking.

REFERENCES

- [1] Winter, D.A. (1983). Energy consumption and absorption at the ankle and knee during fast, natural, and slow cadences. *Clinical Orthopaedics and Related Research*, 175, pp. 147-154.
- [2] Winter, D. A. (1991). *Biomechanics and motor control of human gait: normal, elderly and pathological*. 2nd ed., Waterloo, ON, University of Waterloo Press.
- [3] Hsu, M. J., Nielsen, D. H., Lin-Chan, S. J., & Shurr, D. (2006). The effects of prosthetic foot design on physiologic measurements, self-selected walking velocity, and physical activity in people with transtibial amputation. *Archives of physical medicine and rehabilitation*, 87(1), 123-129.
- [4] Torburn, L., Powers, C. M., Guitierrez, R., & Perry, J. (1995). Energy expenditure during ambulation in dysvascular and traumatic below-knee amputees: a comparison of five prosthetic feet. *Journal of rehabilitation research and development*, 32(2), 111.
- [5] Au, S. K., Weber, J., & Herr, H. (2007, June). Biomechanical design of a powered ankle-foot prosthesis. In *Rehabilitation Robotics, 2007. ICORR 2007. IEEE 10th International Conference on* (pp. 298-303). IEEE.
- [6] Au, S. K., Weber, J., & Herr, H. (2009). Powered Ankle--Foot Prosthesis Improves Walking Metabolic Economy. *IEEE Transactions on Robotics*, 25(1), 51-66.
- [7] Herr, H. M., & Grabowski, A. M. (2012, February). Bionic ankle-foot prosthesis normalizes walking gait for persons with leg amputation. *Proceedings of the Royal Society B: Biological Sciences*, 279(1728), 457-464.
- [8] Try emPOWER. Retrieved January 23, 2017, from
<http://www.bionxmed.com/healthcare-professionals/the-empower-advantage/>.
- [9] Pratt, G. A., & Williamson, M. M. (1995, August). Series elastic actuators. In *Intelligent Robots and Systems 95.'Human Robot Interaction and Cooperative Robots', Proceedings. 1995 IEEE/RSJ International Conference on* (Vol. 1, pp. 399-406). IEEE.
- [10] Hitt, J. K., Bellman, R., Holgate, M., Sugar, T. G., & Hollander, K. W. (2007, January). The sparky (spring ankle with regenerative kinetics) project: Design and analysis of a robotic transtibial prosthesis with regenerative kinetics. *Proceedings of the ASME International Design Engineering Technical Conferences and Computers and Information in Engineering Conference*, Las Vegas, NV, pp. 1-10.

- [11] Hitt, J. K., Sugar, T. G., Holgate, M., & Bellman, R. (2010). An active foot-ankle prosthesis with biomechanical energy regeneration. *Journal of medical devices*, 4(1), 011003.
- [12] Lawson, B. E., Varol, H. A., Huff, A., Erdemir, E., & Goldfarb, M. (2013). Control of stair ascent and descent with a powered transfemoral prosthesis. *IEEE Transactions on Neural Systems and Rehabilitation Engineering*, 21(3), 466-473.
- [13] Shultz, A. H., Lawson, B. E., & Goldfarb, M. (2016). Variable cadence walking and ground adaptive standing with a powered ankle prosthesis. *IEEE Transactions on Neural Systems and Rehabilitation Engineering*, 24(4), 495-505.
- [14] Feldman, A. G., & Levin, M. F. (1995). The origin and use of positional frames of reference in motor control. *Behavioral and brain sciences*, 18(04), 723-744.
- [15] Hogan, N. (1980). Tuning muscle stiffness can simplify control of natural movement. In *Advances in Bioengineering, ASME Winter Annual Meeting* (pp. 279-282).
- [16] Hogan, N. (1984). Adaptive control of mechanical impedance by coactivation of antagonist muscles. *IEEE Transactions on Automatic Control*, 29(8), 681-690.
- [17] Hogan, N. (1985). The mechanics of multi-joint posture and movement control. *Biological Cybernetics*, 52(5), 315-331.
- [18] Sup, F., Bohara, A., & Goldfarb, M. (2008). Design and control of a powered transfemoral prosthesis. *The International journal of robotics research*, 27(2), 263-273.
- [19] Zheng, H., Wu, M., & Shen, X. (2016). Pneumatic Variable Series Elastic Actuator. *Journal of Dynamic Systems, Measurement, and Control*, 138(8), 081011.
- [20] Zheng, H., & Shen, X. (2015). Design and control of a pneumatically actuated transtibial prosthesis. *Journal of Bionic Engineering*, 12(2), 217-226.
- [21] Goldfarb, M., Barth, E. J., Gogola, M. A., & Wehrmeyer, J. A. (2003). Design and energetic characterization of a liquid-propellant-powered actuator for self-powered robots. *IEEE/ASME transactions on mechatronics*, 8(2), 254-262.

CHAPTER 7: CONCLUSION

Overall in this work, firstly, two types of sleeve muscle actuators were introduced, including a single-acting type with a fixed insert at the center, and a double-acting type with two chambers to provide bi-directional actuation capability. For each type of sleeve muscle, the basic structure was described in detail, and the force capacity was analyzed accordingly. Experimental results obtained on the prototypes validated and demonstrated that sleeve muscle is a good fit for robotic systems with asymmetric force/torque requirements.

Secondly, a unique robotic transtibial prosthesis that utilizes a pneumatic cylinder-type actuator to drive the prosthetic ankle joint is presented. For the walking control of the prosthesis, a finite-state impedance controller (FSIC) has been developed as a walking controller, and the parameters are tuned in walking experiments. The results from the experiments proved that the prosthesis is able to provide an improved gait compared with the traditional passive prosthesis.

Thirdly, a model that characterizes the stiffness and equilibrium point as functions of the chamber air masses in the pneumatic cylinder has been developed and a predictive pressure control algorithm was used to improve pressure control performance while minimizing valve actions. This enables the pneumatic actuator to be used as a variable series elastic actuator (VSEA). Experimental results showed that VSEA is able to provide the desired elastic characteristics of an artificial spring in stiffness control and demonstrated the advantages of this new approach for potential prosthetic applications.

Lastly, the dissertation presented VSEA-powered TT prosthesis with direct implementation of the finite-state impedance control (FSIC). Experiments conducted on a human subject demonstrated the validity of modeling analysis as well as the effectiveness of the direct FSIC prosthesis control approach through a natural gait observed and recorded in the treadmill walking.

REFERENCES

- [1] Ziegler-Graham, K., MacKenzie, E. J., Ephraim, P. L., Travison, T. G., & Brookmeyer, R. (2008). Estimating the prevalence of limb loss in the United States: 2005 to 2050. *Archives of physical medicine and rehabilitation*, 89(3), 422-429.
- [2] Owings, M. F., & Kozak, L. J. (1998). Ambulatory and inpatient procedures in the United States, 1996. *Vital and health statistics. Series 13, Data from the National Health Survey*, (139), 1-119.
- [3] Au, S. K., Weber, J., & Herr, H. (2009). Powered Ankle--Foot Prosthesis Improves Walking Metabolic Economy. *IEEE Transactions on Robotics*, 25(1), 51-66.
- [4] Waters, R. L., Perry, J., Antonelli, D., & Hislop, H. (1976). Energy cost of walking of amputees: the influence of level of amputation. *J Bone Joint Surg Am*, 58(1), 42-46.
- [5] Winter, D. A., & Sienko, S. E. (1988). Biomechanics of below-knee amputee gait. *Journal of Biomechanics*, 21(5), 361-367.
- [6] Bateni, H., & Olney, S. J. (2002). Kinematic and kinetic variations of below-knee amputee gait. *JPO: Journal of Prosthetics and Orthotics*, 14(1), 2-10.

APPENDIX: IRB APPROVAL



May 19, 2016

Xiangrong Shen, Ph.D.
Assistant Professor
Department of Mechanical Engineering
College of Engineering
The University of Alabama
Box 870276

Re: IRB Protocol # *12-009-ME-R465*
“Chemo-fluidic Sleeve Muscle-Actuated Robotic Below-Knee Prostheses – Prosthesis Testing”

Dr. Shen:

The University of Alabama Medical IRB recently met to consider your renewal application. The IRB voted to approve your protocol for a period of one year.

Your application will expire on May 12, 2017. You will receive a notice of the expiration date 90 days in advance. If your research will continue beyond this date, complete the renewal portions of the FORM: IRB Renewal Application. If you need to modify the study, please submit FORM: Modification of An Approved Protocol. Changes in this study cannot be initiated without IRB approval, except when necessary to eliminate apparent immediate hazards to participants. When the study closes, please complete the FORM: Request for Study Closure.

Please use reproductions of the IRB approved stamped consent form or information sheet to obtain consent from your participants.

Should you need to submit any further correspondence regarding this application, please include the above application number.

Good luck with your research.

Since

J. Grier Stewart, MD, FACP
Medical IRB Chair

**UNIVERSITY OF ALABAMA
INSTITUTIONAL REVIEW BOARD FOR THE PROTECTION OF HUMAN SUBJECTS
REQUEST FOR APPROVAL OF RESEARCH INVOLVING HUMAN SUBJECTS**

I. Identifying information

Names:	Xiangrong Shen	Second Investigator	Third Investigator
Department:	Mechanical Engineering	Hao Zheng	Young-Hui Chang
College:	Engineering	Mechanical Engineering	Applied Physiology
University:	The University of Alabama	Engineering	The University of Alabama
Address:	359 H.M. Comer Hall	359 H.M. Comer Hall	Georgia Institute of Technology
Telephone:	205-348-6743		555 14th Street NW, Atlanta, GA 30332
FAX:	205-348-6419		404-894-9993
E-mail:	xshen@eng.ua.edu	hzheng10@crimson.ua.edu	yh.chang@ap.gatech.edu

Title of Research Project: Chemo-fluidic Sleeve Muscle-Actuated Robotic Below-Knee Prostheses – Prosthesis Testing

Date Submitted: 04/15/2016

Funding Source: National Institutes of Health

Type of Proposal	<input type="checkbox"/> New	<input checked="" type="checkbox"/> Revision	<input checked="" type="checkbox"/> Renewal Please attach a renewal application	<input type="checkbox"/> Completed	<input type="checkbox"/> Exempt
Please attach a continuing review of studies form					
Please enter the original IRB # at the top of the page					

UA faculty or staff member signature: 

II. NOTIFICATION OF IRB ACTION (to be completed by IRB).

Type of Review: Full board Expedited

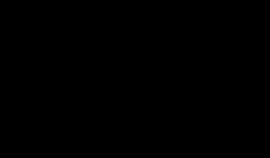
IRB Action:

<input type="checkbox"/> Rejected	Date: _____
<input type="checkbox"/> Tabled Pending Revisions	Date: _____
<input type="checkbox"/> Approved Pending Revisions	Date: _____

Approved–this proposal complies with University and federal regulations for the protection of human subjects.

Approval is effective until the following date: *5/12/17*

Items approved:	<input type="checkbox"/> Research protocol (dated _____)
<input type="checkbox"/> Informed consent (dated _____)	
<input type="checkbox"/> Risk/Benefit (dated _____)	
<input type="checkbox"/> Other (dated _____)	

Approval signature  Date *5/19/16*

The University of Alabama Individual's Consent to be in a Research Study

Title of Research: Chemo-fluidic Sleeve Muscle-Actuated Robotic Below-Knee Prostheses

Investigator(s): Xiangrong Shen, Young-Hui Chang, Hao Zheng

IRB Approval #: 12-009-ME-R4

OSP #: 12-0083

Sponsor: NIH

Your are being asked to be in a research study.

The name of this study is "Chemo-fluidic Sleeve Muscle-Actuated Robotic Below-Knee Prostheses – Prosthesis Testing."

This study is being done by Dr. Xiangrong Shen, Assistant professor in Mechanical Engineering at the University of Alabama. Hao Zheng, a doctoral student in Mechanical Engineering at the University of Alabama, and Dr. Young-Hui Chang, associate professor in the School of Applied Physiology at Georgia Institute of Technology, will assist Dr. Shen in this research.

What is the purpose of this study?

The purpose of this study is to test a chemo-fluidic sleeve muscle actuated active below-knee prosthesis. This new powered prosthesis utilizes high-concentration (70%) hydrogen peroxide to generate the high-pressure gas to drive a novel sleeve muscle actuator. With the new technology, the prosthesis is expected to function like a human leg, weigh less, and last long. In this study, we want to test the prosthesis and see if it can help the wearer to walk more naturally than traditional unpowered prostheses.

Why is this study important?

This study, if successful, will help the below-knee amputees to move more freely and enjoy a better life.

Why have I been asked to be in this study?

You have been asked because you meet the requirements of this study, including one-side below-knee amputee, between 19 and 55 years old, physically fit, at least two years after amputation, and having previous experience of wearing prosthesis.

How many other people will be in this study?

4 persons will be in this study, including one at the University of Alabama, and three at Georgia Institute of Technology.

What will I be asked to do in this study?

You will be asked to wear the new prosthesis or your daily-use prosthesis and conduct a few tests, such as the walking experiments on the treadmill, when the treadmill is level or tilted. We

will compare your walking with the new robotic prosthesis versus that with your daily-use prosthesis, and see if the new robotic prosthesis works better or not.

How much time will I spend being in this study?

You will spend 14 days being in this study. For each day of testing, you will spend about 4 hours. This includes the actual experiment time and the setup time. The whole testing does not necessarily need to be completed in 14 days in a row, and we will arrange the testing time to better fit your schedule. Also, if anything goes wrong, we might need some time to fix the problem. So, possibly there will be periods of time separating the testing days.

How much will the study cost?

It will cost you nothing.

Will I be compensated for being in this study?

In appreciation of your time, and to cover the travel expenses to the experimental site, you will receive 100 dollars per day during the test. If you withdraw from this study before it is completed, your compensation will be prorated based on how much you have completed at the moment of withdrawal.

What are the benefits of being in this study?

Although you will not benefit personally from being in this study, you may feel good about knowing that you have helped in creating this robotic prosthesis. If the prosthesis works well, people with below-knee amputation will be able to use it and walk more freely.

What are the risks (dangers or harms) to me if I am in this study?

The major risk to you is falling down if the controller does not work well. Under the protection of the overhead harness, you are not likely to be injured. Also, your skin may feel uncomfortable if you touch the hot surface or the exhaust. But we will wrap the hot surface with thick insulation material and make sure that the exhaust is taken care of properly, so the chance of your skin getting hurt is really low.

How will my privacy be protected?

We will not contact you if you don't want us to. If you leave us your contact information, we will keep it safe so no one else will be able to get it, unless you tell us to. Also, we will contact you only in a way comfortable to you. In the testing, the door of the laboratory will be closed, and only the investigators will be present during testing.

How will my confidentiality be protected?

Your participation in this study is totally confidential. Your name will not appear on any study document besides this consent form. There is no way to link the consent form and name with data. We will store the data from the study in computers only we can access, or in locked cabinets in locked offices. No one will have access to it except the investigators. We will publish scientific articles on this study but no family, town, or Alabama county will be identified.

Do I have to be in this study?

No. If you decide to be in this study it should be because you really want to volunteer. You can refuse to be in the study. You can also start the study and decide to stop at any time. If you refuse or if you start the study and then stop it, you will not lose any benefits or rights you would normally have.

If I don't want to be in the study, are there other choices?

If you do not want to be in this study, the other choice is to refuse. We will thank you for your time and you will be allowed to leave.

What if new information is learned during the study that might affect my well-being or decision to continue in the study?

If new information is learned that affects this study, we will tell you about it. You can tell us at any time whether you want to continue the study or not.

What if I have questions, suggestions, concerns, or complaints?

If you have questions about the study during the testing, please feel free to ask. If you have any questions or concerns later, you can reach Dr. Shen at 205-348-6743. If you have questions about your rights as a person taking part in a research study, make suggestions or file complaints and concerns, you may call Ms. Tanta Myles, the Research Compliance Officer of the University at (205)-348-8461 or toll-free at 1-877-820-3066. You may also ask questions, make suggestions, or file complaints and concerns through the IRB Outreach Website at http://osp.ua.edu/site/PRCO_Welcome.html. You may email us at participantoutreach@bama.ua.edu.

What else do we need to know?

You do not give up any of your legal rights by signing this consent form.

You will be given a copy of this consent form to keep. Save it in case you want to review it later or you decide to contact the investigator or the university about the study.

The University of Alabama Institutional Review Board (IRB) is the committee that protects the rights of people in research studies. The IRB may review study records from time to time to be sure that people in research studies are being treated fairly and the study is being carried out as planned.

I have read this consent form. I have had a chance to ask questions.

Signature of Research Participant _____ Date _____

Signature of Investigator _____ Date _____